ASTROPHYSICAL ICES IN THE LABORATORY AND THE NATURE OF SOLID CARBON DIOXIDE IN MOLECULAR CLOUDS

By

Perry Alexander Gerakines

A Thesis Submitted to the Graduate

Faculty of Rensselaer Polytechnic Institute

in Partial Fulfillment of the

Requirements for the Degree of

DOCTOR OF PHILOSOPHY

Major Subject: Physics

Approved by the
Examining Committee:

Douglas C. B. Whittet, Thesis Adviser

James P. Ferris, Member

Joseph W. Haus, Member

James Napolitano, Member

Wayne G. Roberge, Member

Rensselaer Polytechnic Institute
Troy, New York

October 19, 1998
(For Graduation December 1998)

CONTENTS

LIST OF TABLES

LIST OF FIGURES

Acknowledgements

After five and a half years as a graduate student and life on two continents, it is quite a task to remember the names of all the friends and colleagues deserving of mention here. I will try, but I apologize to anyone inadvertently omitted.

I have three personal dedications for this book. First of all, this is for my parents. My mother, Barbara Gerakines, has been waiting for many years to call me "Doctor." She always encouraged me to think for myself and to take advantage of opportunities when they came my way. She trusted me to make my own decisions, and helped me out when my choices turned out to be less than perfect. Thanks, Mom. For my father, Stephen Gerakines, thank you for looking me in the eye and telling me to go to whatever school I wanted, that you would be able to handle it. Most of all, thanks for cheering so much at my graduation in 1993. It meant a lot to me. This thesis is also for my wife, Suzanne, who had to put up with me while I was writing it and kept me from being too nit-picky with myself (not so easy to do, eh?). You gave me a reason to smile on those extremely short, dark and rainy Dutch winter days as I bicycled upwind (both ways) to and from work. I don't know where I'd be today without you. Finally, I dedicate my PhD. work to my daughter, Stephanie, in the hopes that she will grow to be the explorer that I can see in her at only 11 months of age.

I attribute the contents of this thesis and all that I've learned of astronomy to my advisor and friend, Doug Whittet. The day I approached him in the fall of 1991 to do undergraduate research opened the door for so many experiences that followed. I don't believe I would be the same person without those oppportunities and all those pats on the back. Thanks, Doug.

Many thanks to the denizens of the Starlab, past and present: especially to Sean Carey, Don Mizuno, Mike Fogel, Erika Gibb, Lida He, Dave Joiner, Andy Kalukin, Monika Kress, Dave Messinger, Heather Rave, and Nicolle Zellner. Thanks to Becky DiBari for helping me study for the quals. Thanks to Kristen Larson for teaching me the difference bewteen "that" and "which" and for not always beating

me to the dictionary when someone in the lab had an odd grammar question. Thanks to Doug Caldwell for his penchant for *starting* many a ludicrous debate (and, come to think of it, for not knowing when to *stop one*, either). Thanks to Jean Chiar for being such a good collaborator, friend, and giver of advice (but mostly for telling me to shut up when I really needed to).

Thanks to everyone at Leiden Observatory who took me in and made me feel at home: especially Ewine van Dishoeck, Pascale Ehrenfreund, Mayo Greenberg, Menno de Groot, Frank Helmich, Michiel Hogerheijde, David Jansen, Tom Millar, François Rouleau, Willem Schutte, Osmama Shalabiea, Marco Spaans, Zhangfan Xing, and Tim de Zeeuw. Special thanks to Willem, Pascale, and Menno for teaching me what they knew about Lab Astrophysics. Thanks to Xander Tielens for his advice and to Adwin Boogert for teaching me all about ISO-SWS data reduction.

Thanks to Leo Arrebola-Aranda for putting up with me as a flat-mate for nearly two years ("of course, my horse!"). Special thanks to Ray DeCampo and Erik Saperstein for being great friends during what turned out to be very tumultuous times in all of our lives (yes, Erik, they were!).

Thanks to my Thesis committee members, Jim Ferris, Joe Haus, Jim Napolitano, and Wayne Roberge, for their questions, suggestions, and advice. Thanks also to Marc Kutner, Chun Leung, and Wayne Roberge for getting me into astronomy in the first place by teaching it so well. Thanks also to Judy, Kate, and Tracie in the Physis office for answering my innumerable administrative questions.

Last but not least, I thank NASA for supporting my research through grants NAGW-3144, NAGW-4039, NAG5-3339, and NAG5-7410.

Abstract

Icy grain mantles in the interstellar medium play an important role in the chemistry of molecular clouds. The vibrational absorption features of solid-state materials are detected by infrared (IR) spectroscopy, and the study of laboratory ice analogs provides a means by which they may be interpreted. The general methodology behind laboratory astrophysics is discussed. The absorption strengths of a molecule's IR features are important parameters used to calculate its interstellar abundance, and results presented show that these strengths are only weakly dependent on the ice environment. Results of ultraviolet (UV) irradiation experiments on nine pure ices are presented and show a remarkable complexity in certain cases. Pure methane (CH_4), formaldehyde (H_2CO) and methanol (CH_3OH) ices are shown to be efficient producers of complex organics. These experiments provide a basis by which more complex UV photochemistries may be evaluated.

Spectra of interstellar carbon dioxide (CO_2) taken by the Short-Wavelength Spectrometer (SWS) on the Infrared Space Observatory (ISO) at a resolving power $\lambda/\Delta\lambda \approx 1500$ are presented for 14 lines of sight. The selected sources include a background field star (Elias 16), massive protostars (Elias 29, GL 490, GL 2136, GL 2591, GL 4176, NGC 7538 IRS9, NGC 7538 IRS1, S 140, W3 IRS5, and W33 A), and sources associated with the Galactic Center (Sgr A*, GCS 3I, and GCS 4). These sight-lines probe a diverse range of environments, but measured column densities of CO_2 fall in the range 10–23 % relative to water (H_2O): this ratio displays remarkably little variation for such a physically diverse sample. Comparisons with laboratory data indicate that interstellar CO_2 generally exists in two phases, one polar (H_2O-dominant) and nonpolar (CO_2-dominant). The observed profiles may also be reproduced when the nonpolar components are replaced with thermally annealed ices. Formation and evolutionary scenarios for grain mantle chemistry are discussed. Results show that thermal annealing, rather than energetic processing due to UV or cosmic rays, dominates the evolution of the CO_2-bearing ices.

CHAPTER 1
INTRODUCTION

"Plato is my friend, Aristotle is my friend, but my greatest friend is Truth."

Sir Isaac Newton[1]

1.1 The Interstellar Medium

The space between the stars contains clouds of gas in approximate pressure equilibrium. Observations of these clouds at radio and millimeter wavelengths reveal a highly varying, rich mixture of gas species dominated by either atomic or molecular hydrogen (see e.g., Evans, Lacy, & Carr 1991). The average particle density of the interstellar medium (hereafter "ISM") is only about one atom per cubic centimeter (compared to $10^{19}\,\mathrm{cm}^{-3}$ in Earth's atmosphere), but the majority of its mass is grouped into clumps of so-called *diffuse* and *dense molecular* (or *dark*) *clouds*, the birthplaces of new stars. Gas densities in molecular clouds are many orders of magnitude above the average, ranging from 10^3 to greater than $10^6\,\mathrm{cm}^{-3}$. The most abundant gas-phase molecules in molecular clouds are H_2 and CO, permeated with a population of *dust particles* which are relatively low in abundance (about 10^{-12} per gas particle) but have large extinction cross sections at visual wavelengths (about $10^{-12}\mathrm{cm}^2$; e.g., Draine & Lee 1984). Indeed, the attenuation of light by interstellar dust grains is the reason why molecular clouds appear dark against a field of background stars. Modeling of the extinction and polarization of starlight which passes through these dust clouds reveals that there are at least two major varieties of interstellar grains: particles of about $0.1\,\mu$m in size which are responsible for absorption at visual and infrared wavelengths, and very small grains $\lesssim 0.01\,\mu$m in diameter (or perhaps large molecules such as polycyclic aromatic hydrocarbons, "PAHs") which cause a steep rise in extinction in the far ultraviolet (Mathis, Rumpl, & Nordsieck 1977; Greenberg 1979; Duley & Williams 1981; Chlewicki 1985).

[1]Translated from the original Latin: *"Amicus Plato amicus Aristoteles magis amica veritas."*

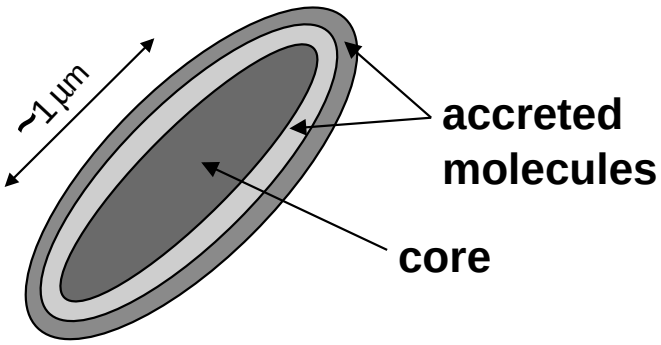

Figure 1.1: Simple schematic of a mantled interstellar dust grain.

1.2 Icy Grain Mantles

Emission curves of the dust inside dense clouds resemble blackbodies whose peaks fall in the far infrared ($\lambda = 40$–$400\,\mu$m), indicating that they are cold: T $\approx$ 5–50 K. In the coldest regions, the sticking probabilities of most molecules heavier than H_2 are approximately equal to unity (e.g., Leitch-Devlin & Williams 1985; Sandford & Allamandola 1990). There are also no efficient means of removing molecules from cold dust grains. Thus, gas species should accumulate on grain surfaces efficiently and in short timescales (with respect to the typical lifetime of a cloud of 10^7 yr). Accreted species may then remain frozen to the dust, perhaps to undergo chemical reactions with other molecules residing there, forming an *icy grain mantle*[2] with a potentially complex chemistry. Figure 1.1 displays a simple schematic of a mantled interstellar dust grain.

The existence of interstellar ices was first proposed by Lindblad (1935), who suggested that ices would form in the ISM by random accretion, and his work was expanded into a more complex model for ice nucleation and growth by Oort & van de Hulst (1946). Unfortunately, the technology required for interstellar ice observations did not emerge until the 1960's. Ices are detected in the ISM via the absorption features of molecular vibrational modes (called *stretching*, *bending*, or *deformation* modes, depending on the nature of the interatomic motion involved), whose fundamental frequencies fall in the mid infrared ($\lambda = 2$–$25\,\mu$m). Only tran-

[2]With apologies to non-astronomers, the phrases *icy mantles* and *interstellar ices* henceforth refer not only to solid H_2O, but to any mixture of volatile molecules frozen onto interstellar dust grains. In support of this nomenclature, *Webster's New Universal Unabridged Dictionary* provides the following definition: "**ice**, *n.* 3. anything like frozen water in appearance, structure, etc."

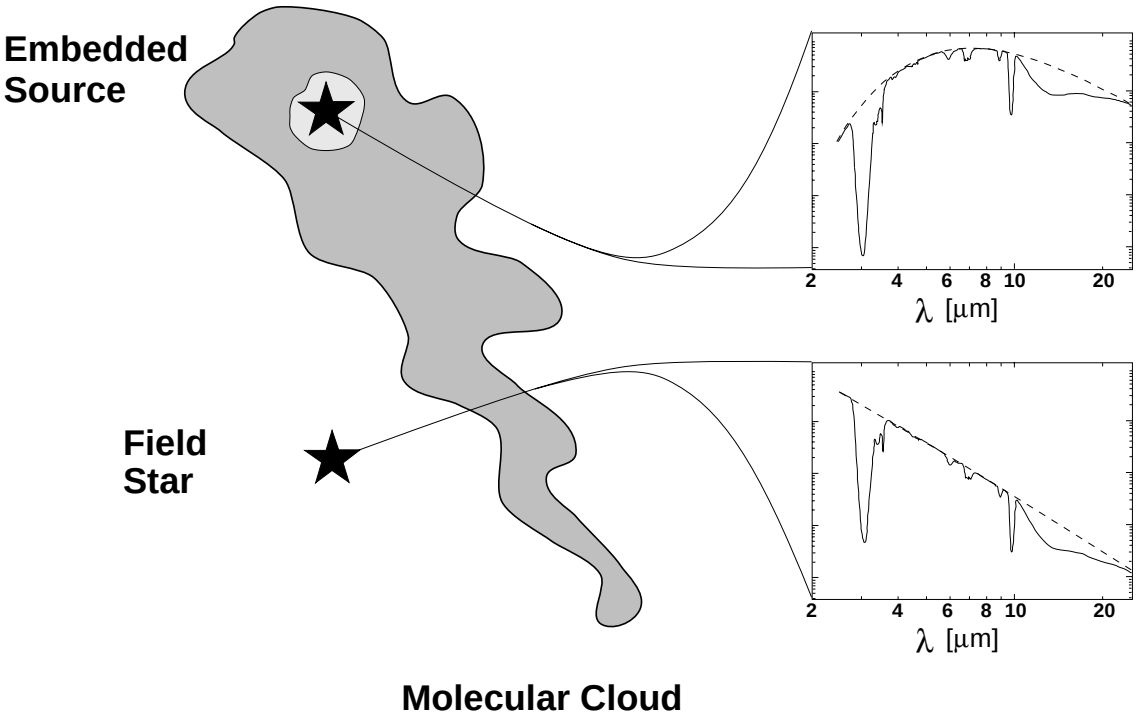

Figure 1.2: Comparison of typical observations of interstellar ices toward embedded sources (top) and background field stars (bottom). The flux spectra (solid lines) are shown on logarithmic scales and span the wavelength range from 2 to 25 μm. The ice spectrum is the same in each figure (H_2O:CH_3OH:CO:NH_3 = 100:50:1:1, T = 10 K; Hudgins et al. 1993), only the continua differ (dotted lines).

sitions that cause a change in dipole moment are observable. Thus, homo-nuclear diatomic molecules such as O_2 and N_2 cannot be studied with infrared spectroscopy (in pure form only: their infrared transitions may become weakly active when they reside in a strongly-interacting ice matrix; see, e.g., Ehrenfreund et al. 1992).

Ice absorption features are seen in the spectra of objects whose lines of sight intersect dense interstellar clouds. Either the radiation source is actually embedded inside the cloud and the hot dust surrounding it provides the background radiation for the absorptions (a *protostar*, or *young stellar object* "YSO"), or it is located at some unknown distance behind the cloud and absorption features are superimposed on the star's blackbody emission curve (a *field star*). These cases are contrasted in Fig. 1.2. The former case usually provides a higher flux level in the mid infrared, where the blackbody emission of materials at T $\sim$ 100–900 K is the strongest. Radia-

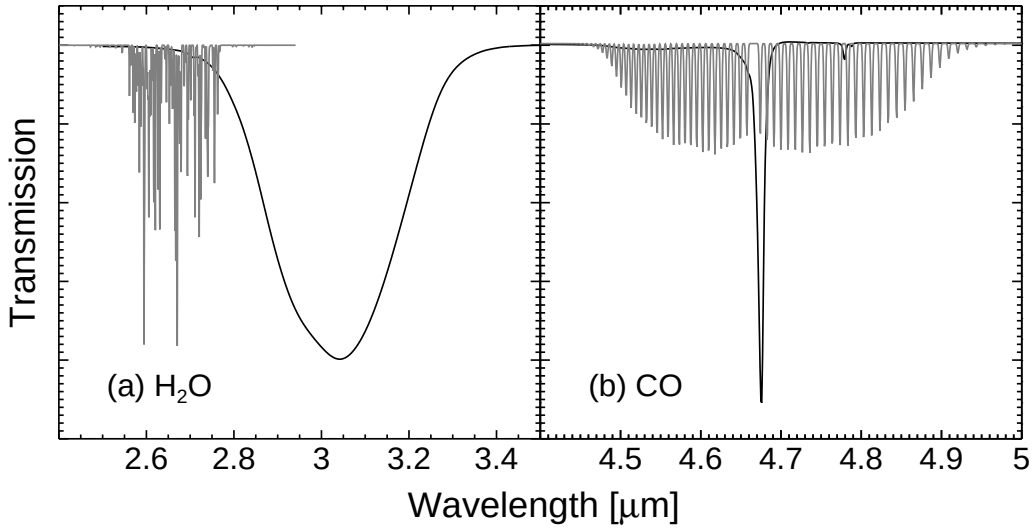

Figure 1.3: Comparison of gas- and solid-phase spectra of (a) H_2O and (b) CO. Ice spectra (black lines) come from laboratory-measured samples of amorphous materials at 10 K (This work, Ch. 4; Ehrenfreund et al. 1997). Gas-phase spectra (grey lines) are computed models of molecular ro-vibrational modes at 250 K from Helmich (1996), Chapter 7.

tion from a typical background field star peaks at visible to near-infrared wavelengths and decreases rapidly in the mid infrared.

Although a certain vibrational transition falls at (approximately) the same frequency in both gas and solid phases, these two components may be spectroscopically separated given adequate resolution. This is primarily due to the fact that gas-phase species are free to rotate, unlike their solid-phase counterparts that are locked into an ice matrix. Therefore gas-phase spectra contain sharp structures due to the coupling of rotation and vibration (hence these are known as "ro-vibrational" modes; $\Delta\nu \sim 1$–$2\,\mathrm{cm}^{-1}$), while those of the solid are relatively broad and free of such substructure ($\Delta\nu \sim 5$–$400\,\mathrm{cm}^{-1}$; Fig. 1.3). Moreover, the peak absorption of the solid is typically redshifted from the center of the gas-phase Q-branch due to energetic effects of the surrounding ice matrix. This shift, demonstrated in Fig. 1.3, is most prominent for molecules with a strong dipole moment and/or form hydrogen bonds in the solid state (such as H_2O). It is less prominent for species that have little or no solid-state interaction (such as CO).

The first interstellar ice feature to be detected was the O–H stretching fun-

damental (ν_3) of H_2O located at 3.05 μm (Gillett & Forrest 1973). Since then, the infrared features of several other molecules have been detected; see the listing in Table 1.1. Nevertheless, H_2O remains the most abundant of all molecules thought to be present in icy mantles ($N_{H_2O}/N_H \sim 10^{-5}$–$10^{-4}$). In fact, the column densities of all other icy mantle constituents are commonly expressed as a percentage relative to the H_2O abundance along the same line of sight (Table 1.1).

1.3 Interstellar Chemistry

The primary role of dust in the ISM (from a gas-phase point of view) is to provide a surface upon which H atoms may react to form H_2 (e.g., Hollenbach & Salpeter 1971), but a variety of other species may also be produced in gas-grain interactions, including both gas-phase and icy mantle constituents. Models by d'Hendecourt, Allamandola, & Greenberg (1985), for example, show that the composition of the mantle depends on the cloud's gas-phase environment: where the fraction of H/H_2 is significant ($\sim$ 0.01–0.1 %), molecules such as H_2O, NH_3, and CH_4 are produced by the hydrogenation of atomic O, N, and C (respectively) on grain surfaces. In cloud environments where $H \rightarrow H_2$ conversion is nearly complete, molecules such as CO, O_2, and N_2 become abundant in the gas phase; these accrete directly onto the grain surface at low temperatures.

Observed profiles of the 4.67 μm CO absorption feature support the existence of at least two distinct ice phases (Tielens et al. 1991; Chiar et al. 1994; Chiar et al. 1998b): *polar* (H_2O-rich), and *nonpolar* (H_2O-poor). The nonpolar ices are dominated by molecules such as CO, CO_2, O_2, or N_2. It is uncertain whether these phases represent physically segregated mantle layers on the same grains or separate grain populations in different cloud regions along the observed lines of sight. The presence of methanol (CH_3OH) and the possibility of formaldehyde (H_2CO) in the icy mantles (Allamandola et al. 1992; Schutte et al. 1996a) suggest an intermediate state in which the CO molecule may be hydrogenated by H addition: i.e., $CO \stackrel{H}{\rightarrow} HCO \stackrel{H}{\rightarrow} H_2CO \stackrel{H}{\rightarrow} CH_3OH$ (see discussion in Tielens & Whittet 1997 and references therein).

The driving forces behind interstellar ice chemistry are surface reactions, heat-

Table 1.1: Molecules detected in icy grain mantles

Molecule	Vibration Mode	Wavelength [μm]	Abundance [% H_2O]	Refs
H_2O	(ν_3) O–H stretch	3.05	···	1,2,3,4
	(ν_2) H–O–H bend	6.02		
	(ν_1) libration	13.16[a]		
CO	$^{12}C\equiv O$ stretch	4.67	5–50	5,6,7
	$^{13}C\equiv O$ stretch	4.78		
CO_2	($\nu_1 + \nu_3$) combination	2.70	10–23	8,9
	($2\nu_2 + \nu_3$) combination	2.78		
	(ν_3) $^{12}C{=}O$ stretch	4.27		
	(ν_3) $^{13}C{=}O$ stretch	4.38		
	(ν_2) O=C=O bend	15.15		
CH_3OH	C–H stretch	3.53	1–10	10,11
	C–O stretch	9.75		
H_2CO	(ν_5) C–H stretch	3.48[a]	1–10	12
HCOOH	C=O stretch	5.83[a]	2–4	13
CH_4	(ν_4) deformation	7.70	0.5–2	14,15
H_2	H–H stretch	2.42	~ 1	16
"XCN"[b]	C–N stretch	4.62	~ 1	5,17
OCS ("XCS"[b])	C–S stretch	4.91	~ 0.1	18,19
$-CH_2-$, $-CH_3$[c]	C–H stretch	3.47	···	20,21

[a] tentative detection.

[b] "X" denotes an unknown atom or group. Abundances for these species cannot be accurately calculated.

[c] Groups of simple hydrocarbons which cannot be deconvolved.

References.— (1) Willner et al. 1982; (2) Whittet et al. 1988; (3) Smith, Sellgren, & Tokunaga 1989; (4) Whittet et al. 1996; (5) Lacy et al. 1984; (6) Larson et al. 1985; (7) Geballe 1986; (8) this work, Ch. 6; (9) this work, Ch. 7; (10) Allamandola et al. 1992; (11) Skinner et al. 1992; (12) Schutte et al. 1996a; (13) Schutte et al. 1996b; (14) Lacy et al. 1991; (15) Boogert et al. 1996; (16) Sandford & Allamandola 1993; (17) Tegler et al. 1995; (18) Geballe et al. 1985; (19) Palumbo, Geballe, & Tielens 1997; (20) Pendleton et al. 1994; (21) Chiar, Adamson, & Whittet 1996.

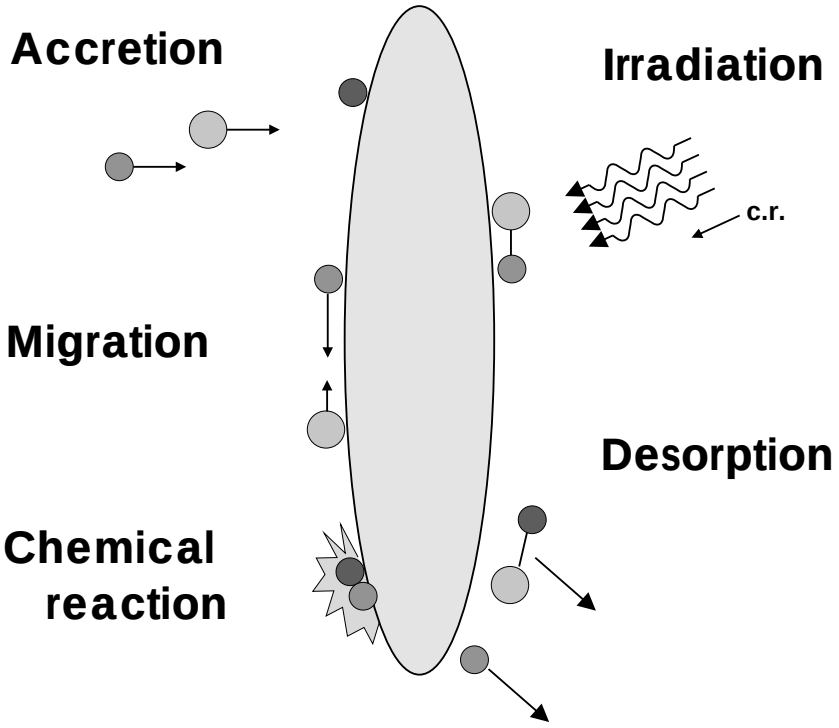

Figure 1.4: The elements of grain surface chemistry.

ing due to nearby protostars, shocks, or irradiation due to the interstellar radiation field (ISRF) and/or cosmic rays. The different elements of grain surface chemistry are displayed in Fig. 1.4. When atoms encounter a grain surface they attach themselves to *chemisorption* sites (chemically bound) or *physisorption* sites (physically bound by, e.g., electromagnetic forces) between which they may migrate, eventually sampling the entire surface. The time it takes an atom to sample the grain surface depends on its mass, the strength with which it bonds to a site, and the grain's temperature. Estimated sampling rates for species on an H_2O surface at $T = 10\,K$ are– $10^{-12}\,s$ for H, $4\times 10^{-12}\,s$ for H_2, and $10^{-2}\,s$ for C, N, and O (Tielens & Allamandola 1987). Since these times are much shorter than a typical evaporation time (10^3 to more than $10^7\,s$ for these species, and essentially infinite times for all others; see Tielens & Allamandola 1987), an H, C, N or O atom (or even an H_2 molecule) is able to sample the entire grain surface a large number of times before evaporating: thus increasing the probability of interaction with the other species frozen to the surface prior to its arrival.

At $T \lesssim 20\,K$ (as inside dense clouds), however, only chemical reactions which

are exothermic will proceed directly, and those containing energetic barriers, if they are to take place, will require quantum tunneling. Given the relatively large amount of time a species has to sample the entire grain surface, and the long time scales between arrival times of other reactants ($\sim$ 1 day; Tielens & Hagen 1982), even reactions with moderately low tunneling probabilities may proceed. Estimates by Tielens & Whittet (1997) predict that hydrogenation reactions with barriers as high as 2000 K could take place under these conditions. For heavier atoms such as O, the limiting reaction barrier is lower, $\simeq$ 400 K.

Icy mantles are subjected to UV radiation and ion bombardment capable of driving energetic reactions which process them into more complex species. The dominant sources of UV radiation are (i) embedded protostars, (ii) secondary electrons produced in the cosmic-ray–ionization of H_2, and (iii) the ISRF (e.g., Greenberg 1973; Sternberg, Dalgarno, & Lepp 1987; Prasad & Tarafdar 1983; Schutte & Greenberg 1991 and references therein). The cosmic-ray–induced UV flux internal to a dense cloud amounts to $\sim 10^3\,\mathrm{cm^{-2}\ s^{-1}}$ ($\mathrm{E}_{h\nu} > 6.2\,\mathrm{eV}$) for a typical cosmic ray ionization rate of $\xi \approx 10^{-17}\,\mathrm{s^{-1}}$ (Sternberg, Dalgarno, & Lepp 1987; Gredel et al. 1989). The intensity of the penetrating ISRF depends on the position in the cloud as well as the cloud morphology. In the outer cloud regions, this will be the dominating source of UV photons, with a UV intensity of up to $\sim 8\times 10^7\,\mathrm{cm^{-2}\ s^{-1}}$ ($\mathrm{E}_{h\nu} > 6$ eV; Mathis, Metzger, & Panagia 1983).

The interstellar ice feature at 4.615 μm in the spectra of several embedded protostellar sources provides observational evidence for UV photolysis of ice mantles in dense clouds (Lacy et al. 1984; Tegler et al. 1995). This feature is well reproduced by the irradiation of laboratory ices which contain NH_3 and CO in an H_2O-dominated mixture and has been assigned to the OCN^- ion in these experiments (Grim & Greenberg 1987). However, the species responsible for the interstellar feature is still uncertain (isonitriles such as CH_3NC also produce a good fit; Grim & Greenberg 1987). Recent observations of embedded protostars and background field stars (Tegler et al. 1995) seem to indicate that this feature is confined to regions of early star formation. Taken together, these two facts point to an important role of such regions in the chemical processing of interstellar ices.

1.4 Goals and Outline of this Thesis

The goal of this research is to study the physical and chemical properties of the ices which comprise the icy grain mantles of dense interstellar clouds. Studies of laboratory analogs of these ices give us a greater understanding of their physical and chemical properties. When these laboratory data are matched to the interstellar data, we may then constrain the nature of interstellar environments.

Chapter 2 introduces the principles of laboratory astrophysics and summarizes the experimental procedures used to produce the results given in Chapters 3 and 4. In Chapter 3, the changes in strengths of the infrared features of H_2O, CO and CO_2 as a function of ice mixture are investigated. Chapter 4 presents a study of the photochemical properties of ice mantle component molecules, representing the first step in the understanding of chemistries involved in more complex mixtures. Chapter 5 describes the Infrared Space Observatory (ISO), the Short Wavelength Spectrometer (SWS), and the data reduction techniques used in deriving the observed interstellar CO_2 spectra presented in Chapters 6 and 7. The origins of solid CO_2 in molecular clouds and the key factors its evolution are studied in a large range of environments. Finally, a summary of this work is given in Chapter 8.

CHAPTER 2
METHODS OF LABORATORY ASTROPHYSICS

"What one fool can do, another can do better!"

Richard P. Feynman

2.1 Laboratory Astrophysics

The profiles of observed interstellar ice features vary widely from source to source (e.g., Whittet, Longmore, & McFadzean 1985; Whittet et al. 1988; Chiar et al. 1994, 1995). Their properties can reveal a great deal about ice environments in dense molecular clouds, since the exact positions and widths of absorption features are strongly dependent upon many environmental factors, including *total* ice composition, temperature and thermal history, levels of annealing, crystalline structure, and doses of irradiation. In order to extract meaningful information about these physical parameters, it is necessary to compare observations to a wide range of laboratory-produced analogs which represent an appropriate variety of ice environments.

To this end, many projects have been undertaken at several facilities around the world. The first laboratory astrophysics group to study interstellar ices was created at Leiden University in the Netherlands by J. Mayo Greenberg. Aspects of ice chemistry studied there have included UV photochemistry of mixtures such as H_2O:CO:NH_3 (e.g., Hagen, Allamandola, & Greenberg 1979; d'Hendecourt et al. 1986; Grim 1988), the production of complex organic species from initially simple ice mixtures (e.g., Grim 1988; Schutte 1988), ice desorption mechanisms (d'Hendecourt, Allamandola, & Greenberg 1985), and grain surface chemistry (e.g., Grim & d'Hendecourt 1986; Zhao 1990).

Research at the NASA/Ames laboratory in Mountainview, CA includes studies of CO- and CO_2-bearing ices (Sandford et al. 1988; Sandford & Allamandola 1990), the properties of PAH's (e.g., Salama & Allamandola 1992; Salama et al. 1996), and

UV photochemistry and thermal processing (e.g., Allamandola, Sandford, & Valero 1988; Bernstein et al. 1995; Bernstein, Sandford, & Allamandola 1997). The effects of ion bombardment on mantle ice analogs have been studied in laboratories in Catania, Italy (e.g., Strazzulla & Baratta 1992), and NASA/Goddard in Greenbelt, MD (e.g., Moore et al. 1983; Moore, Khanna, & Donn 1991).

The photochemical and thermal evolution of ice mantles is simulated by condensing mixtures of gases onto a cold substrate ($T \sim 10\,K$) situated in a vacuum chamber ($P \sim 10^{-8}\,mbar$), which may then be exposed to UV photons or heated within the setup. These condensed and treated samples may then be analyzed *in situ* using a fast-Fourier infrared (FTIR) spectrometer, in which the sample chamber is located (e.g., Allamandola, Sandford, & Valero 1988; Hudgins et al. 1993).

Interstellar IR features may often be reproduced in the laboratory. Since their profiles are strongly dependent on the ice environment in which the parent molecules reside, many properties of interstellar ices may be inferred through just one absorption feature (e.g., Sandford et al. 1988; Elsila, Allamandola, & Sandford 1997). A prime example is the C≡O stretching feature of solid CO at $4.67\,\mu m$ ($2138\,cm^{-1}$) which exhibits properties of CO mixed in H_2O as well as those of CO mixed with nonpolar molecules (e.g. Tielens et al. 1991; Chiar et al. 1994). Another example is the $3.05\,\mu m$ feature of solid H_2O, whose profile is often used to trace the thermal history and composition of the ices (e.g., Hagen, Greenberg, & Tielens 1983; van de Bult, Greenberg, & Whittet 1985).

Since the molecules of interstellar icy grain mantles may exist in many different environments, it is important to understand how the strengths of their IR absorbance features change with respect to environment. Ice abundances are derived from the areas of ice absorption features and on their assumed *absorption strengths* (or *integrated absorption cross sections*). Previous studies in the literature have been made in which these absorption strengths have been derived in the laboratory for a number of molecules in several different environments (d'Hendecourt et al. 1986; Sandford et al. 1988; Sandford & Allamandola 1990; Hudgins et al. 1993). In Ch. 3, new results are presented for the absorption strengths of H_2O, CO, and CO_2 using techniques developed in the Leiden laboratory.

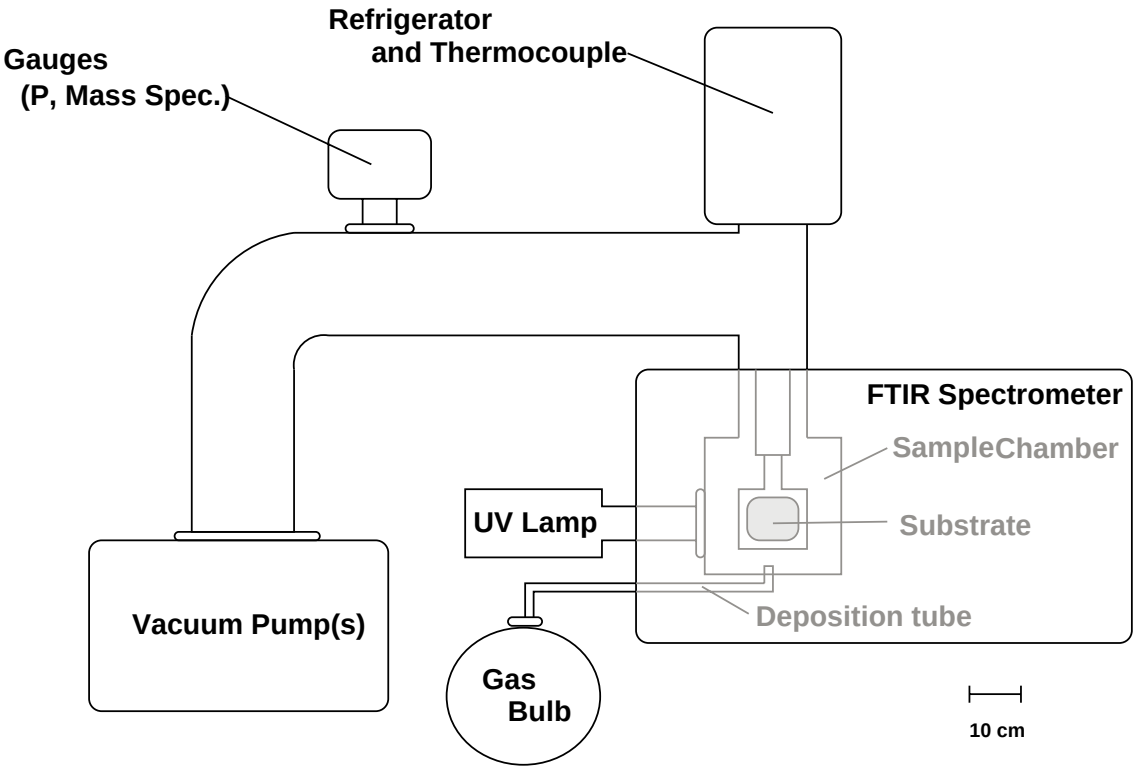

Figure 2.1: A typical laboratory astrophysics vacuum system (approximately to scale).

The chemical dynamics of icy grain mantles may also be understood through laboratory study. Simple mixtures of only a few molecules (i.e. H_2O:NH_3:CH_4), after undergoing UV processing and heating, lead to very complex mixtures, whose IR features resemble those of the organic refractory molecules observed in the ISM (e.g. Grim 1988; Schutte 1988).

2.2 Vacuum System

In this section, I describe the equipment set-up used in the experiments of Chs. 3 and 4. The system is similar to those previously used to study ice analogs (Hagen, Allamandola, & Greenberg 1979; Allamandola, Sandford, & Valero 1988; Hudgins et al. 1993), with some modifications. A schematic of a typical laboratory set-up is shown in Fig. 2.1.

The ice sample chamber (Fig. 2.2) is situated within the sample compartment of an IR spectrometer (Bio-Rad FTS 40A). The chamber has four ports– two KBr

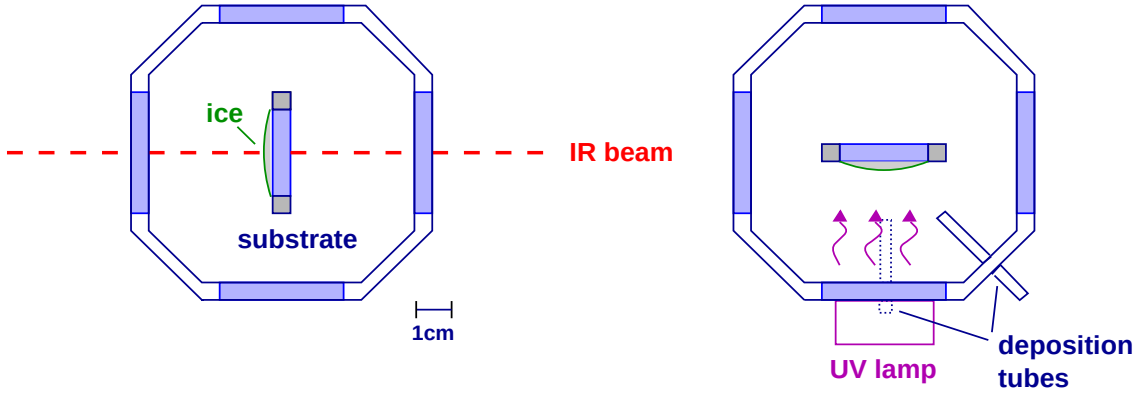

Figure 2.2: Cross section of the sample chamber, viewed from above and to scale. In (a), the substrate is positioned perpendicular to the infrared beam of the spectrometer, for acquiring spectra. In (b), the substrate is positioned for UV photolysis and/or sample deposition.

windows which transmit the IR beam of the spectrometer, one MgF_2 window transparent to the UV radiation used to process the ice samples, and one glass window for visual monitoring. An IR-transmitting substrate (CsI) is mounted in the vacuum chamber and may be cooled by a closed-cycle helium refrigerator (expander, Air Products Displex DE-202; compressor module, Air Products 1R04W-SL) to a minimum temperature of $T \simeq 14\,K$. The temperature of the substrate is continuously adjustable between this and room temperatures by a resistive heater element. The temperature is monitored by a chromel-Au thermocouple with an accuracy of 2 K.

The stainless steel chamber is sealed with Viton O-rings and is evacuated by a turbo-molecular pump (Pfeiffer/Balzers TPH170), backed by a rotary pump (Pfeiffer/Balzers DUO016B). A liquid nitrogen (LN_2) trap between the two pumps prevents any rotary pump oil from back streaming into the system. Ion and thermocouple pressure gauges, placed between the sample chamber and the turbo pump, monitor the internal pressure. The walls of the vacuum system are externally heated (between experiments) in order to remove any gases trapped in the metal. After about two days of pumping and externally heating to $\sim 80\,C$, a vacuum of 5 to 10×10^{-8} mbar could be obtained. The residual gases at this pressure were analyzed by IR spectroscopy after collection on the substrate at 14 K. They were found

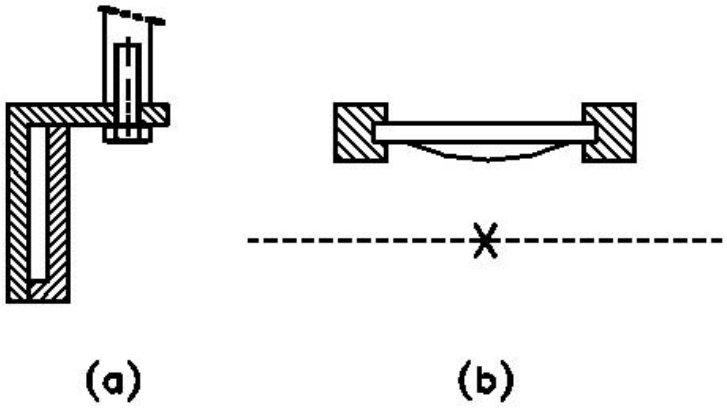

Figure 2.3: Diagram of the substrate holder used in these experiments, showing a side view of the 0.9 cm off-axis mounting of the substrate (a), so that it may be turned completely out of the infrared beam (b, top view; the beam is represented by the dotted line, and the cross denotes the rotation axis)

to consist mainly of H_2O accreting at a rate of $2\times 10^{12}\,\mathrm{cm^{-2}\ s^{-1}}$ (corresponding to a layer growth of $0.002\,\mu\mathrm{m\ s^{-1}}$), with additional organic contaminants accreting at about half this rate.

The substrate holder can be rotated without breaking the vacuum. During an experiment, the substrate is rotated between two positions which are 90 degrees apart, as illustrated in Figs. 2.2 and 2.3. In Position (a), when the substrate is perpendicular to the spectrometer's IR beam, a transmission spectrum of the substrate (and ice sample) can be obtained. The spot size of the infrared beam on the CsI substrate is 0.6 cm in diameter. The second position enables the deposition of an ice sample through a deposition tube onto the cold substrate, and/or the UV irradiation of an ice sample. Moreover, the substrate holder used in these experiments was constructed such that the substrate is mounted 0.9 cm away from the rotation axis. Therefore, when the substrate is rotated by 90 degrees into Position (b), the infrared beam may pass unimpeded through the sample chamber (Fig. 2.3). This allows a reference spectrum to be collected at any moment during the experiment. Use of such reference spectra greatly improves the baseline stability of the infrared spectra (§ 2.4).

Additionally, the chamber used in these experiments has been equipped with

two independent deposition tubes, each directed at the center of the substrate from a distance of 2.1 cm. For each deposition system, the gas flow from a storage bulb (§ 2.3) to the vacuum system is regulated by a variable leak valve (Leybold-Heraeus 28341), and each leak valve is equipped with shut-off and regulation valves. The binary mixtures described in Ch. 3 were produced by simultaneous deposition of each component through the separate tubes. The homogeneity of these samples was checked using the aperture of the IR source to vary the diameter of the spectrometer beam incident on the sample. Samples were found to be $\gtrsim 90\,\%$ homogeneous inside a 1.2 cm diameter.

2.3 Gas Bulb Preparation

Bulbs for individual gases were prepared in a glass vacuum manifold, evacuated through an oil diffusion pump (Edwards Diffstack Series Model 63) backed by a rotary mechanical pump (Edwards BS2212). Back streaming of pump oil into the system is prevented by a LN_2 cold trap located between the line and the pumps. The pressure in the line can be monitored in many ranges with an ion gauge, a thermocouple gauge, and a diaphragm manometer. The system is heated under vacuum to clean it between preparation of different samples.

Species which are gaseous at room temperature are released from their container into the gas bulb through the line. If more than one gas component is desired in the same bulb, an over-pressure of the next gas (determined by the ideal gas law) is subsequently released into the bulb. Molecules such as H_2O or CH_3OH, which are liquids at room-temperature, are first frozen by LN_2 and any dissolved volatile gases are removed by pumping. They are then allowed to liquify, and evaporate into the line and bulb. Certain molecules such as formaldehyde polymerize at room temperature, therefore they must first be collected and stored in a LN_2 trap by heating and "cracking" them from a powdered form of their polymer. To deliver these species through the deposition tubes, the LN_2 trap is replaced with a "slush bath" of a liquid with a freezing/melting temperature of ~ 150 K (such as pentane), thereby evaporating the gas without polymerizing it.

2.4 Measurement of Spectra

A single scan consists of an *interferogram*, the measure of detector output as a function of the optical path length within the spectrometer (Fig. 2.4). A moving mirror mounted on an air gasket is driven by a motor to obtain data across several centimeters. A single-beam spectrum is derived by taking the power spectrum (Fourier transform) of the interferogram. Hence, interferograms measured as functions of path length (e.g., cm), convert to power spectra as functions of wavenumber (e.g., cm^{-1}; Fig. 2.4).[3] In order to obtain a high signal-to-noise in the final spectrum, many scans (~ 100 at a time) are averaged together before taking the Fourier transform. The time to take one spectrum of 100 scans is ~ 3 min. The single-beam spectra described here are taken from $\nu = 4400$ to $400\,\mathrm{cm}^{-1}$ ($\lambda = 2.3$–$25\,\mu$m) at a resolution of $1.0\,\mathrm{cm}^{-1}$ (the width of an unresolved line).

To produce the transmission spectrum, $T(\nu)$, of a sample ice, single-beam spectra are taken before deposition, $I_0(\nu)$, and after deposition, $I(\nu)$. $T(\nu)$ is obtained by their ratio:

$$T(\nu) = \frac{I(\nu)}{I_0(\nu)}, \tag{2.1}$$

(Fig. 2.4). However, the total column density of a material in a spectrum is proportional to $1 - \log T(\nu_0)$ (where ν_0 is the central frequency of an absorption feature), and so spectra are commonly presented in *absorbance* units $\alpha(\nu)$:[4]

$$\alpha(\nu) = -\log_{10} T(\nu) = -\log_{10}\left[\frac{I(\nu)}{I_0(\nu)}\right], \tag{2.2}$$

(Fig. 2.4).

In some cases, especially when measuring spectra after gradual warm-up of the ice sample, the time between obtaining the background and the sample may become large– perhaps on the order of hours. Due to inevitable spectrometer instabilities, such as in the source temperature and in the alignment of the interferometer, this

[3] It is the convention in chemistry literature to present laboratory spectra as functions of "frequency" in units of *wavenumber*, as opposed to wavelength units or the proper frequency units of Hz.

[4] It is also the convention in chemistry literature to use absorbance units, α, as opposed to *optical depth* units, τ, preferred by astronomers ($\tau = -\ln T$). However, the two units only differ by a constant multiplicative factor of $\ln 10$ (=2.303), and at every value of ν, $\tau(\nu) = \ln 10 \cdot \alpha(\nu)$.

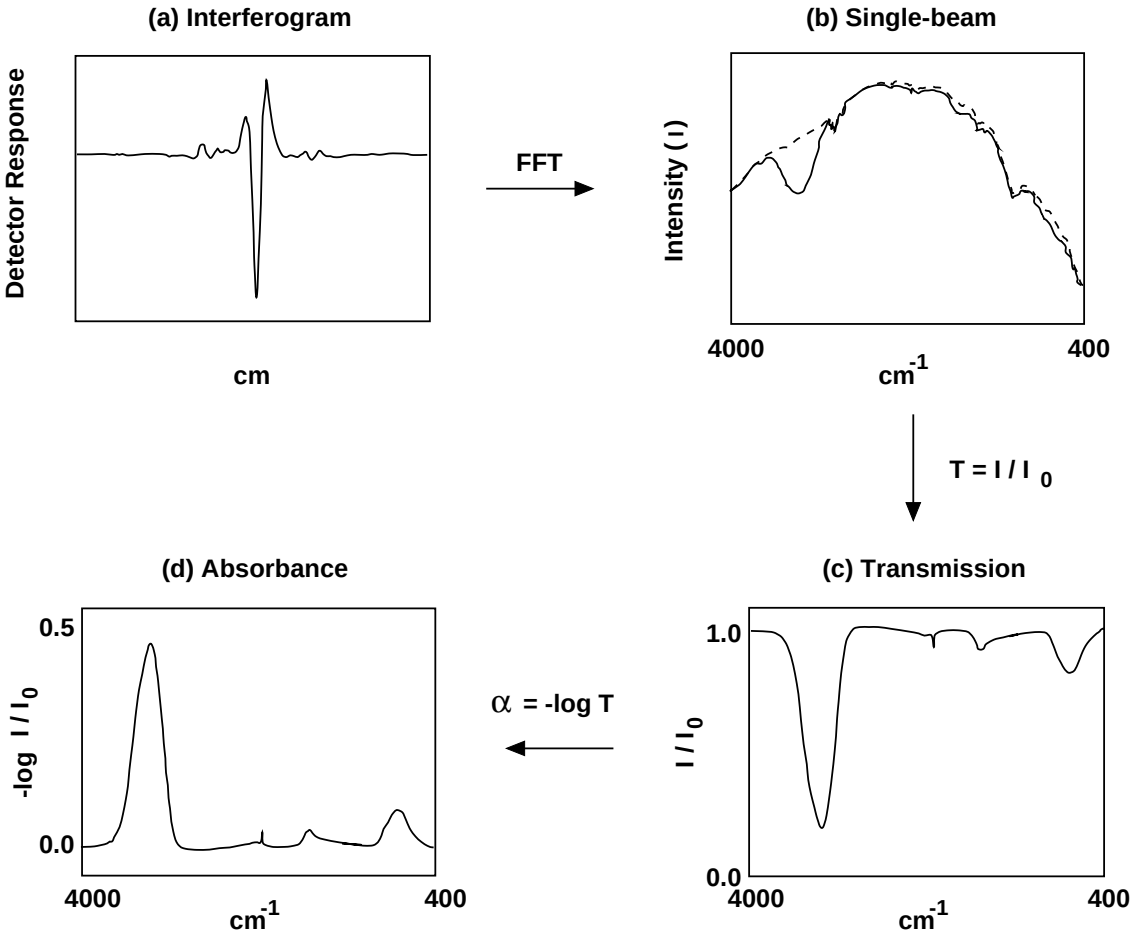

Figure 2.4: Evolution of lab data into absorbance spectra. In (b), the dashed line represents I_0, the continuum used to derive the curves in (c) and (d). Lab data from Ch. 3.

can lead to the appearance of some spurious spectral structure and deviation of the spectral baseline from zero absorbance. To prevent this, additional single-beam spectra can be obtained just after the background spectrum (at time t_1) and just after the sample spectrum (at time t_2) with the substrate in Position (b) (Fig. 2.3), i.e., with the infrared beam passing unimpeded through the vacuum chamber (an "empty" spectrum, I_E). The desired sample absorbance spectrum is then obtained from

$$\alpha(\nu) = -\log_{10}\left[\frac{I(\nu)}{I_E(\nu)}\right]_{t=t_2} + \log_{10}\left[\frac{I_0(\nu)}{I_E(\nu)}\right]_{t=t_1}. \tag{2.3}$$

In effect, a "spectrum" representing the change in spectrometer stability since the original ice deposition is subtracted from the current ice's spectrum (compare

Eqs. 2.2 and 2.3), creating a much stabler baseline.

The column density N (in units of cm^{-2}) of an ice component contributing to absorption feature i is directly proportional to the area underneath feature i (when measured in absorbance or optical depth units). Hence,

$$N = \frac{\int_i \tau(\nu) d\nu}{A_i}, \tag{2.4}$$

where $\tau(\nu)$ is the optical depth spectrum, A_i is the strength (or integrated absorbance cross section) of feature i (in units of cm molec^{-1}), and the integration is taken over the frequency range of i using an appropriate baseline. Values for A_i are measured in the laboratory (Ch. 3).

CHAPTER 3
THE INFRARED ABSORPTION STRENGTHS OF H_2O, CO, & CO_2 IN LABORATORY ANALOGS OF INTERSTELLAR ICE MIXTURES*

"Through measurement to knowledge."

Kamerlingh Onnes[5]

Infrared spectroscopic observations toward objects obscured by dense cloud material show that H_2O, CO and, likely, CO_2 are important constituents of interstellar ice mantles (Ch. 1). In order to accurately calculate the column densities of these molecules, it is important to have good measurements of their IR absorption strengths in astrophysical ice analogs. In this Chapter, I present the results of laboratory experiments to determine these absorption strengths. Improved experimental methods, relying on simultaneous independent depositions of the subject and dilutant molecules, have led to accuracies better than a few percent. The temperature behavior of the CO and H_2O IR absorption strengths have also been studied. In contrast with previous work on this subject, the strengths of the CO, CO_2, and H_2O IR features are found to depend only weakly on the composition of the ice matrix, and the reversible temperature dependence of the CO feature is found to be weaker than previously measured for a mixture of CO in H_2O.

In § 3.2, I describe the experimental methods developed for these experiments. In § 3.3, I summarize the absorption strength measurements for H_2O, CO, and CO_2 in various binary mixtures with polar and nonpolar molecules. Finally, in § 3.4, I discuss the results and their astrophysical implications.

*The results presented in this chapter have been published in modified form by Gerakines et al. (1995).

[5]Translated from the original Dutch: *"Door meten tot weten."*

3.1 Introduction

The abundances of ices in the polar and nonpolar phases of ice mantles described in § 1.3 provide important clues to the chemical processes in dense interstellar clouds, and therefore it is of importance to accurately measure the absorption strengths of their IR features. The goal of this Chapter is to provide new, more accurate measurements of the absorption strengths of solid H_2O, CO and CO_2, so that their interstellar abundances may be determined with more confidence.

Although H_2O appears to be the most abundant molecule in the polar phase (§ 1.2), the presence of nonpolar species such as CO and CO_2 could influence the strength of its IR absorptions. Specifically, the resulting break-up of the hydrogen bonding network could weaken the intensity of the O–H stretching feature of fully H-bonded H_2O at $\nu = 3280\,\mathrm{cm}^{-1}$ ($\lambda = 3\,\mu$m; Hagen & Tielens 1981).[6] As of yet, H_2O has not been observed in the nonpolar ice.

3.2 Experimental Procedures

3.2.1 Previous Studies

Previous methods of measuring absorption strengths for species in a mixed ice involved the preparation of several gases within a single gas container. Components are added one after another, using the ideal gas law to convert pressures to abundances (see § 2.3). This mixture is then deposited onto a cold substrate and it is assumed that the molecular abundances in the ice sample equal the gas abundances in the container. The ice abundances are then used to convert the integrated optical depths to IR absorption strengths, either (i) by measuring the thickness of the ice directly by counting the interference fringes produced by a laser directed at the sample (this method also requires knowledge of the ice density; d'Hendecourt et al. 1986; Hudgins et al. 1993), or (ii) by assuming that the absorption strengths of the dominant component are equal to those in a pure sample and using these to calibrate the other features (Sandford et al. 1988; Sandford & Allamandola 1990). (i) and (ii) each rely heavily on the assumption that the compositions of the ice

[6] In this Chapter, absorption features will be referred to by their peak frequency in units of cm^{-1}, with the corresponding wavelength value in units of μm listed in parenthesis: e.g., "the $3280\,\mathrm{cm}^{-1}$ ($3\,\mu$m) feature of H_2O."

sample and of the gas mixture are equal. However, there are several caveats to this assumption. First, a small change in temperature could significantly influence the amount of gas-phase H_2O inside the bulb if it is made with H_2O close to its vapor pressure (which has a strong dependence on temperature: between 18 and 23 C, it varies from 20.6 to 28.1 mbar). Second, mixing of the different gases in the bulb may be incomplete. Finally, the deposition rate of a molecule is proportional to its thermal velocity, which depends on the molecular mass, i.e., $v_{\mathrm{therm}} \propto m^{-\frac{1}{2}}$. This effect could give rise to a significant difference in the compositions of the gas mixture and of the ice sample if molecules with very different molecular masses are involved. For example, the thermal velocities of H_2O and CO_2 are different by a factor of 1.56.

3.2.2 New Methods

In the new procedures implemented here, these pitfalls have been avoided by the simultaneous deposition of pure gases through separate deposition tubes. An outline of the basic procedure is as follows. In one experiment, a pure ice sample is deposited through a single deposition tube and measured. In the next, this same deposition is repeated *simultaneously* with that of a diluting gas through the second deposition tube. The ratio of the absorption strengths of molecules in the binary ice to those in the pure ice may then be measured, since equal column densities of the subject gas are deposited in each case (pure and mixed). When this ratio has been measured, the absorption strengths in the mixed ice may be calculated using the pure ice strengths, which are accurately known and present in the literature.

The details of this new method of measuring IR absorption strengths is described here. Two gas bulbs, one containing the gas for which the strengths are to be measured (the "subject") and one containing the diluting gas (the "dilutant") are connected to the entries of the two deposition tubes. Before cooling the substrate, flow rates are set with the regulation valve while monitoring the pressure increase within the system, using the following relation:

$$F_i \propto \frac{\Delta P}{\sqrt{m_i}} \ , \tag{3.1}$$

where m_i is the molecular mass of component i, ΔP is the measured pressure increase

within the vacuum system, and F_i is the desired flow rate of component i (e.g., Schutte, Allamandola, & Sandford 1993). In this way, the flow rates through each deposition tube are set independently, based on the desired ratio of the component gases. After setting the flow rates with the regulation valves, flows are controlled exclusively with the shut-off valves. From later spectroscopic analysis (§ 2.4) of ices produced by this method of pre-calibration, it is found that the flow rates reproduce from experiment to experiment within 3 %.

After calibration, the substrate is cooled down to 14 K, and a deposition is made of the subject gas. After obtaining the IR spectrum, the substrate is heated until the sample sublimes and then re-cooled. Next, the subject gas and the dilutant are deposited simultaneously for the same length of time as in the first deposition: this results in a binary ice sample that contains the same number of subject molecules. The column density N of an ice component and the integrated optical depth of its feature i relate as shown in Eq. (2.4). Thus, the ratio of the strengths in the binary and in the pure ice can be found simply from the ratio of the integrated optical depths in the two samples, provided that the subject material makes up $\lesssim 10\,\%$ of the binary ice. On the other hand, if the subject:dilutant ratio is large ($\gtrsim 10\,\%$), the dilutant's absorption strength may be affected by presence of the subject species, and so an additional sample of pure dilutant is made as a final step. Then the exact composition of the binary ice may be determined from the integrated optical depths measured in the two pure samples using absorption strengths from the literature.

The ice samples in these experiments had the approximate composition of dilutant:subject = 20:1 or 1:1. Due to uncertainties involved in pre-calibrating the flows (above), the actual compositions of the ice samples, as measured from the IR spectra, could differ by up to a factor of two from those intended, although the deviation was typically no more than $\sim 30\,\%$. Since O_2 is IR-inactive, the composition of the O_2-containing binary ices could only be assessed from the increase in pressure at room temperature by the O_2 flow (Eq. 3.1). Thus, for these ices there can be an error in the listed composition of about a factor of two (of course, this does not introduce any uncertainty in the measurement of $A/A_{\rm pure}$).

The total deposition rate for the binary ices was typically $\sim 4 \times 10^{15}\,\mathrm{cm^{-2}\ s^{-1}}$ for the 20:1 ices and $\sim 1 \times 10^{15}\,\mathrm{cm^{-2}\ s^{-1}}$ for the 1:1 ices (corresponding to thickness growth rates of ~ 4 and $1\,\mu\mathrm{m\,s^{-1}}$, respectively). Deposition rates of the subject gases were $\sim 2 \times 10^{14}\,\mathrm{cm^{-2}\ s^{-1}}$ when producing a 20:1 ice sample and $\sim 5 \times 10^{14}\,\mathrm{cm^{-2}\ s^{-1}}$ when producing a 1:1 ice sample. With these deposition rates, the contamination due to mixing of the residual gases into the ice samples (§ 2.2) ranged from ~ 0.1 to 2 %. Deposition times were 6 min for the 1:1 ices and 3 min for the 20:1 ices, the resulting in thicknesses of ~ 0.2 and $0.1\,\mu$m respectively.

Depositions at a slightly increased temperature of 20 K were made in order to check the sticking of the molecules on the substrate: if no decrease in sticking at the higher temperature is found, then sticking can be assumed to equal 100 % (Sandford & Allamandola 1990). In all cases, sticking was found to equal unity.

Pressures used in the bulbs containing H_2O were limited to a maximum of 10 mbar, well below its room temperature vapor pressure of ≈ 20 mbar. The effects of substantial sticking of H_2O on the walls of the bulb and the temperature dependence of the H_2O vapor pressure are thus avoided.

3.3 Results

Integrated optical depths (in units of $\mathrm{cm^{-1}}$) were measured from the absorbance spectra by choosing an appropriate baseline for the feature in question. For the features of pure ice and for most ices without H_2O, a linear baseline gave sufficient results. The absorptions of H_2O are strong and broad, and they dominate the spectra of H_2O-containing mixtures. Most CO_2 and CO absorptions lie on top of these structures, and in order to define good baselines in these cases, polynomial fits were made to the underlying H_2O structures. In general, good fits were obtained for polynomials of order 2 or 3. An average of measurements was taken when more than one polynomial fit well. An example of an absorption for which the underlying H_2O feature created some difficulty in baseline determination is the CO_2 660 $\mathrm{cm^{-1}}$ (15.2 μm) feature, which lies on the low-frequency side of the H_2O 760 $\mathrm{cm^{-1}}$ (13 μm) feature. Two polynomial fits of the underlying H_2O feature are shown in Fig. 3.1 for an H_2O:CO_2 = 24:1 mixture: the resulting CO_2 column densities differ by 14 %.

Table 3.1: IR absorption strengths A of pure H_2O, CO, and CO_2 ices after deposition at T = 14 K and CO_2 after warm-up to T = 60 and 100 K.

Ice	Mode	Position [cm^{-1}] ([μm])	A_{14}[a]	A_{60}/A_{14}	A_{60}[a]	A_{100}/A_{14}	A_{100}[a]
H_2O	O–H stretch	3280 (3.045)	20[b]				
	O–H bend	1660 (6.024)	1.2				
	libration	760 (13.16)	3.1				
CO	$^{12}C\equiv O$ stretch	2139 (4.675)	1.1[c]				
	$^{13}C\equiv O$ stretch	2092 (4.780)	1.3				
CO_2	(ν_3) $^{12}C{=}O$ stretch	2343 (4.268)	7.6[d]	0.98	7.4	0.97	7.4
	(ν_3) $^{13}C{=}O$ stretch	2283 (4.380)	7.8	0.94	7.3	0.92	7.2
	(ν_2) O=C=O bend	660,665 (15.15,15.27)	1.1	1.03	1.1	1.04	1.1
	($\nu_1 + \nu_3$) combination	3708 (2.697)	0.14	1.05	0.15	1.08	0.15
	($2\nu_2 + \nu_3$) combination	3600 (2.778)	0.045	1.22	0.055	1.20	0.054

[a] in units of 10^{-17} cm $molec^{-1}$.
[b] Hagen & Tielens 1981.
[c] Jiang, Person, & Brown 1975.
[d] Yamada & Person 1964.

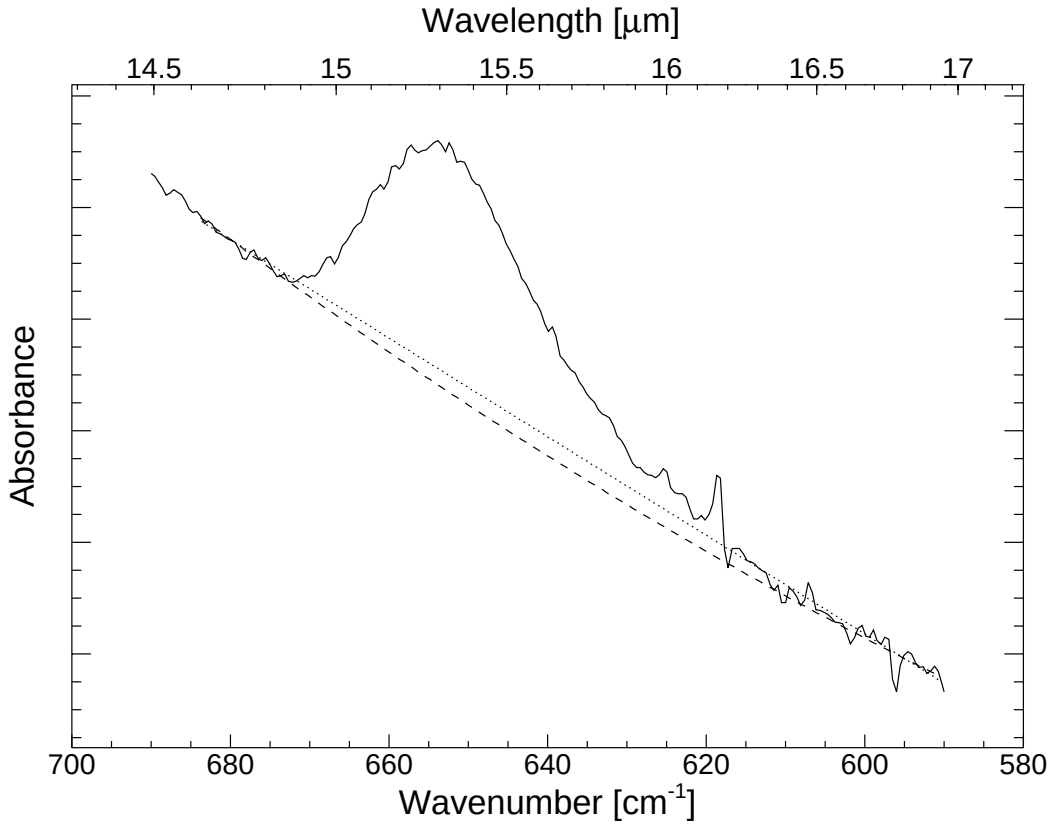

Figure 3.1: The 660 $\mathrm{cm^{-1}}$ (15.2 μm) feature of $\mathrm{CO_2}$ in an $\mathrm{H_2O}$:$\mathrm{CO_2}$ = 24:1 mixture demonstrates the uncertainty involved in producing a fit to the underlying feature of $\mathrm{H_2O}$. Dotted line– 1st order polynomial fit to the $\mathrm{H_2O}$ absorption; dashed line– 2nd order fit in the same regions. Resulting $\mathrm{CO_2}$ column density measurements differ by 14 %.

3.3.1 Pure ices

Table 3.1 lists the IR absorption strengths at 14 K for the pure ices used in these experiments. For each molecule, values for the strongest features have been taken from the literature (Yamada & Person 1964; Jiang, Person, & Brown 1975; Hagen & Tielens 1981) and used to calculate the strengths for the other features by scaling the relative integrated optical depths (for the features of ^{13}CO and $^{13}\mathrm{CO_2}$, the terrestrial isotopic ratio of $^{12}\mathrm{C}/^{13}\mathrm{C} = 89$ has been assumed). Table 3.1 also lists measurements of pure $\mathrm{CO_2}$ at higher temperatures that were obtained by depositing the ice at 14 K and subsequent stepwise heating of the ice sample at a rate of $\sim 2\,\mathrm{K\ min^{-1}}$ (an IR spectrum was taken at each step). Only a weak temperature

Table 3.2: Measured values of $A/A_{\rm pure}$ and resulting absorption strengths, A (in units of 10^{-17} cm molec^{-1}), for CO in binary ices with H_2O, O_2 and CO_2 at T = 14 K. Uncertainties greater than 5% are listed.

	^{12}C≡O stretch		^{13}C≡O stretch	
Ice	$A/A_{\rm pure}$	A	$A/A_{\rm pure}$	A
H_2O:CO = 26:1	0.97	1.1	0.63 ± 0.3	0.82 ± 0.4[a]
H_2O:CO = 2.1:1	0.99	1.1	0.78 ± 0.3	1.0 ± 0.4[a]
O_2:CO = 20:1[b]	1.13	1.2	1.18 ± 0.1	1.5 ± 0.1
O_2:CO = 1:1[b]	1.04	1.1	1.00	1.3
CO_2:CO = 17:1	1.04	1.1	0.87 ± 0.1	1.1 ± 0.1
CO_2:CO = 0.8:1	1.10	1.2	1.04	1.4

[b] Measurement contains a large uncertainty due to underlying features of H_2O.
[c] Listed composition is uncertain by a factor of 2 (§ 3.3.2).

dependence was revealed for each of the CO_2 IR features.

Peak positions in both cm^{-1} and μm are listed for the pure ices in Table 3.1 (cf. Sandford et al. 1988; Sandford & Allamandola 1990). For purposes of identification, each feature is denoted by its position in the pure ice. Values in mixed ices were found to agree with those of Sandford et al. (1988) and Sandford & Allamandola (1990), and the reader is referred to these works for a complete listing of absorption positions in binary mixtures.

3.3.2 CO mixtures

The measurements of $A/A_{\rm pure}$ and the resulting absorption strengths for the ^{13}C≡O and ^{12}C≡O fundamental stretching modes are shown in Table 3.2 for CO mixed with H_2O, O_2, and CO_2. Errorbars were estimated using several (equally valid) baseline choices (§ 3.3): only errors larger than 5 % are listed. Errors due to spectral noise are negligible (i.e., $\lesssim$ 1 %), even for the weakest features. For ^{12}CO, the value of $A/A_{\rm pure}$ does not deviate from unity by more than 13 % in all experiments studied. The values for ^{13}CO in H_2O mixtures contain substantial baseline errors due to the small size of its absorption feature and its position on top of a broad H_2O feature. Within the errorbars, however, the values of $A/A_{\rm pure}$ for ^{13}CO in all mixtures do not significantly differ from those in a pure CO ice.

Table 3.3: Reversible temperature dependence of the CO stretching feature in an H_2O:CO = 30:1 mixture. A is in units of 10^{-17} cm molec^{-1}.

T [K]	$A/A_{14\,K}$	A
14	1.0	1.1
40	0.97	1.1
60	0.94	1.0
80	0.88	0.96
90	0.83	0.92

The reversible temperature dependence of the $^{12}C{\equiv}O$ absorption strength was also studied in the H_2O:CO = 26:1 ice sample following the methods of Schmitt, Greenberg, & Grim (1989). Measuring the *irreversible* component of the temperature dependence is impossible for CO, since a fraction of CO ice starts to sublime when the sample temperature is raised only to 25 K (Schmitt, Greenberg, & Grim 1989; Sandford et al. 1988).

The initial sample was heated to 115 K and then annealed for 20 min to remove any such weakly-bound CO. The ice was then cooled slightly to 100 K and held there for 5 min, in order to stop sublimation and to pump away any gas-phase CO left in the system. Finally, the ice was re-cooled to 14 K and measured. After annealing and re-cooling, the ice composition was found to equal H_2O:CO = 30:1 (assuming that $A_{CO,14\,K} = 1.1 \times 10^{-17}$ cm molec^{-1}, as for the unannealed ice). As a check of CO re-condensation during the cool-down, the sample was kept at 14 K for 10 min and then re-measured. No new condensation was found in the ice sample. The sample was then warmed up and measured in T steps from 14 to 90 K. In order to check for any further sublimation of CO during this second warm-up sequence, the sample was once again cooled to 14 K and the CO absorption measured: no new sublimation was found. Measured values of A are listed in Table 3.3 and plotted in Fig. 3.2. As in Schmitt, Greenberg, & Grim (1989), a clear temperature dependence was found. Results show that the absorption strength drops by 17 % (from 1.1×10^{-17} to 9.1×10^{-18} cm molec^{-1}) when the temperature is raised from 14 to 90 K.

3.3.3 CO_2 mixtures

Table 3.4: Measured values of $A/A_{\rm pure}$ and resulting absorption strengths, A (in units of 10^{-17} cm molec^{-1}), for CO_2 features in binary ices at T = 14 K. Uncertainties greater than 5% are listed.

	(ν_3) ^{12}C=O stretch		(ν_3) ^{13}C=O stretch		(ν_2) O=C=O bend		($\nu_1 + \nu_3$) combination		($2\nu_2 + \nu_3$) combination	
Ice	$A/A_{\rm pure}$	A	$A/A_{\rm pure}$	A	$A/A_{\rm pure}$	A	$A/A_{\rm pure}$	A	$A/A_{\rm pure}$	A
H_2O:CO_2 = 24:1	0.94	7.1	0.80 ± 0.1	6.2 ± 0.8	1.38 ± 0.2	1.5 ± 0.2	...[a]	...	...[a]	...
H_2O:CO_2 = 1.6:1	1.00	7.6	0.98	7.6	1.37 ± 0.2	1.5 ± 0.2	0.83 ± 0.2	0.12 ± 0.03	0.72 ± 0.3	0.032 ± 0.01
O_2:CO_2 = 20:1[b]	0.95	7.2	0.79 ± 0.1	6.2 ± 0.8	0.85	0.94	0.85	0.12	1.02	0.046
O_2:CO_2 = 1:1[b]	1.05	8.0	1.10	8.6	0.91	1.0	1.00 ± 0.1	0.14 ± 0.01	1.36	0.061
CO:CO_2 = 29:1	1.09	8.3	1.00	7.8	0.96	1.1	2.15	0.3	1.58	0.071
CO:CO_2 = 1.3:1	1.01	7.7	0.99	7.7	0.88	0.97	1.04 ± 0.1	0.15 ± 0.01	1.33 ± 0.2	0.06 ± 0.01

[a] Unobservable due to overlap with strong H_2O feature.
[b] Listed composition is uncertain by a factor of two (§ 3.3.2).

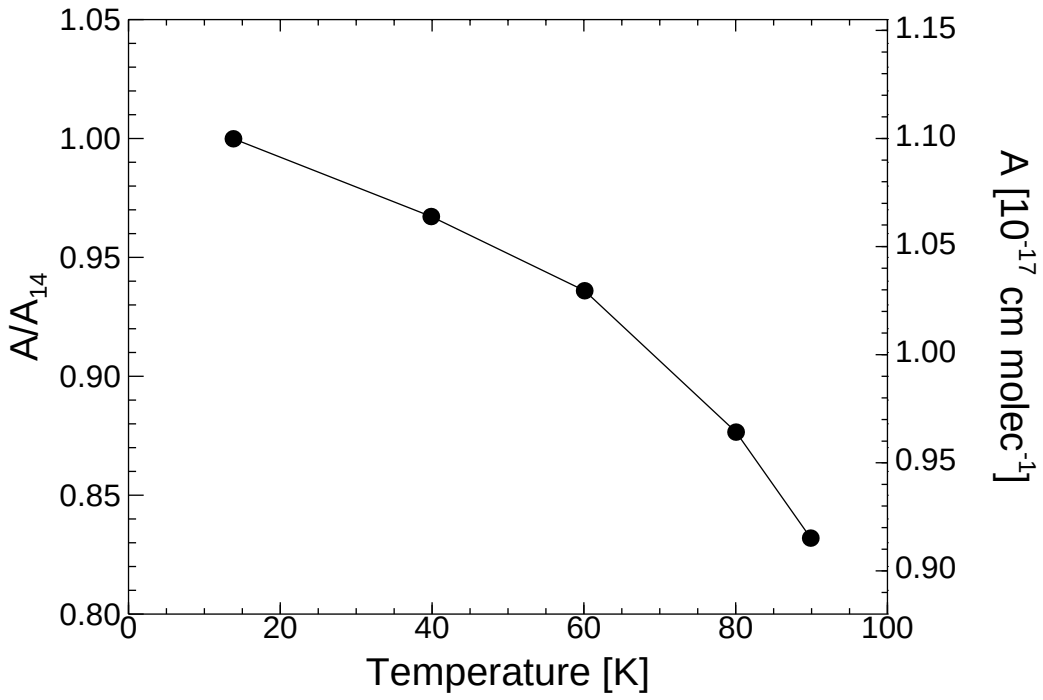

Figure 3.2: The reversible temperature dependence of the CO stretching feature in an H_2O:CO = 30:1 mixture. The absolute scale assumes $A_{CO,14\,K} = 1.1 \times 10^{-17}$ cm molec^{-1}, as in the ice sample before annealing.

Table 3.4 presents the absorption strengths of the CO_2 IR features in H_2O, O_2, and CO mixtures. Errors due to baseline uncertainties are listed whenever they exceed 5 % (as in Table 3.2). The temperature dependence of the CO_2 absorptions in an H_2O matrix were studied by warm-up of the deposited ice sample, in the same manner as for pure CO_2 (§ 3.3.1). No significant temperature dependence was found (at 100 K, the strengths of all CO_2 features measured deviated by less than 3 % from their values at 14 K). Hence, only results of measurements at 14 K are listed in Table 3.4. As with CO, the CO_2 absorption strengths have been found to depend only weakly on ice composition: the strength of the main stretching feature of CO_2 varies by less than 10 % in the ices studied. The strengths of the $^{13}CO_2$ feature at 2283 cm^{-1} (4.38 μm) and CO_2 bending mode at 660 cm^{-1} (15.2 μm) deviate by a somewhat larger amount (up to 21 and 37 % respectively), but these measurements contain considerable error (up to 20 %). Only the strengths of the two weak CO_2 combination modes show any clear dependencies on ice composition

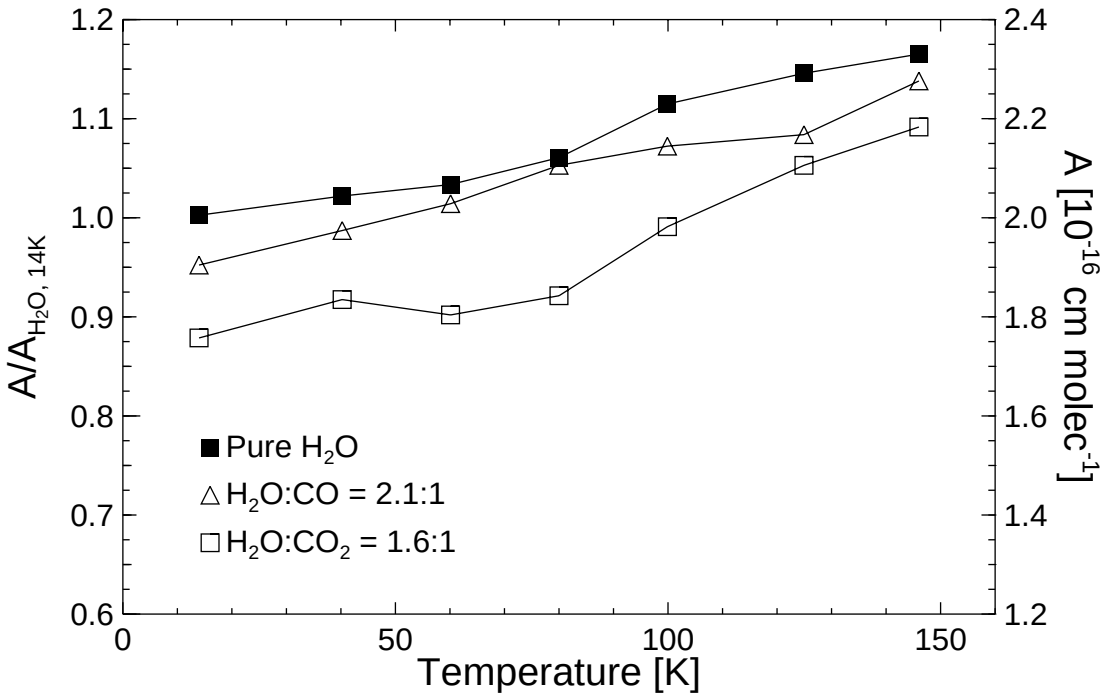

Figure 3.3: Measured integrated optical depth of the stretching feature of H_2O in mixtures with CO and CO_2 as a function of temperature. Left-hand y-scale is relative to the strength of the corresponding feature of pure H_2O at T = 14 K (Table 3.5). Solid squares– pure H_2O; empty triangles– H_2O:CO = 2.1:1; empty squares– H_2O:CO_2 = 1.6:1.

(compare columns of Table 3.4).

In order to estimate the influence of residual gases depositing within the ice samples (§ 2.2), an H_2O:CO_2 = 20:1 experiment was performed with a factor of 4 increase in deposition velocity. Since the residual gas deposition rate is constant to a reasonable approximation over the course of an experiment, a higher sample deposition rate should produce an ice with correspondingly fewer contaminating molecules per unit volume (in this case, 4 times fewer). The ratios of $A/A_{\rm pure}$ obtained in this experiment deviated by less than 1 % from those at the lower deposition rate, indicating that the residual gas condensation has a negligible effect on the results.

3.3.4 H_2O mixtures

Results of diluting H_2O ices with CO and CO_2 molecules are presented in Table 3.5, and the temperature dependencies of the three H_2O IR features are plotted

Table 3.5: Measured values of A_{H_2O} in mixtures with CO and CO_2, listed relative to pure H_2O at T = 14 K and in units of 10^{-17} cm molec^{-1}.

T	Pure H_2O		H_2O:CO = 2.1:1		H_2O:CO_2 = 1.6:1	
[K]	$A/A_{H_2O,14\,K}$	A	$A/A_{H_2O,14\,K}$	A	$A/A_{H_2O,14\,K}$	A
			O–H Stretching Mode:			
14	1.00	20.0	0.95	19.0	0.88	16.6
40	1.02	20.4	0.99	19.8	0.92	18.4
60	1.03	20.6	1.01	20.2	0.90	18.0
80	1.06	21.2	1.05	21.0	0.92	18.4
100	1.11	22.2	1.07	21.4	0.99	19.8
125	1.15	23.0	1.08	21.6	1.05	21.0
145	1.17	23.4	1.14	22.8	1.09	21.8
			O–H Bending Mode:			
14	1.00	1.20	1.09	1.31	1.21	1.45
40	1.01	1.21	1.08	1.30	1.13	1.36
60	0.98	1.18	1.05	1.26	1.13	1.36
80	1.05	1.26	0.99	1.19	1.15	1.38
100	1.05	1.26	1.01	1.21	1.12	1.34
125	1.09	1.31	1.07	1.28	1.06	1.27
145	1.05	1.26	1.05	1.26	0.99	1.19
			Libration Mode:			
14	1.00	3.10	0.94	2.91	0.81	2.51
40	1.00	3.10	0.96	2.98	0.71	2.20
60	1.00	3.10	0.98	3.04	0.72	2.23
80	1.00	3.10	1.00	3.10	0.83	2.57
100	0.98	3.04	0.95	2.95	0.89	2.76
125	0.97	3.01	0.94	2.91	0.85	2.64
145	0.95	2.95	0.91	2.82	0.82	2.54

in Figs. 3.3–3.5. The stretching feature itself could be measured with a simple straight baseline in all cases, and the side features produced in binary ices were subtracted using a polynomial fit of order 2 or 3 to the wings of the stretching feature. The resultant correction amounted to $\lesssim 2.5\,\%$ of the total absorption strength in all cases. For the 1660 cm^{-1} (6 μm) bending feature, a straight baseline was used through the regions of 1930 to 1980 and 1050 to 1080 cm^{-1} (5.05 to 5.18 and 9.26 to 9.52 μm), and a straight baseline from 500 to 1050 cm^{-1} (9.5 to 20.0 μm)

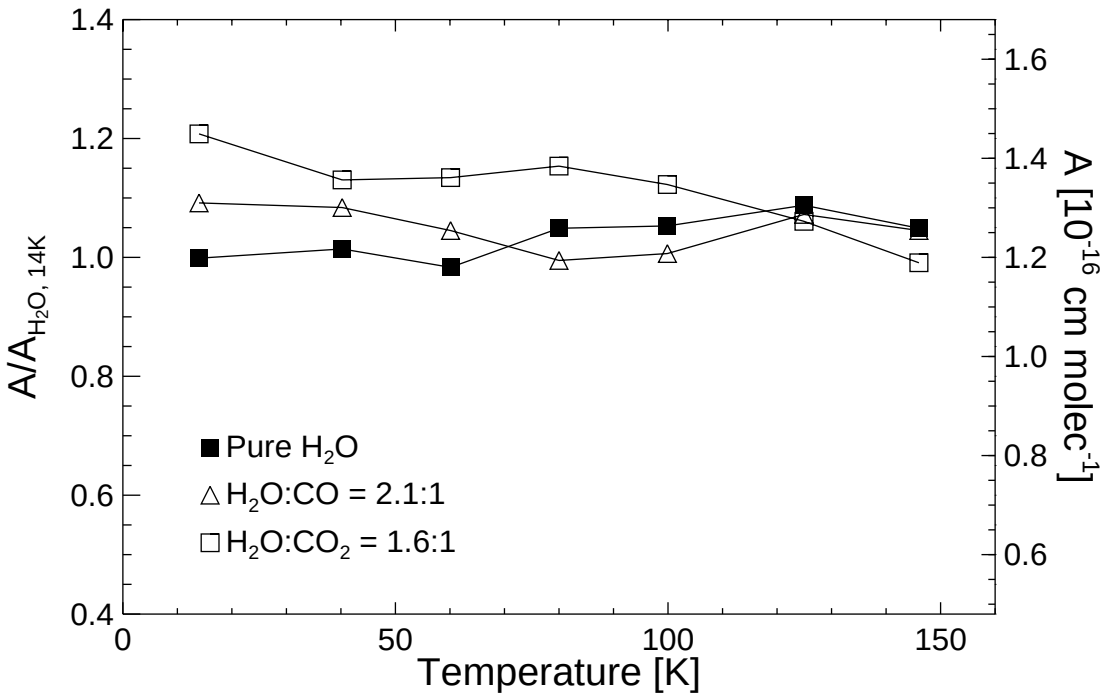

Figure 3.4: As Fig. 3.3, but for the bending mode of H_2O.

was used for the libration feature at $760\,\mathrm{cm}^{-1}$ ($13\,\mu$m). In the H_2O:CO_2 = 1.6:1 mixture, the CO_2 bending mode at $660\,\mathrm{cm}^{-1}$ ($15.2\,\mu$m) totally obscures the shape of the long-wavelength side of the H_2O libration feature. In this case, the H_2O feature was assumed to be symmetric, and twice the measured integrated optical depth from its peak position at $\sim 770\,\mathrm{cm}^{-1}$ ($13.0\,\mu$m; temperature-dependent) to $1050\,\mathrm{cm}^{-1}$ ($9.52\,\mu$m) was taken as an estimate of its full integrated optical depth.

The O–H stretching feature is slightly reduced in strength in mixtures containing either CO or CO_2 (Fig. 3.3). As the ice is heated, however, the nonpolar molecules begin to diffuse through and escape from the H_2O matrix (Schmitt, Greenberg, & Grim 1989; Sandford et al. 1988), and the $3\,\mu$m feature grows as more H_2O molecules form hydrogen bonds. Just after deposition at 14 K, the $6\,\mu$m feature is slightly strengthened, and the $13\,\mu$m feature is slightly weakened by the new molecule. Both features approach the pure H_2O value as they are heated (Figs. 3.4 and 3.5).

The strength of the $3\,\mu$m O–H stretching mode in a mixture of H_2O:CO = 2.1:1

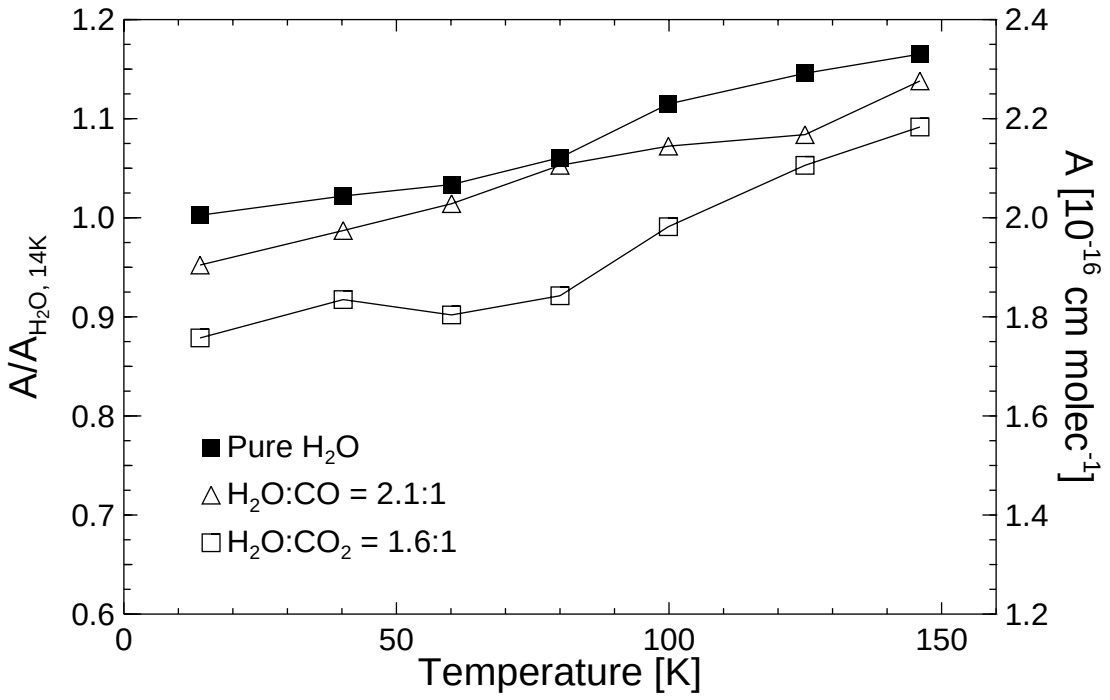

Figure 3.5: As Figs. 3.3 and 3.4, but for the libration mode of H_2O.

is reduced to 95 % of its pure-ice value and to 88 % in an H_2O:CO_2 = 1.6:1 mix (Table 3.5). The effects of dilution on the 3 μm H_2O feature have been studied previously by Greenberg, van de Bult, & Allamandola (1983). Using the statistical concentrations of monomers, dimers, and trimers of a molecule randomly placed within a simple cubic lattice (e.g., Behringer 1958), these authors showed that the 3 μm feature's absorption strength will be related to the H_2O concentration in the mixture (f) by the semi-empirical relation

$$\frac{A}{A_{\rm pure}} = \frac{1 - f_0/f}{1 - f_0}, \tag{3.2}$$

where $f_0 = 0.15$ represents the lower limit on f for producing the 3 μm feature. With $f = 0.68$ and 0.62 (as for the H_2O:CO = 2.1:1 and H_2O:CO_2 = 1.6:1 mixtures), Eq. (3.2) yields $A/A_{\rm pure} = 0.92$ and 0.89, respectively, which are essentially identical to the measured reductions of 95 and 88 % in the H_2O mixtures (Table 3.5). The consistency of these results may indicate that there is good mixing of the subject and dilutant molecules and that there is little diffusion taking place upon deposition

before the molecules become fixed in the ice lattice.

3.4 Discussion

3.4.1 Comparison with previous studies

The absorption strengths determined here for CO and CO_2 diluted in H_2O, O_2, CO and CO_2 show no significant deviation from their corresponding pure-ice values. This contrasts with earlier studies which have shown large increases in A for these molecules diluted in H_2O: a 70 % increase for CO and increases by factors of 2 to 4 for the features of CO_2 (Sandford et al. 1988; Palumbo & Strazzulla 1993; Sandford & Allamandola 1990). Since the errors in these results are in general less than 10 %, it appears that these earlier measurements could be significantly influenced by the problems involved in the deposition methods discussed in § 3.1. On the other hand, the absorption strengths of CO_2 in a CO matrix do agree well with those measured previously (Sandford & Allamandola 1990). Additional careful studies should be performed to study absorption strengths for other astrophysically interesting molecules and to determine the origin of these apparent discrepancies.

Other results in this Chapter show that the 2140 cm^{-1} feature of CO in an H_2O:CO ice has a strong reversible temperature dependence, decreasing in strength by 17 % when the temperature is raised from 14 to 90 K. Earlier measurements by Schmitt, Greenberg, & Grim (1989) showed a considerably larger decrease (33 %) over this temperature range. The difference between these results could possibly be attributed to the use of the specular reflectance method of obtaining IR spectra by Schmitt, Greenberg, & Grim, since it has been shown that measurements with this technique yield different peak absorbances as compared to spectra measured in transmission due to interference losses at the interface between the ice sample and the reflecting block surface (Hagen & Tielens 1981; Kitta & Krätschmer 1983).

3.4.2 Astrophysical implications

These results have several astrophysical implications. First, the abundance of CO in the polar phase of icy grain mantles in dense interstellar clouds becomes 1.7 times larger than previously calculated: toward embedded sources, the amount

of CO in polar ice is then comparable to the amount of CO in nonpolar ice (Tielens et al. 1991; Chiar et al. 1994; Chiar et al. 1998b). Also, the CO_2 column densities as estimated by d'Hendecourt & Jourdain de Muizon (1989) toward three embedded sources all become 3.7 times higher, matching or even exceeding that of CO towards the objects studied.

Next, ices toward embedded sources have been observed with line-of-sight–averaged temperatures of up to $\sim 80\,\mathrm{K}$ (Smith, Sellgren, & Tokunaga 1989). In these cases, the absorption strengths determining the column densities of polar CO should be slightly lower than the value of $1.1\times10^{-17}\,\mathrm{cm\ molec^{-1}}$ appropriate for $\mathrm{T} = 14\,\mathrm{K}$: for an average ice temperature of 70 K, a CO absorption strength of $1.0\times10^{-17}\,\mathrm{cm\ molec^{-1}}$ is more suitable (Fig. 3.2). Finally, in determining H_2O column densities from the 3 and 6 μm interstellar features, the strengths for pure H_2O ice may be used, since the presence of small abundances of nonpolar species in the ice ($\lesssim 30\,\%$) has little influence on its absorption strengths (see Table 3.5 and Figs. 3.3 and 3.4). However, the effects of dilution should become important if the concentration of nonpolar molecules were considerably larger, i.e., $\gtrsim 60\,\%$ (Eq. 3.2; Greenberg, van de Bult, & Allamandola 1983).

3.5 Conclusions

The experiments presented in this Chapter show that the strengths of the CO and CO_2 IR absorption features depend *only weakly* on the composition of the ice mixture in which they are diluted. It is known that the profiles of these features have extremely strong dependencies on ice matrix (Sandford et al. 1988; Sandford & Allamandola 1990), but these results show that their absorption strengths (expressed as total absorption over the features per molecule) remain constant: i.e., an increase in width is compensated by a decrease in depth. The 4.67 μm ($2140\,\mathrm{cm^{-1}}$) feature of CO is a prime example: its width is more than three times greater in an H_2O-dominated ice than in pure CO (Sandford et al. 1988), but the total integrated area under the CO feature in these ices is the same when equal column densities of CO are involved, *despite the overall ice composition*. It has also been shown here (§ 3.3.4) that the strengths of the 3, 6, and 13 μm features of H_2O are only weakly

affected by the presence of CO and CO_2: the change is $\lesssim 20\,\%$ for all three features in ices where the amount of nonpolar species is comparable to the amount of H_2O.

CHAPTER 4
ULTRAVIOLET PROCESSING OF INTERSTELLAR ICE ANALOGS*

> "Why, for example, should a group of simple, stable compounds of carbon, hydrogen, oxygen and nitrogen struggle for billions of years to organize themselves into a professor of chemistry? What's the motive?"
>
> Robert Pirsig

Interstellar ices are chemically processed by ultraviolet (UV) radiation to form complex products, and models of UV photochemistry provide powerful tools for the interpretation of astronomical observations. In this Chapter, I present UV photolysis experiments performed on pure ice samples at T = 10 K, made up of nine astrophysically interesting molecules: H_2O, NH_3, CH_4, CO, CO_2, O_2, N_2, H_2CO, and CH_3OH. Destruction of these species by photochemical processes is discussed, and the cross sections for destruction are estimated (crucial parameters in gas-grain chemical models). New molecules produced during photolysis are identified on the basis of their characteristic infrared (IR) features, and their chemical origins and astrophysical implications are discussed. Rates of formation are also estimated for first-order products. In § 4.2 I describe the procedures unique to these experiments. Results are presented in § 4.3, and the photochemical reaction schemes are considered in § 4.4. The astrophysical implications of this research are discussed in § 4.5.

4.1 Introduction

Molecules in the interstellar environment undergo chemical reactions driven by such forces as cosmic ray ionization, the interstellar radiation field, and shocks due to nearby star formation. Molecules are constantly being destroyed and (re-)formed by

*The results presented in this chapter have been published in modified form by Gerakines, Schutte, & Ehrenfreund (1996).

these processes. A complex chemistry is evident and is supported by new detections of new and complex molecules (§ 1.3). Astronomical observations are complimented by chemical modeling, and all gas-grain chemistry models predict that a population of simple atomic species will eventually evolve into a complex chemistry of large molecules (e.g. Tielens & Hagen 1982; d'Hendecourt et al. 1986; Hasegawa, Herbst, & Leung 1992; Shalabiea & Greenberg 1994). This often involves intricate chemical pathways whose end products bear little resemblance to the initial contents.

The irradiation ratio R is adopted here as a measure of UV dose for convenient comparison between of the expected processing of interstellar ice and the results of simulation experiments. R is defined as the amount of UV photons absorbed per solid H_2O molecule and is calculated assuming an average H_2O UV cross section of $2\times 10^{-18}\mathrm{cm}^2$ ($E_{h\nu} > 6\,\mathrm{eV}$; Okabe 1978). For example, $R = 0.06$ with a UV flux of $1000\,\mathrm{cm}^{-2}\ \mathrm{s}^{-1}$ after $10^6\,\mathrm{yr}$.

In this Chapter, I describe the photochemical behavior of simple interstellar analogs by means of in-situ infrared spectroscopy. Such studies are important for a number of reasons. First, they will help to understand the compositions of interstellar ices. Observations with the Infrared Space Observatory (ISO) in regions obscured from ground-based observers (e.g., $\lambda = 4$–$8\,\mu\mathrm{m}$) call for high-quality data for thorough interpretation. Secondly, UV photolysis of icy grain mantles may be important for the modification of gas-phase species, since molecules are cycled through both solid and gaseous phases as a result of accretion and desorption mechanisms (Blake et al. 1987; Brown & Charnley 1990; Millar et al. 1991; Charnley, Tielens, & Millar 1992; Shalabiea & Greenberg 1994).

A number of other astrochemical phenomena may rely on UV irradiation in the interstellar medium. For instance, the solid organic materials observed in both the diffuse ISM and in cometary dust (Kissel & Krueger 1987; Sandford et al. 1991; Pendleton, Tielens, & Werner 1990) may originate in the energetic processing of ice mantles in dense clouds (Greenberg 1973). This connection has been supported by laboratory simulations which show the formation of complex organic species from initially simple ices by such processes (Agarwal et al. 1985; Briggs et al. 1992; Strazzulla & Baratta 1992).

Previous studies of the UV properties of interstellar ice analogs have dealt mainly with mixtures of two or more ices and their combined chemistries (e.g., Hagen, Allamandola, & Greenberg 1979; Grim et al. 1989). This Chapter presents the results of UV photolysis experiments on pure ices of nine molecules known or suspected to be important components of interstellar ices: H_2O, NH_3, CH_4, O_2, N_2, CO, CO_2, CH_3OH, and H_2CO. Understanding these simple systems is essential before confronting the photochemistry of more complex ices. Moreover, detailed analyses of interstellar ice features have shown that ice mantles are not strictly homogeneous, and certain components exist in relatively pure states (Sandford et al. 1988; Tielens et al. 1991; Skinner et al. 1992; Schutte et al. 1996a; Boogert et al. 1997).

4.2 Experiment

4.2.1 Vacuum Set-up and Equipment

Detailed descriptions of the vacuum system and the procedures for the deposition and analysis of ice analogs have been given in Ch. 2. Molecules to be studied were condensed out of the gas phase onto a cold (10 K) IR-transparent substrate that is positioned inside the sample chamber of an FTIR spectrometer and may be rotated without breaking the vacuum. Rotation of the substrate permits deposition, UV irradiation, and IR spectroscopy to be performed with one ice sample. The temperature of the substrate is continuously adjustable between 10 K and room temperature using the resistive heater element.

A microwave-discharge hydrogen flow lamp (Opthos instruments) was used to irradiate the ice samples. The lamp flux at the substrate is $\sim 10^{15}\,\mathrm{cm^{-2}\ s^{-1}}$ ($E_{h\nu} > 6\,\mathrm{eV}$; Hagen 1982; Weber & Greenberg 1985) and its spectrum is dominated by five bands centered at 122 (Lyman-α), 136, 145, 160, and 280 nm. See Figure 4.1 for the lamp spectrum (de Groot, private communication). The lamp is mounted directly onto the sample chamber, and its UV flux is transmitted through a window of MgF_2, which is transparent at $\lambda \gtrsim 110$ nm.

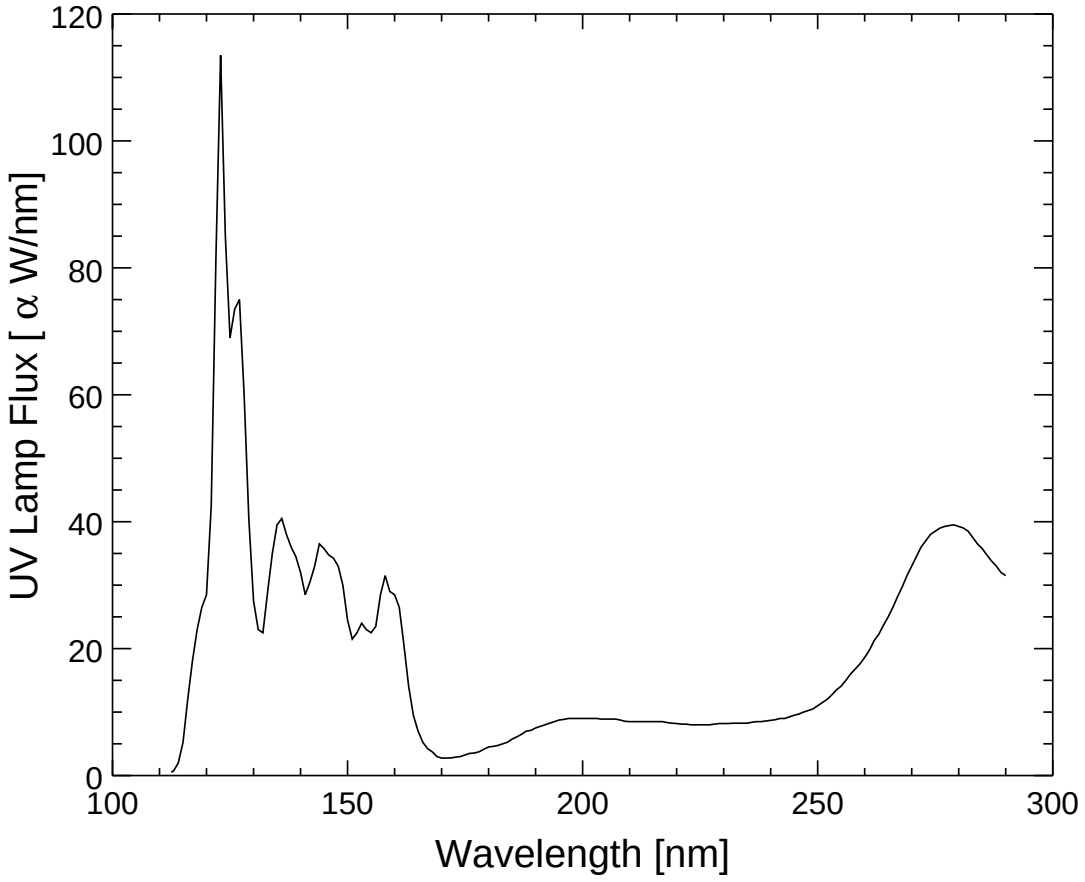

Figure 4.1: Spectrum of the microwave discharge lamp used in these experiments to irradiate interstellar ice analogs. Absolute y-scale is uncertain.

4.2.2 Ice samples

Deposited samples were typically 0.1 μm in thickness. This value was estimated using the column density derived from the IR absorption strengths after deposition (from e.g., Ch. 3) and a literature value of the ice's mass density. Thicknesses of $\lesssim 0.1\,\mu$m ensure that ice samples are optically thin throughout the wavelength range of the processing ultraviolet radiation (110 to 300 nm; Okabe 1978). Ices were deposited with flow rates between ~ 2 to 5×10^{15} cm^{-2} s^{-1} (1 to 2 μm s^{-1}) for 2.5 to 5 min.

As mentioned in § 2.2, the metal walls of our system constantly produce residual gases that are impossible to remove entirely. The contamination level of the samples was measured to be ~ 0.1–0.2 %. At the deposition rate of the residual gases,

the sample ice would become optically thick to UV radiation after 28 hr of constant deposition (estimated with an average UV cross section for H_2O of $2\times 10^{-18}\,cm^2$; Okabe 1978). For the timescales involved in these experiments ($\sim 2\,hr$), no significant loss of UV photons is expected due to the layer of background condensation.

In order to isolate the sample from background molecules condensing before and after deposition, the sample was deposited between two layers of solid argon (Ar). This procedure was made possible by the two independent deposition systems of our setup (§ 2.2), with which the transition from sample to Ar depositions was made almost instantaneously. Some small overlap did occur, however, and was seen as features of isolated H_2O and NH_3 in the deposition spectra of these molecules.

Rare-gas matrices such as Ar are transparent to the UV used to process the ices samples, since the relevant energy range lies well outside their continuum or discrete electronic transition regions (e.g., Klein & Venables 1976). Each Ar layer was approximately 3 to 5 times the thickness of the sample ice (~ 0.3–$0.5\,\mu m$). Deposition of each of the Ar layers was typically made at a rate of $\sim 2.4\times 10^{15}\,cm^{-2}\ s^{-1}$ ($\sim 3.5\,\mu m\ s^{-1}$) for 10 min.

As a consequence of using two relatively thick layers of Ar on either side of the sample ice, a sinusoidal wavelength dependence is observed in the baseline of obtained spectra (see, for example, Fig. 4.15). This is due to interference by directly transmitted photons and those which are scattered between the substrate and the vacuum interface of the sample. In addition to the sinusoidal structure, features appear in all experiments at ~ 3280, 1660, and $770\,cm^{-1}$ (3, 6, and $13\,\mu m$)[7] due to the continuous background condensation of H_2O.

To enable correction for the effects of the background contamination within the sample itself, two experiments were performed for each molecule to be studied, using flow rates that differed by about a factor of two. Thus, products due to contaminating molecules change by approximately the same factor between the two experiments: thereby achieving a means of distinguishing these products from those due to the sample molecules. This correction was performed, for example, in the experiments of solid CO photolysis where reactions of CO with contaminating H_2O

[7] In this Chapter, positions of IR features will be given in both cm^{-1} and μm, as in Ch. 3: e.g., "the $3280\,cm^{-1}$ ($3\,\mu m$) feature of H_2O."

molecules produced small amounts of HCO ($\sim 0.1\,\%$ at maximum).

A blank experiment was also performed in which a single layer of solid Ar was irradiated for 1 hr at 10 K. This experiment showed that some CO and CO_2 is produced in all cases due to the interaction of H_2O ice from background accretion and a thin layer of organic material covering the CsI substrate. Using the features present in this experiment (due solely to background gases), many small features were ruled out as possible products of sample molecules.

When producing ice samples of IR-inactive molecules such as Ar, N_2, and O_2, it is impossible to spectroscopically derive the quantity of gas deposited. To obtain this, depositions were made of these ices mixed with a trace of CO. Since the strength of the CO 2138 cm^{-1} (4.677 μm) feature in various ices is well known (e.g., Ch. 3), the deposited CO abundance can be determined and used together with the mixing ratio to estimate the quantity of IR-inactive molecules. This result was then used to calibrate the pressure increase (ΔP) needed at room temperature to set the deposition flow (see Ch. 3, Eq. 3.1). Inaccuracies in the mixing ratio and in the reproducibility of the flow at a given ΔP setting produce an error in the estimation of the deposited quantity of IR-inactive molecules of about a factor of two.

4.2.3 Irradiation procedure

Ices held at 10 K were irradiated stepwise for one hour, pausing to take a spectrum at each step. The total irradiation times at each step were 5 s, 15 s, 1 min, 3 min, 10 min, and 1 hr, corresponding to UV doses of $R \approx 0.01$, 0.03, 0.12, 0.36, 1.2, and 7.2, respectively. These levels of irradiation span the range of exposures expected for ice mantles in the dense ISM (§ 4.1). After irradiation, samples were heated at $\sim 2\,K\,min^{-1}$ to T $\sim$ 30, 60, 115, 150, and 270 K, and spectra taken at each step: thus sampling the expected temperature range for interstellar ices.

Reproducibility of the lamp's UV flux was checked by comparisons of several experiments involving the same molecule. As an illustration, in the two 1-hr irradiations of solid H_2CO at 10 K, the total amount of H_2CO destroyed differed by only 1 %.

It must also be noted that the photochemical reactions observed here are

strongly dependent on the wavelengths of the irradiating photons. While the UV lamp used has most of its flux in the appropriate energy range for interstellar conditions (Fig. 4.1), it may not reproduce the *actual* spectrum of the UV radiation present in the ISM. Any sharp peaks in the interstellar UV energy curve would strongly alter the observed reaction scheme and resulting end products.

4.3 Results

IR features appearing as a result of photolysis are listed by experiment in Tables 4.1, 4.2, 4.4, 4.4, 4.6, 4.7, and 4.9. These features are identified with molecular absorptions from the literature on the basis of three criteria. Since in most cases, literature data refer to measurements of ices isolated in different matrices (e.g., Ar or N_2), the first criterion is that the observed frequency should fall within 0.5 % of the listed position. Matrix shifts of this magnitude are often observed for IR features (e.g., Sandford et al. 1988; Sandford & Allamandola 1990; Schutte et al. 1996a; Ehrenfreund et al. 1996). Secondly, all strong features predicted to fall in relatively unobscured spectral regions must be visible. Finally, the warm-up behavior should be consistent with the proposed assignment, and highly volatile or reactive species should disappear at relatively low temperatures. When any of the above criteria are not obviously met, such features are not explicitly assigned to a carrier and entered in the listings as "unidentified."

Species are designated as first- or higher-order products of the photolysis based on the initial growth rates of their IR features. Linear growth with time indicates a first-order product, and steeper growth represents higher order. Photoproduction yields after 1 hr of UV exposure are given in Tables 4.3, 4.5, 4.8, and 4.10 for species whose absolute IR absorption strengths are known.

For each experiment, growth as a function of time is shown for a number of IR features selected to give an overview of the production of new species (Figs. 4.3, 4.4, 4.5, 4.7, 4.9, 4.12, 4.14, and 4.16). These curves may be converted to abundance at any time using the absorption strengths listed in the 1 hr yield tables (Tables 4.3, 4.5, 4.8, and 4.10).

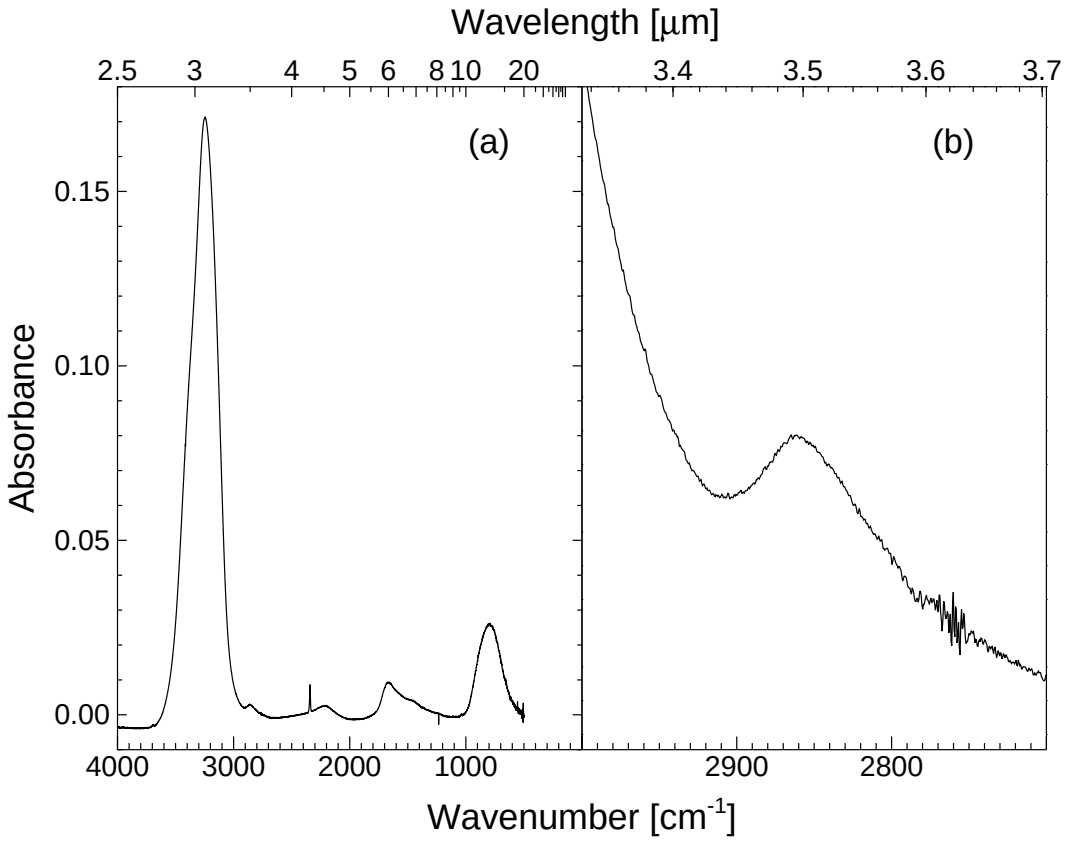

Figure 4.2: Spectrum of H_2O ice after 1 hr UV irradiation and then warm-up to T = 70 K: (a) full spectrum; (b) enlargement ($\times$20) of the 2850 cm^{-1} (3.51 μm) feature of H_2O_2.

4.3.1 H_2O

The spectrum of H_2O ice after 1 hr of photolysis is displayed in Fig. 4.2. Frequencies and identifications of the new IR absorptions are given in Table 4.1, and the evolution of the features of H_2O and of its photoproducts is shown in Fig. 4.3. OH, H_2O_2, and HO_2 have been identified as the main photolysis products of H_2O. The feature due to molecular hydrogen at 4143 cm^{-1} (2.41 μm; Sandford & Allamandola 1993) was not clearly identified.

Properties of the features which appear at 3428 and 3453 cm^{-1} (2.917 and 2.896 μm) suggest that they are due to the OH radical. Both disappear between 30 and 70 K, indicating that they are due to a highly reactive species. They also grow simultaneously and display similar warm-up behaviors. These two features coincide

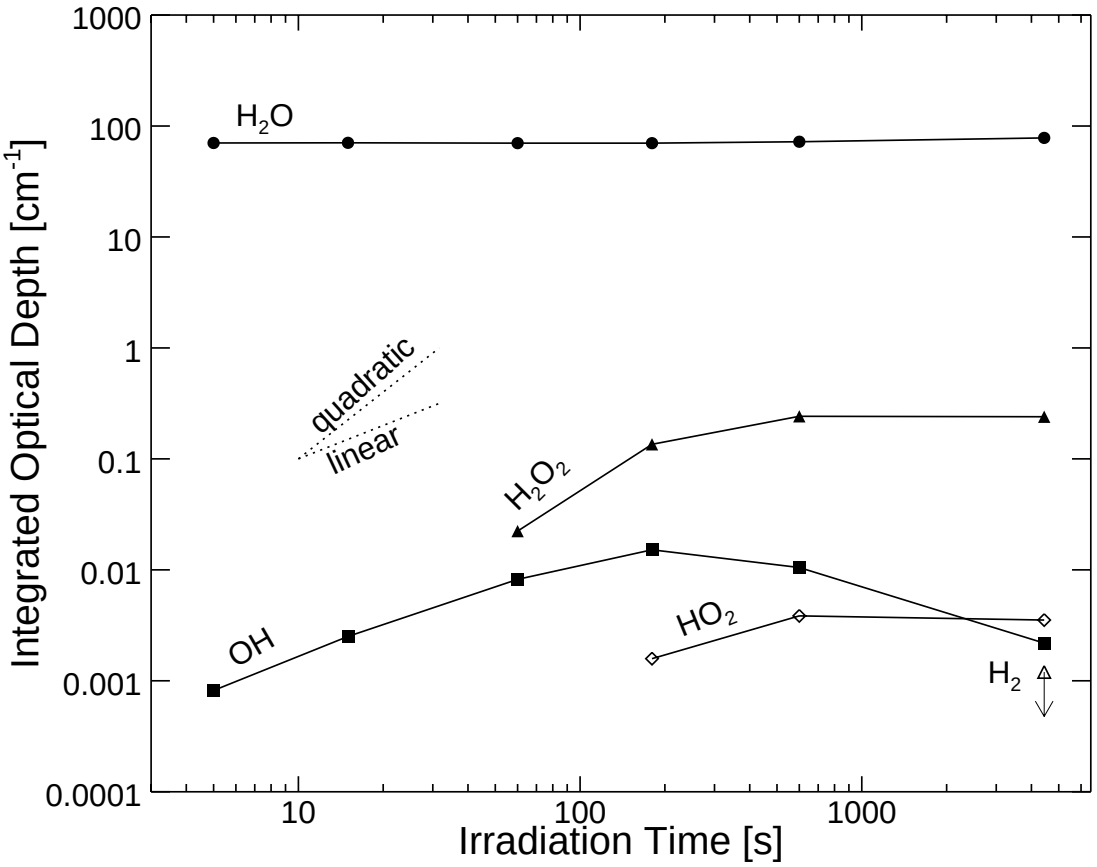

Figure 4.3: Evolution of features in irradiation of H_2O, represented by its 3280 cm^{-1} (3 μm) feature. All others are indicated in Table 4.1. The dotted lines indicate linear and quadratic time dependencies.

with the doublet structure seen in Ar by Acquista, Schoen, & Lide (1968) during the UV photolysis of Ar:H_2O = 250:1 mixtures. This pattern most likely indicates that the OH radicals reside in two distinctly different matrix sites: isolated OH, and OH:H_2O complexes. If a fraction of the sample and Ar depositions in our experiments overlap or the layers penetrate each other to some extent (§ 4.2.2), some H_2O molecules and their photoproducts may be isolated within the Ar layer to produce such a doublet effect. The growth of 3453 cm^{-1} (2.90 μm) feature is plotted in Fig. 4.3 and shows a first-order time dependence, appearing after 5 s of UV exposure.

The features observed at 2850 and 1457 cm^{-1} (3.509 and 6.863 μm) are assigned

Table 4.1: Features observed during the photolysis of solid H_2O and NH_3 at T = 10 K. Product order is listed for features whose evolution is displayed in Figs. 4.3 and 4.4.

Ice	Position cm^{-1} (μm)	Assign.	Order	Ref
H_2O	1101 (9.083)	HO_2		1
	1389 (7.199)[a]	HO_2	?	1
	1457 (6.863)	H_2O_2		2
	2850 (3.509)[a]	H_2O_2	2+	2
	3413 (2.930)	HO_2		1
	3428 (2.917)	OH		3
	3453 (2.896)[a]	OH	1	3
	4143 (2.414)[a]	H_2		4
NH_3 [b]	886 (11.3)	N_2H_4	?	5
	1505 (6.645)	NH_2	1	6
	2115 (4.728)	Unid.	1	
	4137 (2.417)	H_2		4

[a] Growth curve plotted in Fig. 4.3.

[b] Growth curves plotted in Fig. 4.4 for all listed features of NH_3 experiment.

REFERENCES.— (1) Jacox & Milligan 1972; (2) Giguère & Harvey 1959; (3) Acquista, Schoen, & Lide 1968; (4) Sandford & Allamandola 1993; (5) Roux & Wood 1983; (6) Milligan & Jacox 1965.

to H_2O_2. After warm-up to 70 K, they have shifted to 2853 and 1450 cm^{-1} (3.505 and 6.900 μm), respectively. Giguère & Harvey (1959) have shown that absorptions due to H_2O_2 fall at 2840 and 1455 cm^{-1} (3.521 and 6.873 μm) in an 80 K crystalline H_2O_2:H_2O $\sim$ 0.2:1 mixture. These positions coincide by 0.5 and 0.3 % to the locations of the features observed in these experiments. The 2850 cm^{-1} (3.509 μm) feature displays a second-order time dependence in Fig. 4.3 and is clearly seen after 1 min of photolysis.

The features falling at 1101, 1389, and 3413 cm^{-1} (9.083, 7.199, and 2.930 μm) are identified with the HO_2 ν_3, ν_2, and ν_1 fundamentals, respectively (Jacox & Milligan 1972). All disappear between 30 and 70 K. The growth of the 1389 cm^{-1} (7.199 μm) feature is plotted in Fig. 4.3. Its low strength at early stages of photolysis makes a time-dependence assignment unclear.

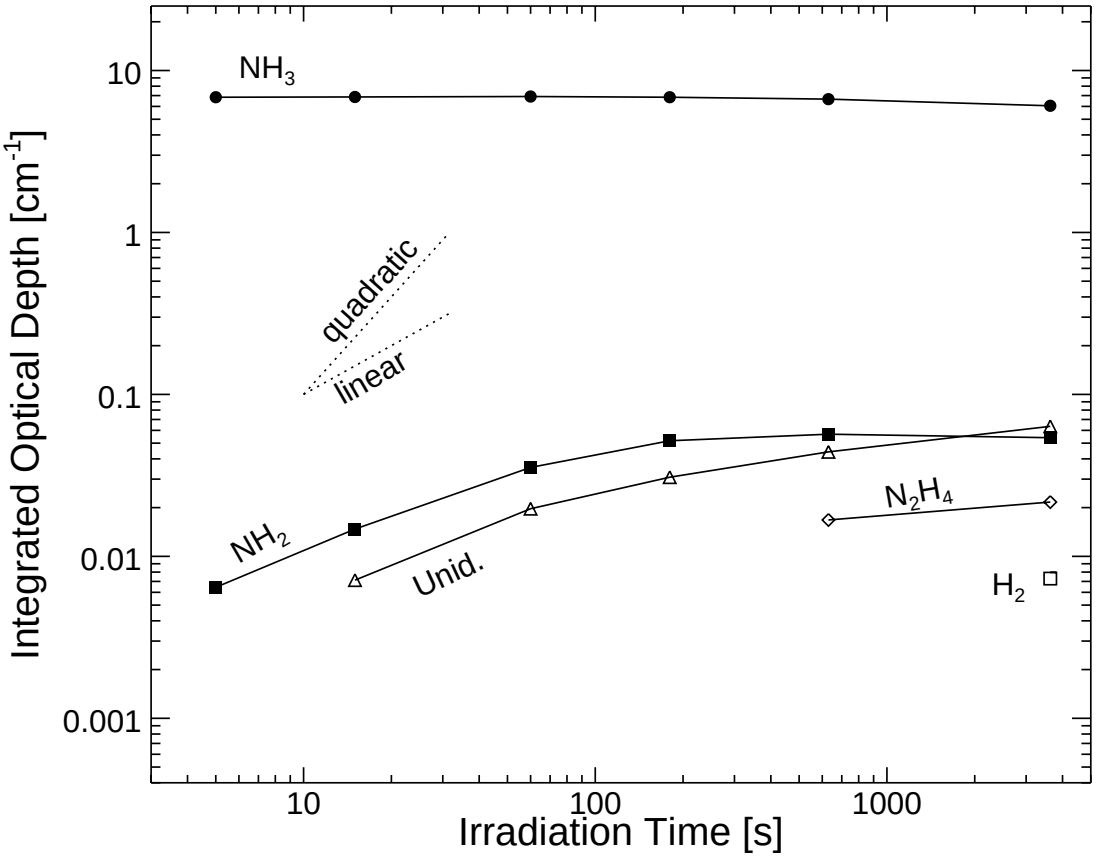

Figure 4.4: Evolution of features in irradiation of NH_3, represented by its 1070 cm^{-1} (9.346 μm) feature. All others are indicated in Table 4.1. The dotted lines indicate linear and quadratic time dependencies.

4.3.2 NH_3

New features appearing during the photolysis of solid NH_3 at 10 K are listed with identifications in Table 4.1. The evolution curves of selected features during photolysis are displayed in Fig. 4.4. The most obvious products of the photolysis are N_2H_4 and NH_2, detected by the growth of features at 886 and 1505 cm^{-1} (11.29 and 6.645 μm), respectively. The identification of N_2H_4 is relatively insecure, given that only one feature was detectable. A broad, strong feature at 2115 cm^{-1} (4.728 μm) with a width of 90 cm^{-1}, which appears after only 15 s of UV photolysis, remains unidentified. This feature disappears after warm-up to 60 K, indicating a its carrier may be a reactive species. There was no clear indication of diimide (N_2H_2)

in our spectra at 1286, 1058, or 946 cm^{-1} (7.776, 9.452, or 10.57 μm; Rosengren & Pimentel 1965). Imidogen (NH) is also not seen at 3125 cm^{-1} (3.200 μm; Rosengren & Pimentel 1965), possibly due to the strong NH_3 absorptions in this region.

4.3.3 CH_4

Numerous IR features appear upon photolysis of CH_4, suggesting a complex photochemistry (Table 4.2). After only 5 s of irradiation, sharp features which may be ascribed to ethane (C_2H_6) occur at 822, 1375, 1465, 2882, 2908, 2942, and 2975 cm^{-1} (12.17, 7.273, 6.826, 3.470, 3.439, 3.399, and 3.361 μm; Comeford & Gould 1960). Broader features grew in the aliphatic C–H stretching region (3000–2800 cm^{-1}; 3.3–3.6 μm) and bending region (1600–1200 cm^{-1}; 6.2–8.3 μm) at large UV doses, indicating the formation of larger aliphatic structures. In particular, the the growth of a feature at 750 cm^{-1} (13.33 μm) signified the formation of propane (C_3H_8; Comeford & Gould 1960).

Besides aliphatic features, relatively weaker absorptions appeared that may be assigned to unsaturated species such as allene, ethylene, and carbon chains containing double and triple carbon bonds. However, no evidence was found for the presence of the smallest unsaturated species, acetylene (C_2H_2).

A feature at 608 cm^{-1} (16.4 μm) which disappeared at $T \lesssim 30$ K suggested the presence of the CH_3 radical. There was no indication of the CH_2 radical, despite the fact that this species is a known product of the vacuum UV photolysis of gaseous CH_4, much more so than CH_3 (Okabe 1978). Perhaps CH_2 is efficiently converted to ethane by reacting with CH_4 in our experiments (e.g., $CH_2 + CH_4 \rightarrow C_2H_6$).

No strong evidence for cyclic structures was found in the irradiated CH_4 spectra. However, two unidentified features at 738 and 950 cm^{-1} (13.6 and 10.5 μm) coincided with features generally produced by cyclic hydrocarbons with side chains (e.g., *n*-propylcyclohexane), substituted benzenes (e.g., toluene and xylene) and aromatics linked to chains, such as styrene (Pouchert 1981).

Figure 4.5 shows the integrated optical depths for selected IR features of the species detected. Absorbance values for the C–H stretching region (3000–2800 cm^{-1}; 3.3–3.6 μm) have been integrated over the entire frequency range with the exclusion

Table 4.2: Features observed during the photolysis of solid CH_4 at T = 10 K. The full width at half-maximum (FWHM; in cm^{-1}) is indicated for overlapping features.

Position cm^{-1} (μm)	FWHM [cm^{-1}]	Assignment	Comments	Refs
608 (16.4)[a]		CH_3		1,2
738 (13.6)		unid.		
750 (13.3)[a]		propane (C_3H_8)		3
822 (12.2)[b]		ethane (C_2H_6)		3
911 (11.0)[a]		$R_2C{=}CH_2$	δCH (out-of-plane)	4
950 (10.5)		unid.		
1235 (8.097)		unid.		
1375 (7.273)		R–CH_3	δ_sCH	
1375 (7.273)		ethane		3
1438 (6.954)	6	ethylene (C_2H_4)		3
1438 (6.954)	26	$R_2C{=}CH_2$	δCH in-plane	
1460 (6.849)		R–CH_3	δ_{as}CH	
1465 (6.826)	7	ethane		3
1470 (6.803)		R–CH_2–R	CH_2 scissor	
1645 (6.079)		$R_2C{=}CHR$	ν(C=C)	
1960 (5.102)		allene ($H_2C{=}C{=}CH_2$)		5
2850 (3.509)	8	R–CH_2–R	ν_s(C–H)	
2875 (3.478)	15	R–CH_3	ν_s(C–H)	
2882 (3.470)	6	ethane		3
2908 (3.439)	5	ethane		3
2916 (3.429)	7	propane		3
2933 (3.409)	16	R–CH_2–R	ν_{as}(C–H)	
2942 (3.399)	11	ethane		3
2962 (3.376)	26	R–CH_3	ν_{as}(C–H)	3
2975 (3.361)[c]	11	ethane		3
3095 (3.231)[a]		ethylene		3,6,7
3248 (3.079)		H–C$\equiv$C–R	ν(C–H)	8
3270 (3.058)		H–C$\equiv$C–R	ν(C–H)	8
3315 (3.017)[a]		H–C$\equiv$C–R	ν(C–H)	4,9

[a] Growth curve plotted in Fig. 4.5.

[b] Used for ethane growth curve in later time steps.

[c] Used for ethane growth curve in early time steps.

REFERENCES.— (1) Pacansky & Bargon 1975; (2) Pacansky, Koch, & Miller 1981; (3) Comeford & Gould 1960; (4) Pouchert 1981; (5) Seloudoux, Soussen-Jacob, & Vincent-Geisse 1979; (6) Duncan, McKean, & Mallinson 1973; (7) Brecher & Halford 1961; (8) Saussey, Lamotte, & Lavalley 1976; (9) Maki & Toth 1965.

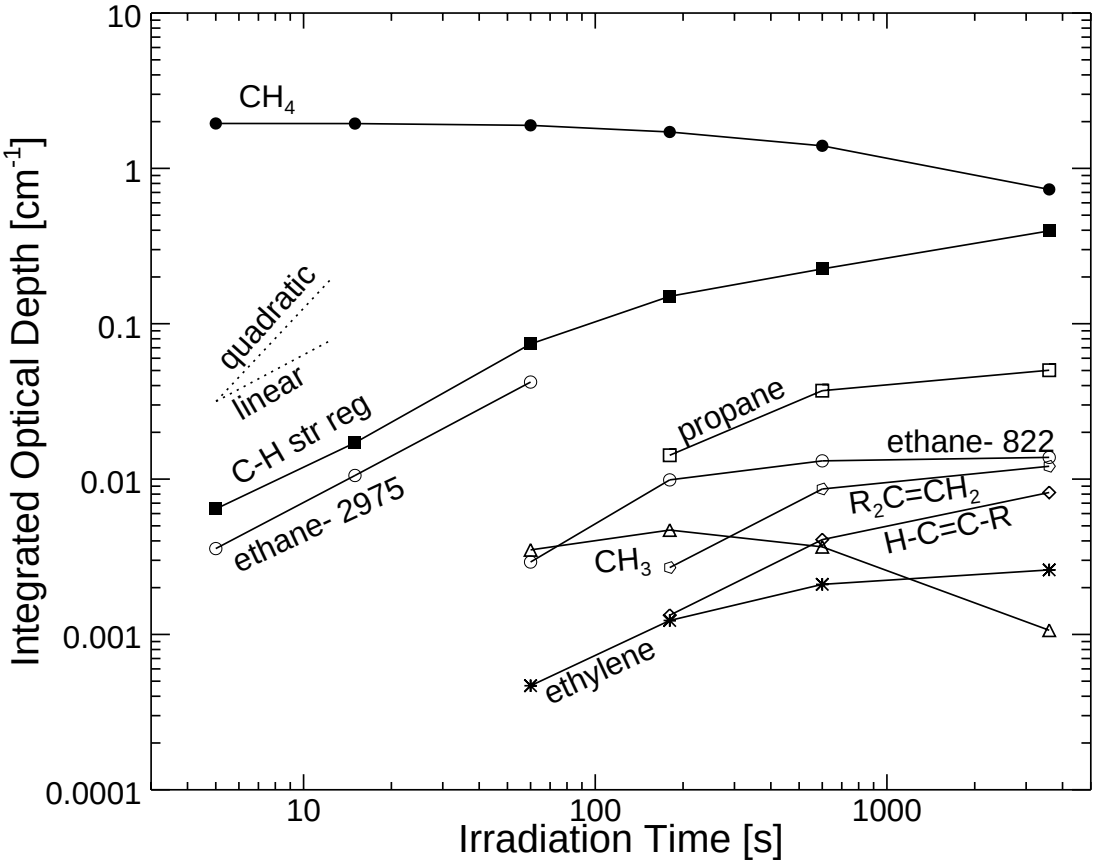

Figure 4.5: Evolution of features in irradiation of CH_4, represented by its $3009\,cm^{-1}$ ($3.3\,\mu m$) feature. The $2975\,cm^{-1}$ ($3.36\,\mu m$) feature of ethane has been plotted in early time steps, when there is little overlap with broader structures. In later time steps, the weaker $822\,cm^{-1}$ ($12.2\,\mu m$) feature of ethane has been plotted. All others are indicated in Table 4.2. The dotted lines indicate linear and quadratic time dependencies.

of the $3009\,cm^{-1}$ ($3.3\,\mu m$) CH_4 feature. The area indicated in Fig. 4.5 is therefore indicative of higher aliphatics (ethane and larger). Even after the growths of ethane and propane had leveled off, the integrated absorption of the C–H stretching region continued to increase due to the production of even larger aliphatics, reflecting an increasing molecular complexity with UV dose.

In Table 4.3, the derived abundances for species produced after 1 hr of UV photolysis are given. Spectroscopically, it is difficult to derive separate abundances for hydrocarbons with overlapping C–H stretching modes. However, separate abun-

Table 4.3: Abundances of products in CH_4 ice after 1 hr UV irradiation at T = 10 K.

Molecule	Position cm^{-1} (μm)	A[a]	Ref	Abund.[b]
CH_4	3009 (3.323)	6.4	1	38
C_2H_6	3100–2800 (3.2–3.6)	6.5	2	8.0
higher-order volatiles[c]	3100–2800 (3.2–3.6)	6.5	2	9.0
higher-order residue[d]	3100–2800 (3.2–3.6)	6.5	2	14
C_2H_4	1438 (6.954)	0.85	3	2.6
CH_3	608 (16.4)	25	4	0.01
$H_2C{=}C{=}CH_2$	1960 (5.102)	2.6	5	0.6

[a] IR absorption strength, in units of 10^{-18} cm/C atom.
[b] % relative to inital CH_4 abundance.
[c] Between $\sim$ 2 and 7 C atoms.
[d] At room temperature, number of C atoms $\geq$ 7.
REFERENCES.— (1) d'Hendecourt & Allamandola 1986; (2) Wexler 1967; (3) Fan & Ziegler 1992; (4) Wormhoudt & McCurdy 1989; (5) Youngquist, Crawford, & Overend 1979.

dances for species of different volatilities may be estimated from the spectra obtained after warm-up to 115 and 290 K, since many molecules evaporate between the ranges of T = 10–115 K and 115–290 K. The sizes of the evaporating species may be roughly estimated by comparing the observed sublimation temperatures with those of molecules for which this value has been previously established under vacuum conditions. For example, we may compare the known values for H_2CO (which sublimes at T $\sim$ 115 K; Schutte, Allamandola, & Sandford 1993) and the most volatile component of the room temperature organic residue obtained by the irradiation of ices under vacuum, hydroxyacetamide ($HOCH_2CONH_2$; Agarwal et al. 1985; Briggs et al. 1992).

The boiling point of a component should be a reasonable indicator of its sublimation behavior under vacuum. Comparing the boiling points of formaldehyde and hydroxyacetamide (252 and 393 K, respectively) with that of alkanes, it is estimated that ethane and smaller species should sublime below 115 K. This is in good agreement with the behavior of the ethane and propane features observed in these experiments (Table 4.3). According to this criterion, all alkanes containing less than

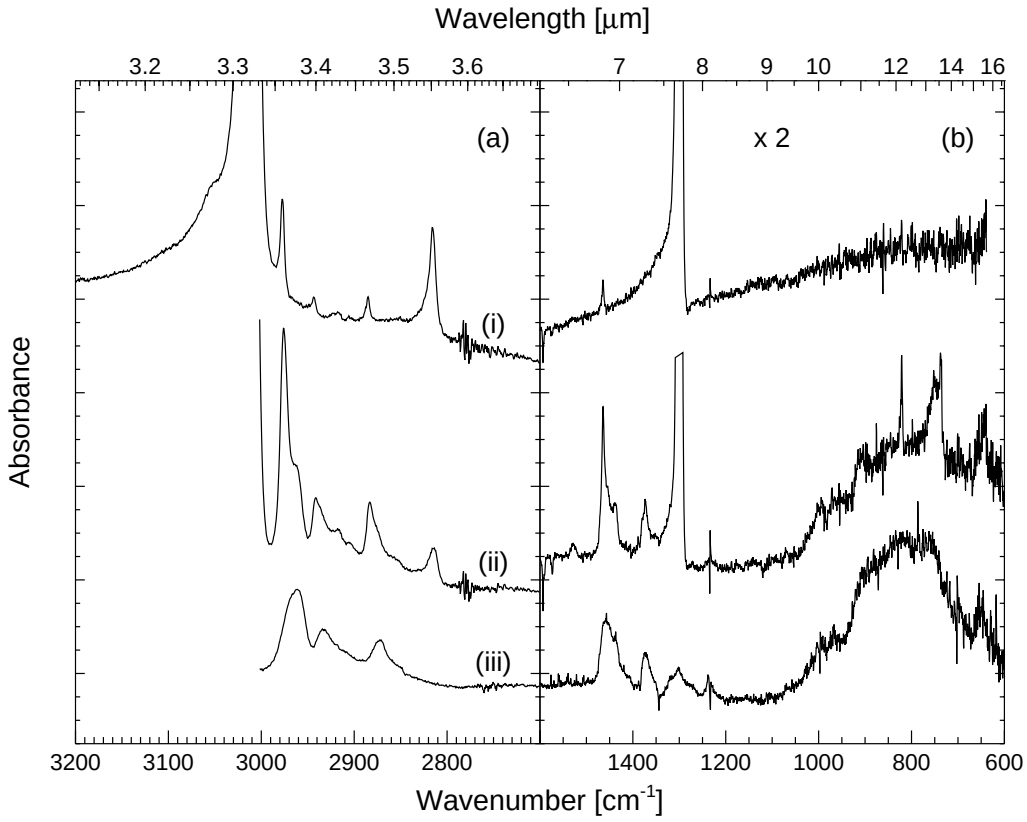

Figure 4.6: IR spectra of irradiated solid CH_4: (a) stretching mode region, 3200–2700 cm^{-1} (3.13–3.70 μm); (b) deformation region, 1600–600 cm^{-1} (6.25–16.7 μm). Y-scale in (b) is enlarged $\times 2$ with respect to (a). Spectra shown (i) after 1 min UV irradiation at 10 K, (ii) after 1 hr UV, and (iii) heated to 115 K. The 3009 and 1302 cm^{-1} (3.3 and 7.7 μm) features of CH_4 have been clipped in (ii) to accentuate smaller features.

~ 7 to 8 C atoms should evaporate in the temperature interval from 115 K to room temperature.

The final abundances listed in Table 4.3 indicate that only 72 % of the carbon atoms have been accounted for by the molecules identified. It should be pointed out that the mass density of amorphous solid CH_4 used to derive the strengths of its IR features is relatively uncertain and is generally assumed to be equal to the density of H_2O for these purposes (1.0 g cm^{-3}). Recent work suggests a much lower value, about 0.53 g cm^{-3} (Kaiser, private communication). The abundance of solid CH_4 deposited in this experiments is therefore equally as uncertain, and this fact may

Table 4.4: Features observed during the photolysis of solid CO and CO_2 at T = 10 K.

Ice	Position cm^{-1} (μm)	Assign.	Order	Ref
CO	660 (15.2)	CO_2		1
	1989 (5.028)	C_2O		2
	2028 (4.931)[a]	C_3	?	3
	2243 (4.458)[a]	C_3O	2+	3
	2248 (4.448)	C_3O_2		4
	2281 (4.384)	$^{13}CO_2$		1
	2347 (4.261)[a]	CO_2	1	1
	2400 (4.167)	C_3O_2		4
	3413 (2.930)	Unid.		
	3550 (2.817)	Unid.		
	3602 (2.776)	CO_2		1
	3709 (2.696)	CO_2		1
CO_2	706 (14.2)	O_3		5
	976 (10.2)	CO_3		6
	1043 (9.588)[b]	O_3	2+	5
	1053 (9.497)	Unid.		
	1067 (9.372)	CO_3		6
	1883 (5.311)	CO_3		6
	2044 (4.892)[b]	CO_3	1	6
	2093 (4.778)	^{13}CO		1
	2141 (4.671)[b]	CO	1	1
	2243 (4.458)[b]	C_3O	2+	3

[a] Used for growth curve in Fig. 4.7.

[b] Used for growth curve in Fig. 4.9.

REFERENCES.— (1) Hudgins et al. 1993; (2) Jacox et al. 1965; (3) DeKock & Weltner 1971; (4) Smith & Leroi 1966. (5) Brewer & Wang 1972; (6) Moll, Ckitter, & Thompson 1966.

help to explain the apparent lack of carbon conservation observed here (Table 4.3).

It is interesting to note that the ratio of CH_3:CH_2 groups, (as indicated by the relative intensities of their asymmetric C–H stretching modes), is as large as ~ 2 at 115 K and ~ 1 at room temperature. For the unevaporated linear alkane groups at these temperatures of the expected size range (≥ 3 and ≥ 7 C atoms, respectively) this ratio should be much smaller. The large alkanes produced in these experiments may therefore contain highly branched structures.

Ausloos, Rebbert, & Lias (1965) reported the results of the UV photolysis

of an Ar:CH_4 = 40:1 mixture. Although they indicated the production of species similar to those presented here, the relative abundances of large species (butanes, pentanes, etc.) were much smaller in their experiments. This could perhaps be due to their Ar dilution, which isolated the photoproducts and led to fewer secondary interactions.

4.3.4 CO

Features appearing during the photolysis of solid CO at 10 K are listed in Table 4.4. CO_2, C_2O, and C_3O were observed as the main photoproducts. The features of CO_2 appeared at 660, 2347, 3602, and 3709 cm^{-1} (15.2, 4.261, 2.776, and 2.696 μm; e.g., Hudgins et al. 1993).

After long irradiation times ($\sim$ 1 hr), the absorption associated with C_3O at 2243 cm^{-1} (4.458 μm) became a sharp doubly-peaked structure, the second peak falling at 2248 cm^{-1} (4.448 μm). The growth of this second peak corresponded with a weak feature centered near 2400 cm^{-1} (4.167 μm). These features were assigned to carbon suboxide (C_3O_2), in fair agreement with previously reported features of this species at 2400 and 2255 cm^{-1} (4.167 and 4.435 μm) by Smith & Leroi (1966). However, this assignment was only tentatively made, since other strong features of C_3O_2 were not seen near 1580 and 530 cm^{-1} (6.329 and 18.9 μm; Smith & Leroi 1966).

CO_2 is produced by reactions of CO with the background H_2O as well as the CO molecules alone. Since two experiments with different contamination levels were performed (see § 4.2), it was possible to derive and remove the excess CO_2 abundance from the measurements. The correction factor was found to be only 1–2 % of the measured CO_2 abundances in the two experiments. CO_2 may also formed by reactions of the background H_2O with organic material on the CsI substrate itself. This was removed from our measurements using results from the photolysis of a layer of pure Ar (§ 4.2.2).

During warm-up all observed species evaporated simultaneously with CO at T $\approx$ 30 K. No sign of any residue was found.

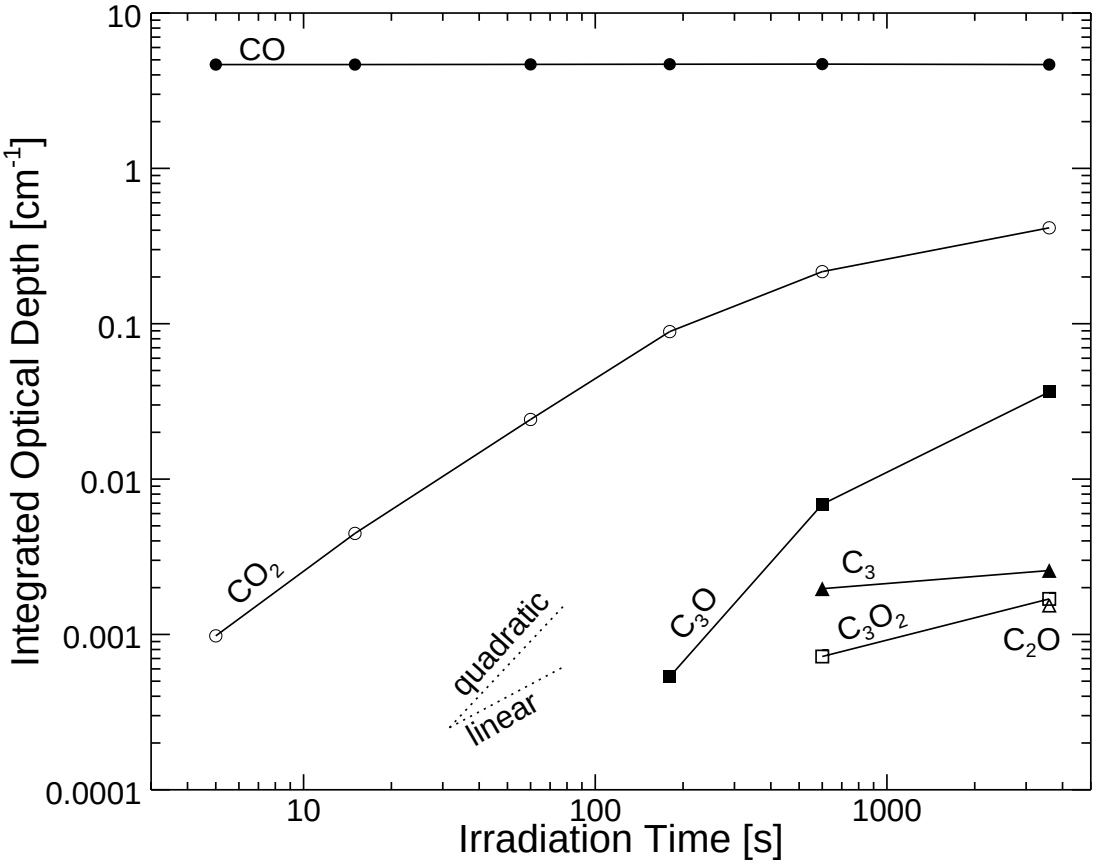

Figure 4.7: Evolution of features in irradiation of CO, represented by its stretching feature at 2138 cm^{-1} (4.677 μm). All others are indicated in Table 4.4. The dotted lines indicate linear and quadratic time dependencies.

4.3.5 CO_2

A list of features which appeared during the photolysis of solid CO_2 at 10 K is given in Table 4.4. The primary product was CO, whose 2138 cm^{-1} (4.677 μm) feature appears on extremely short timescales in our spectra. Two features also appeared at 706 and 1043 cm^{-1} (14.2 and 9.588 μm) and were assigned to O_3. Upon warm up to 30 K, the 1043 cm^{-1} (9.588 μm) feature increased in depth by 7 %, indicating that trapped O atoms diffused through the matrix to form more O_3 (cf., Grim & d'Hendecourt 1986). The CO_3 radical is highly unstable, and, according to Okabe (1978) who report the results of gas-phase CO_2 experiments, CO_3 was formed on the cooled window of their gas chamber rather than in the gas phase itself.

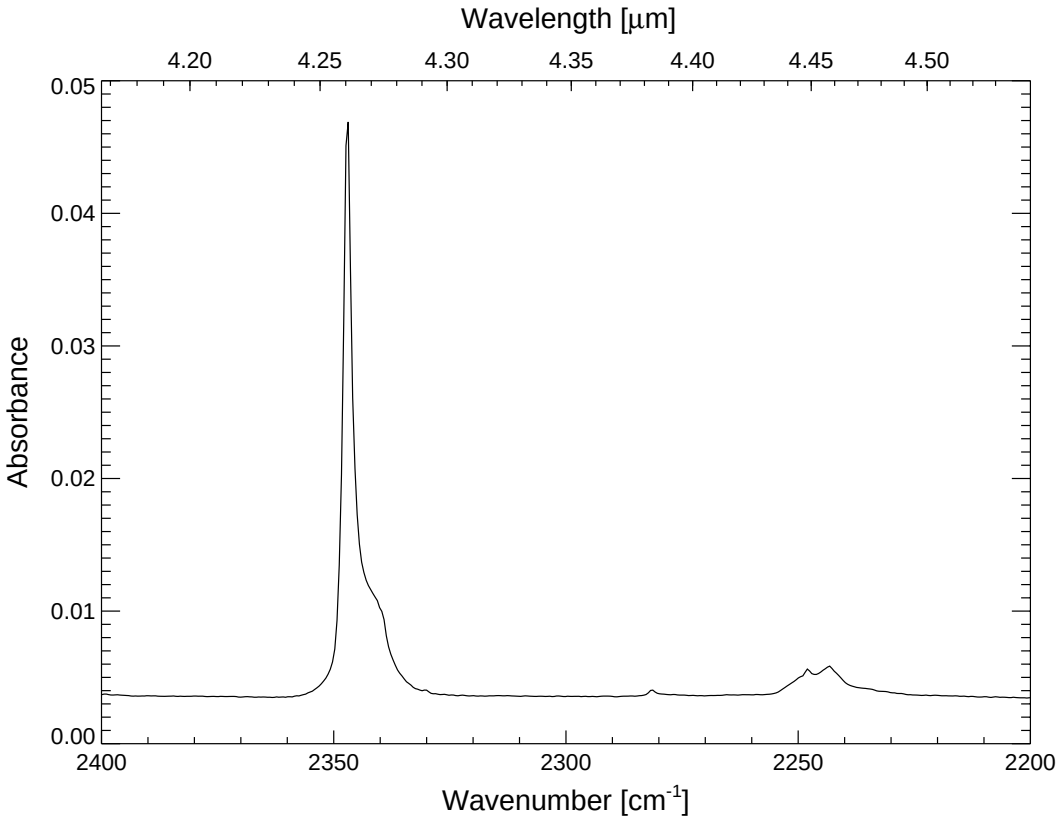

Figure 4.8: 2400–2200 $\mathrm{cm^{-1}}$ (4.2–4.5 μm) region in the spectrum of solid CO ice after 1 hr UV irradiation at T = 10 K. The C=O stretching features of $\mathrm{CO_2}$ and $\mathrm{^{13}CO_2}$ are present at 2347 and 2281 $\mathrm{cm^{-1}}$ (4.261 and 4.384 μm), and the doubly-peaked structure of the $\mathrm{C_3O}$ feature may be seen at 2243 and 2248 $\mathrm{cm^{-1}}$ (4.458 and 4.448 μm).

Estimated abundances of CO_2 photoproducts after 1 hr of UV irradiation are given in Table 4.5. Since the absorption strengths of CO_3 IR features are not known, the final abundance of CO_3 and the intrinsic strength of its 2044 $\mathrm{cm^{-1}}$ (4.982 μm) feature were calculated assuming that it contained all carbon not tied up in CO and CO_2. Under this assumption, 97 % of available O atoms were accounted for in the observed CO_2, CO, CO_3, and O_3 abundances (a certain quantity may have been bound in O_2 as well, but the extremely weak feature of O_2 was unobserved). All features due to the CO_2 photolysis disappeared at 115 K, with no residue.

Table 4.5: Abundances of products in CO and CO_2 ices after 1 hr UV at T = 10 K.

Ice	Product	Position cm^{-1} μm	A[a]	Ref	Abund.[b]
CO	CO	2138 (4.677)	1.1	1	100
	CO_2	2347 (4.261)	7.6	1	0.8
CO_2	CO_2	2342 (4.270)	7.6	1	59
	CO	2138 (4.677)	1.1	1	32
	CO_3	2044 (4.892)	0.54[c]		9[c]
	O_3	1043 (9.588)	1.4	2	5.9

[a] IR absorption strength, in units of 10^{-17} cm $molec^{-1}$.
[b] % relative to initial ice deposition.
[c] Estimated assuming CO_3 contains all remaining C atoms.
References.—(1) this work, Ch. 3; (2) Smith et al. 1985.

Table 4.6: Features observed during the photolysis of solid O_2 and N_2 at T = 10 K.

Ice	Position cm^{-1} (μm)	Assign.	Ref
N_2	2150 (4.651)[a]	N_3	1
O_2	705 (14.2)	O_3	2
	1040 (9.615)	O_3	2
	1105 (9.050)	O_3	2
	1550 (6.452)	O_2	3,4
	1720 (5.814)	O_3	2
	2046 (4.888)	O_3	2
	2110 (4.739)	O_3	2
	3030 (3.300)	O_3	2

[a] Tentative assignment, appears as a shoulder on contamination CO feature.
References.— (1) Milligan, Brown, & Pimentel 1959; (2) Brewer & Wang 1972; (3) Cairns & Pimentel 1965; (4) Ehrenfreund et al. 1992.

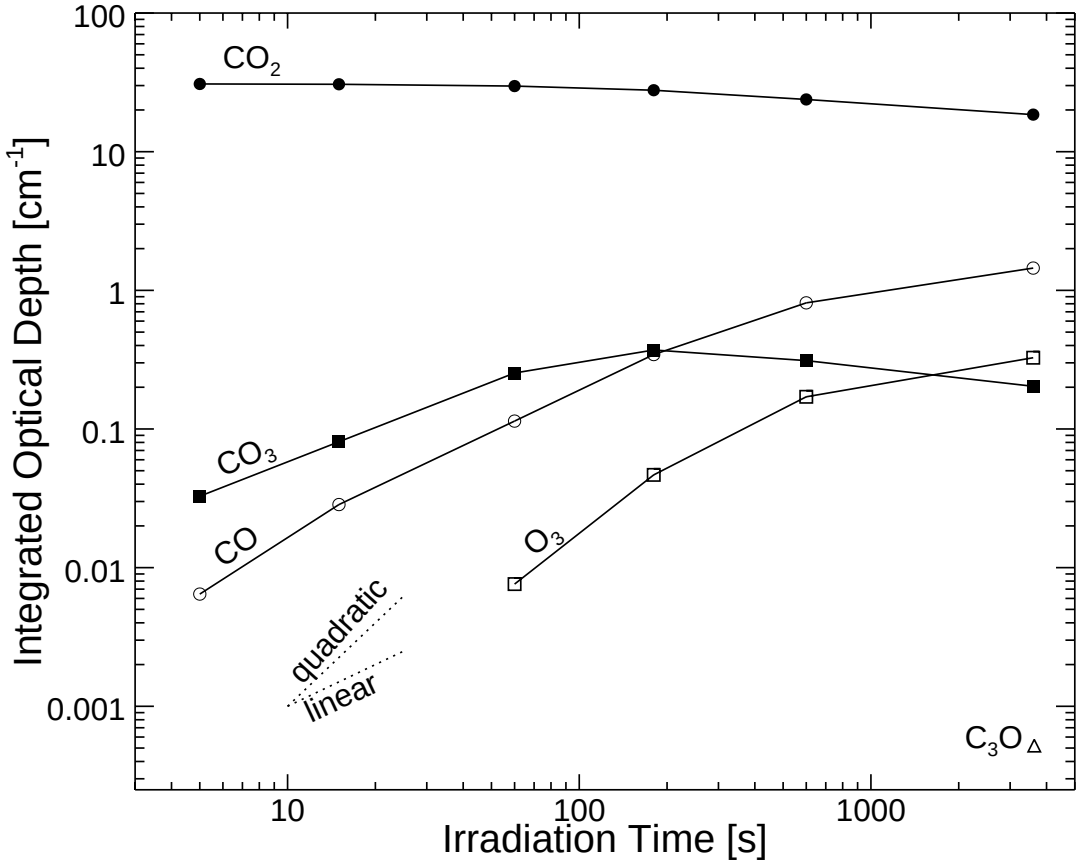

Figure 4.9: Evolution of features in irradiation of CO_2, represented by its feature at 2342 cm^{-1} (4.270 μm). All others are indicated in Table 4.4. The dotted lines indicate linear and quadratic time dependencies.

4.3.6 N_2

N_3, the only photolysis product expected for molecular nitrogen, has been reported to have an asymmetric stretching feature falling at 2150 cm^{-1} (4.651 μm; Milligan, Brown, & Pimentel 1959). This absorption was not clearly seen in these experiments since it (unfortunately) overlaps with the CO feature produced by reactions of the contaminating molecules (see § 4.2.2). A strong shoulder on the CO feature was seen, however, and fell at the correct location for the N_3 absorption. The major contributor to this shoulder was most likely the CO satellite feature also located at this position (Sandford et al. 1988), but upon warm-up of the ice matrix, the observed shoulder *increased* in strength relative to its neighboring CO contam-

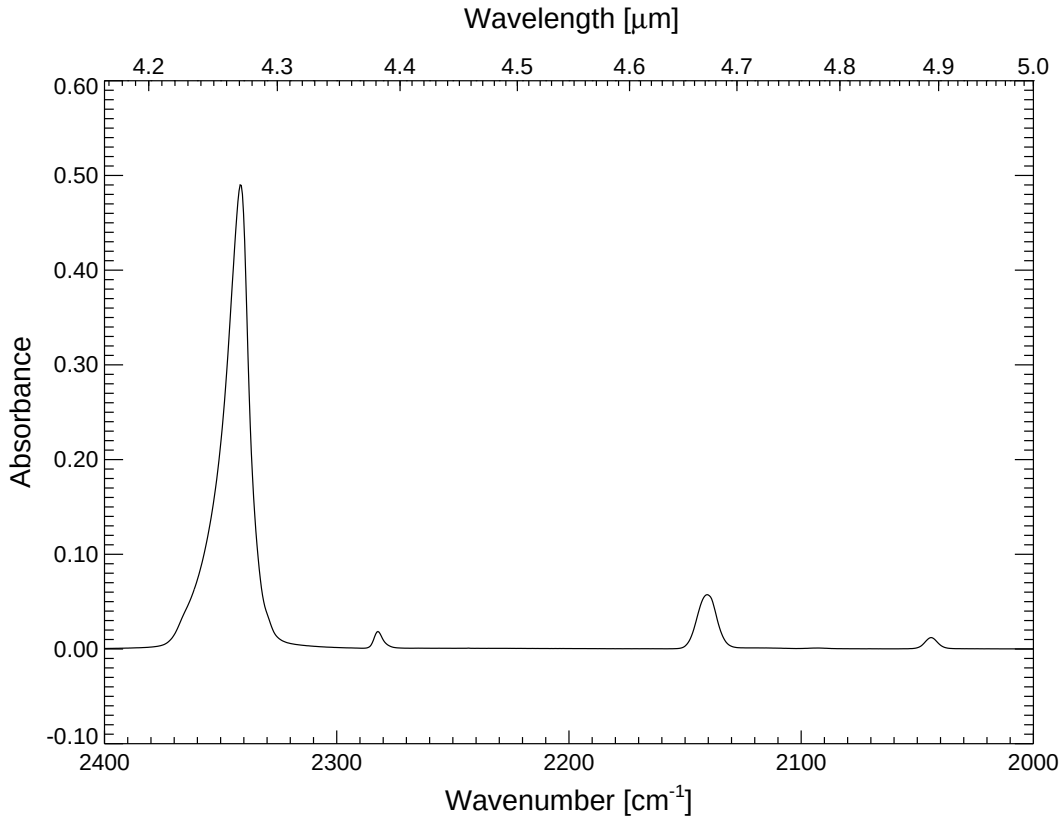

Figure 4.10: 2400–2000 $\mathrm{cm^{-1}}$ (4.2–5.0 μm) region in the spectrum of solid $\mathrm{CO_2}$ after 1 hr UV irradiation at T = 10 K. The features at 2342 and 2280 $\mathrm{cm^{-1}}$ (4.270 and 4.386 μm) are due to $\mathrm{CO_2}$ and $\mathrm{^{13}CO_2}$, respectively. Features due to CO and $\mathrm{CO_3}$ fall at 2138 and 2044 $\mathrm{cm^{-1}}$ (4.677 and 4.892 μm).

ination feature (in contrast with lab studies of pure CO; Sandford et al. 1988). A tentative assertion is made that part of this shoulder may be due to N_3, since it appeared at this strength only in the experiments of N_2. No other features due to products of N_2 photolysis were observed.

4.3.7 O_2

The UV irradiation of molecular oxygen led to the production of ozone (O_3) on very short timescales, and O_3 was observed as the sole photolysis product in these experiments (see Figs. 4.12 and 4.11 and Table 4.6).

The matrix-induced 1550 $\mathrm{cm^{-1}}$ (6.452 μm) feature of O_2 appeared in the spec-

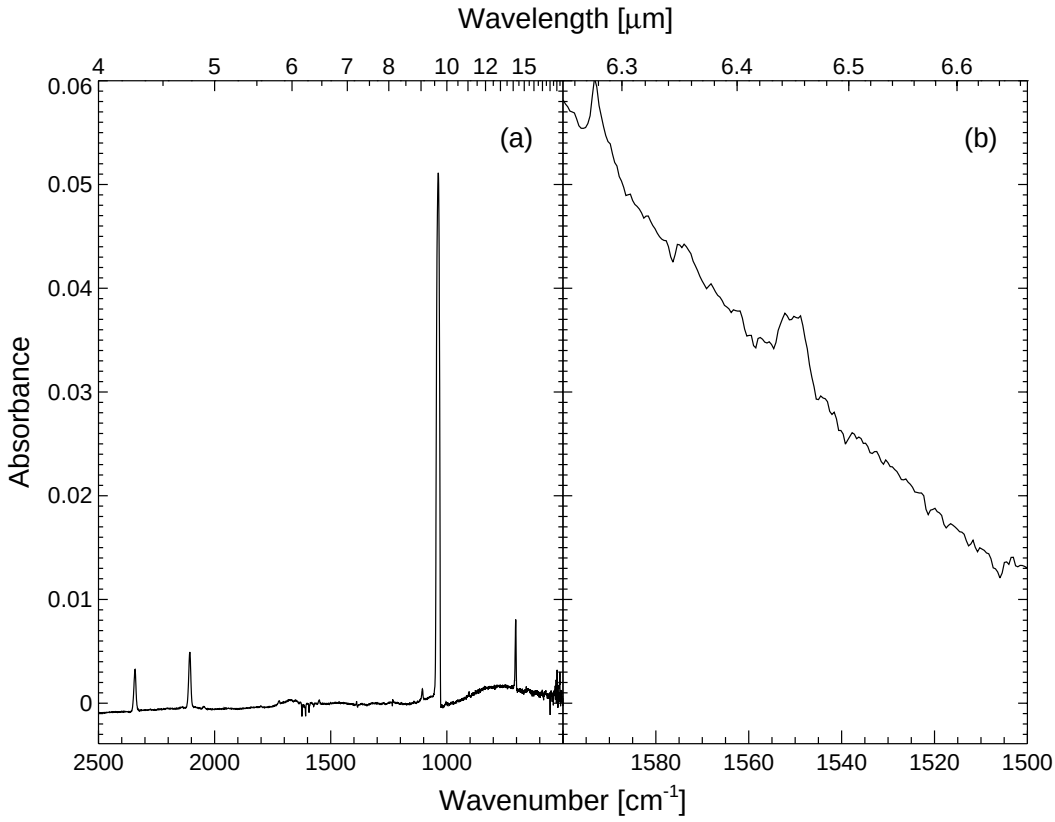

Figure 4.11: Spectrum of O_2 ice after 1 hr UV irradiation at T = 10 K: (a) 2500–500 cm^{-1} (4.0–20.0 μm), six features of O_3 are present in this region (see Table 4.6); (b) enlargement $\times$20 of the 1600–1500 cm^{-1} (6.25–6.67 μm) region of (a), displaying the 1550 cm^{-1} (6.452 μm) matrix-induced absorption of O_2.

tra after 1 min of UV irradiation. Although O_2 is a homo-nuclear diatomic species whose vibrational transitions are usually IR inactive (due to the lack of an intrinsic molecular dipole moment), its vibrational transition has been shown to absorb weakly when situated in a matrix of molecules with which it interacts (Cairns & Pimentel 1965; Ehrenfreund et al. 1992).

The abundance of deposited O_2 was estimated using the method described in § 4.2.2. The abundance of O_3 produced was calculated using the gas-phase absorption strength strength of its 1040 cm^{-1} (9.615 μm) asymmetric stretching fundamental (ν_3), $A = 1.4 \times 10^{-17}$ cm molec^{-1} (Smith et al. 1985). Hence, it was estimated that 36 % of the initially deposited O_2 was converted to O_3 after 1 hr of

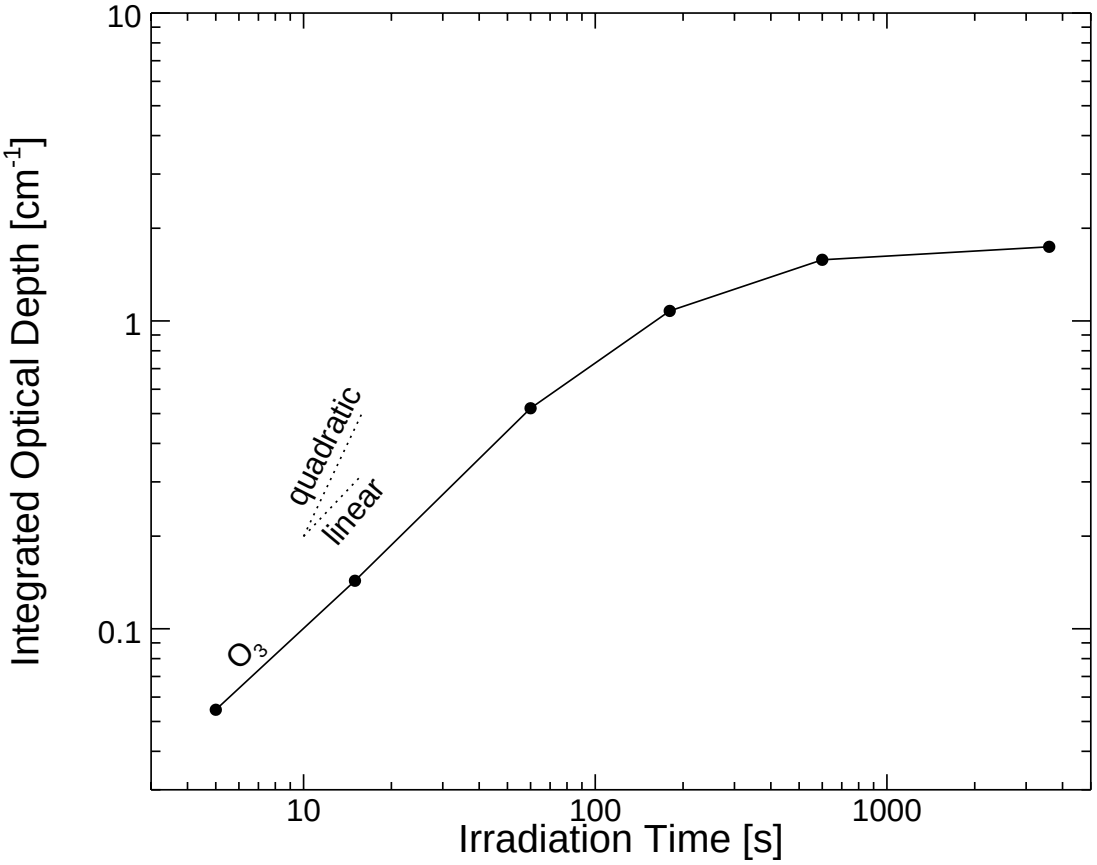

Figure 4.12: Evolution of the ν_3 feature of O_3 at 1043 cm^{-1} (9.615 μm) in the O_2 irradiation at T = 10 K. The dotted lines indicate linear and quadratic time dependencies.

UV irradiation at 10 K.

4.3.8 H_2CO

Figure 4.13 shows the unirradiated H_2CO spectrum at 10 K, that of the same ice after 1 hr of UV photolysis, and again after subsequent warm-up to 190 K. Many new features appear upon photolysis, and the irradiated spectrum bears little similarity to that of the initially deposited ice. The spectrum after warm-up to 190 K shows strong residue features, pointing to the presence of highly refractory species. Positions and identifications of new features are listed in Table 4.7. The main product is the formaldehyde polymer polyoxymethylene (POM), with relatively smaller yields of CO and HCO. Abundances for assigned species after 1 hr of photolysis are

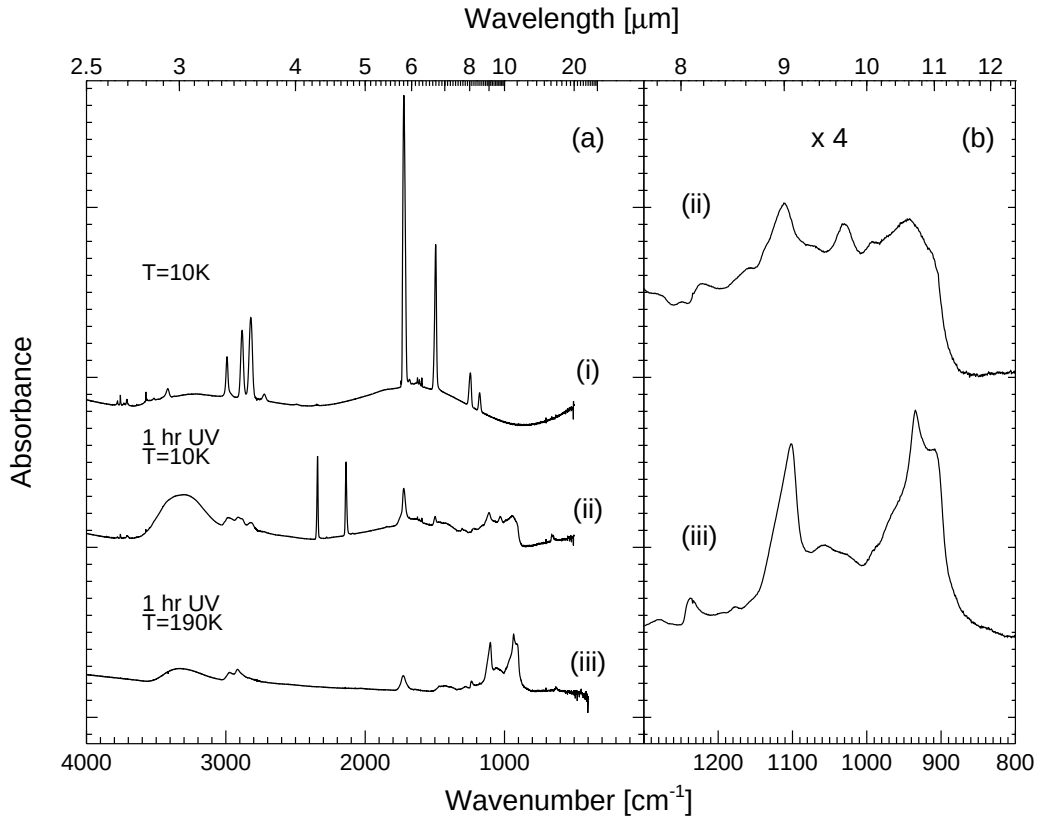

Figure 4.13: Spectrum of H_2CO ice: (i) after deposition; (ii) after 1 hr UV irradiation at T = 10 K; (iii) after irradiation and warm-up to T = 190 K. (a) full spectrum; (b) enlargement ×4 of curves (ii) and (iii) in the 1300 to 800 cm^{-1} (7.7 to 12.5 μm) region to clearly display the features of POM. Sinusoidal baseline behavior is due to scattering in the two Ar layers (§ 4.2.2).

given in Table 4.8.

The CO feature continued to grow over the entire irradiation, even after almost all H_2CO had been consumed by the photolysis. This indicated an additional source of CO– presumably the POM chains abundantly produced in later irradiation stages.

The 1722 cm^{-1} (5.807 μm) feature was assigned to the aldehyde C=O stretching mode (the terminal group of POM chains). Methyl formate (H_3COHCO; "MF"), the smallest product of H_2CO polymerization, may also have contributed to this feature. The presence of MF was confirmed by a second feature at 1161 cm^{-1} (8.613 μm) in the spectra, near the position of the C–O stretching mode of the ester group (–

Table 4.7: Features observed during the photolysis of solid H_2CO at T = 10 K. Product order is given for features whose evolution is displayed in Fig. 4.14.

Position cm^{-1} (μm)	Assignment	Order	Ref
627 (15.9)	POM[a]		1
656 (15.2)	CO_2		2
944 (10.6)	POM		1
993 (10.1)	POM		1
1030 (9.709)[b]	CH_3OH	2+	2
1071 (9.337)	C–OH; ν(C–O)		3
1110 (9.009)[b]	POM	1	1
1161 (8.613)	MF[c]; ν(C–O)		3
1223 (8.177)	POM		1
1283 (7.794)	unid.		
1304 (7.669)[b]	CH_4	2+	2
1351 (7.402)	unid.		
1381 (7.241)	POM		1
1428 (7.003)	POM		1
1440 (6.944)	POM-i[d]; δ(C–H)		3
1468 (6.812)	POM		1
1722 (5.807)[b]	MF + C=O endgrp	2+	1
1844 (5.423)[e]	HCO	1	4
1863 (5.368)[e]	HCO	1	5
2090 (4.785)	^{13}CO		2
2138 (4.677)[b]	CO	1	2
2244 (4.456)	C_3O		6
2277 (4.392)	$^{13}CO_2$		2
2342 (4.270)[b]	CO_2	2+	2
2911 (3.435)	POM		1
3300 (3.030)	POM-i; ν(O-H)		3
4140 (2.415)[b]	H_2		7

[a] Polyoxymethylene, $HCO[CH_2O]_nH_2COH$.

[b] Growth curve shown in Fig. 4.14.

[c] Methyl formate, H_3COHCO.

[d] POM isomer, $HCO[HCOH]_nH_2COH$.

[e] Combination of 1844 and 1863 cm^{-1} (5.423 and 5.368 μm) features used for HCO growth curve.

REFERENCES.—(1) Schutte, Allamandola, & Sandford 1993; (2) Hudgins et al. 1993; (3) Pouchert 1981; (4) Schutte 1988; (5) Milligan & Jacox 1971; (6) DeKock & Weltner 1971; (7) Sandford & Allamandola 1993.

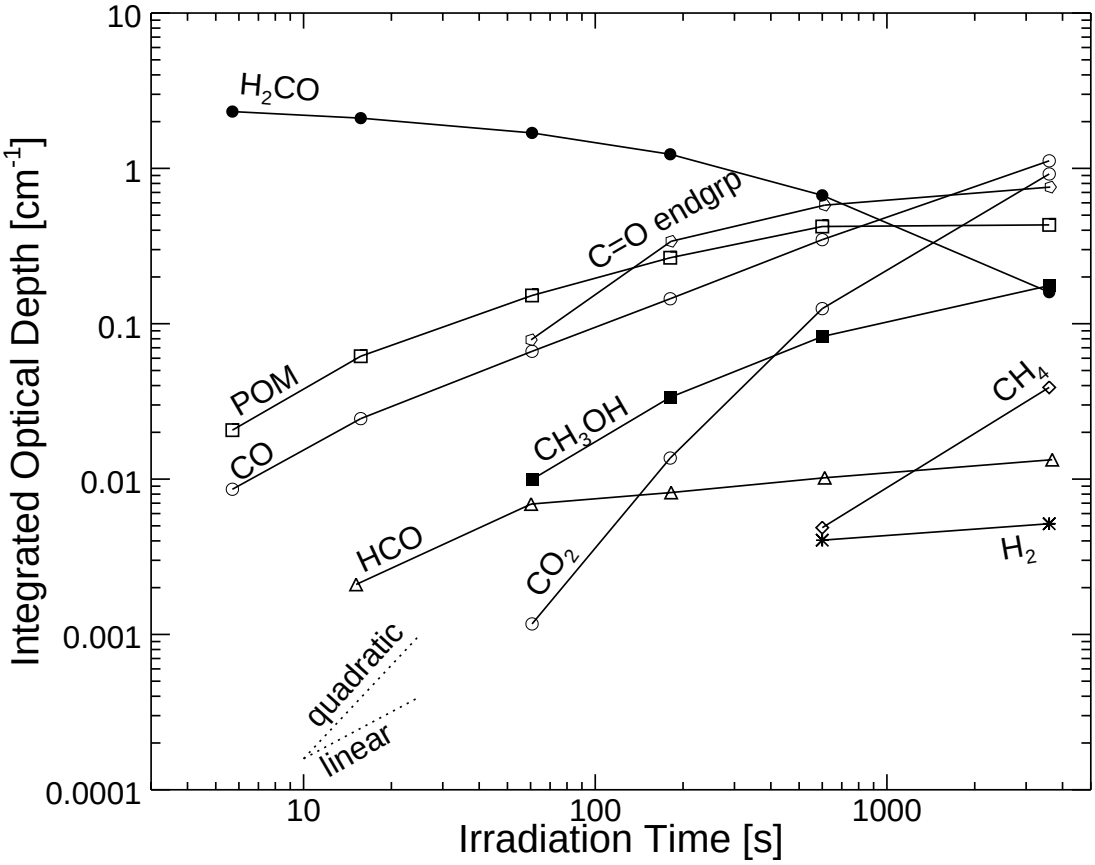

Figure 4.14: Evolution of features irradiation of H_2CO, represented by its 1494 cm^{-1} (6.693 μm) feature. All others are indicated in Table 4.7. The dotted lines indicate linear and quadratic time dependencies.

C–O–HCO). The MF features disappeared between 115 and 190 K, indicating that their carrier was a molecule with approximately the same volatility as CH_3OH, consistent with the proposed assignment.

Features at 1844 and 1863 cm^{-1} (5.423 and 5.368 μm) were attributed to solid HCO in two different matrix sites. These features show the same initial growth during irradiation and the same warm-up behavior, although the 1844 cm^{-1} (5.423 μm) feature became relatively weaker after 1 hr of photolysis. The position of the 1863 cm^{-1} (5.368 μm) absorption coincided with that of HCO seen by Hagen (1982; and references therein) for ice matrices dominated by CO. The 1844 cm^{-1} (5.423 μm) feature is close is position to that of HCO observed by Schutte (1988) in

Table 4.8: Abundances of products in H_2CO ice after 1 hr UV irradiation at T = 10 K.

Product	Position cm^{-1} (μm)	A[a]	Ref	Abund.[b]
POM[c]	944 (10.6)	3.0[d]	1	33[d]
CO	2138 (4.677)	1.1	2	15
POM-i[e]	3300 (3.030)	4.2[d]	3	11[d]
C=O endgrp	1722 (5.807)	2.3[d]	3	6.9[d]
H_2CO	1494 (6.693)	0.39	1	5.8
CO_2	2342 (4.270)	7.6	2	2.1
CH_3OH	1030 (9.709)	1.8	4	1.5
CH_4	1304 (7.669)	0.61	4	0.7
HCO	1863 (5.368)	0.10[f]		0.01

[a] IR absorption strength, in units of 10^{-17} cm molec^{-1} unless otherwise noted.
[b] % relative to initial H_2CO deposition.
[c] Polyoxymethylene, $HCO[CH_2O]_nH_2COH$.
[d] Refers to number of C atoms as opposed to number of molecules.
[e] POM isomer, $HCO[HCOH]_nH_2COH$.
[f] Assumed for HCO.

References.— (1) Schutte, Allamandola, & Sandford 1993; (2) this work, Ch. 3; (3) Wexler 1967; (4) d'Hendecourt & Allamandola 1986; (5) Sandford & Allamandola 1993.

mixtures with H_2O. Hence, the areas of both features have been combined to give the growth curve seen in Fig. 4.14.

After warm-up to 190 K (where background H_2O evaporates, see § 4.2.2), the spectrum is dominated by the POM features. A strong feature was observed centered at 3300 cm^{-1} (3.030 μm), due to the O–H stretch of the POM isomer, $HCO[HCOH]_nH_2COH$ ("POM-i"). Such structures are well-known polymerization products of H_2CO (Walker 1964). It should be noted, however, that no features were found which could be attributed to glycoaldehyde (CH_2OHHCO; Sodeau & Lee 1978). Thus, the observed polymers should contain as least three carbon atoms (e.g., glyceraldehyde, $HOCH_2HCOHHCO$, which has been proposed as a possible precursor to organic residues produced in irradiation experiments involving H_2O:CO:NH_3 mixtures Agarwal et al. 1985; Schutte 1988; Briggs et al. 1992).

Absorption strengths and relative abundances of final products of the H_2CO

irradiation are listed in Table 4.8. The listed abundances account for 76.1 and 78.2 % of the initial carbon and oxygen atoms, respectively. These discrepancies may be accounted for by errors in the absorption strengths, which may be uncertain by factors of 1.5 to 2 for some molecules (see discussion in Boogert et al. 1997), or to some extent by the carriers of the unidentified features.

4.3.9 CH_3OH

Figure 4.15 displays the unirradiated spectrum of solid CH_3OH at 10 K, along with the spectrum following 1 min and 1 hr of UV photolysis. Many new features are evident, indicating a complex photochemistry. Features that appeared during the photolysis are listed in Table 4.9. The evolution curves of selected features are shown in Fig. 4.16.

At later stages of the photolysis, the feature listed at 1718 cm^{-1} (5.821 μm) appeared as a broad component underneath the sharper absorption of formaldehyde. In the H_2CO irradiation (§ 4.3.8) this feature was assigned to the combination of aldehyde end groups on POM chains and MF. Since no POM was observed in the CH_3OH irradiation, it was assigned exclusively to MF in this case. The presence of MF was also indicated by the appearance of a feature at 1160 cm^{-1} (8.621 μm; identical to that observed in the H_2CO irradiation), as well as a weak third feature at 910 cm^{-1} (11.0 μm). Rather than large polymers (as in the H_2CO photolysis, § 4.3.8), the H_2CO produced in the CH_3OH photolysis was converted to relatively small products. This is most likely related to its low concentration in the ice matrix– < 8 % at any stage of the experiment. From Table 4.10, it may be seen that after CO, MF was the most abundant product at long irradiation times.

The features that appeared at 1850 and 1863 cm^{-1} (5.405 and 5.368 μm) have been attributed to the HCO radical. Both appeared simultaneously, showed the same warm-up behavior, and were gone at T = 60 K. As observed in the H_2CO photolysis (§ 4.3.8), their presence indicates two different HCO matrix sites. In this experiment, the 1850 cm^{-1} (5.405 μm) feature was only $\sim$ 2 times stronger than that at 1863 cm^{-1} (5.368 μm), and their relative strengths remained almost constant throughout the irradiation. The sum of the two HCO absorptions was

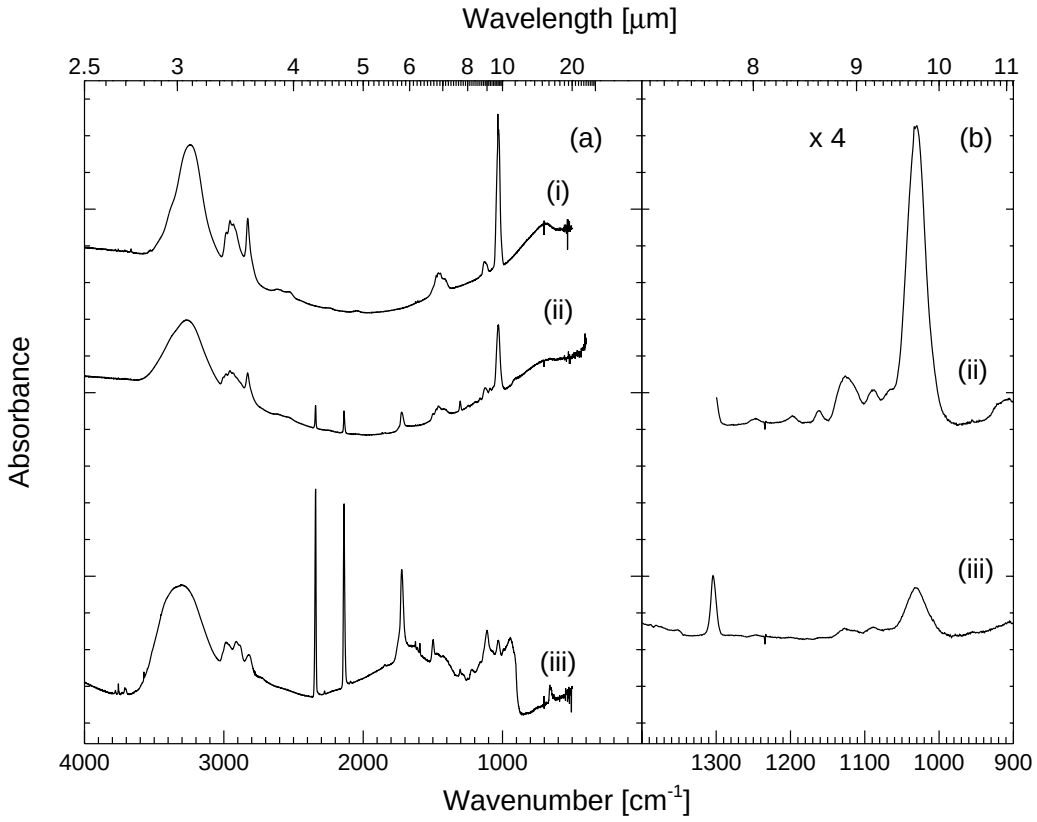

Figure 4.15: Spectrum of solid CH_3OH ice at T = 10 K: (i) after deposition; (ii) after 10 min UV photolysis– first-order products are seen; (iii) after 1 hr UV irradiation. (a) Full spectrum; in (b), the 1350–950 cm^{-1} (7.4–10.5 μm) regions of (ii) and (iii) are enlarged $\times 4$ for comparison. The sinusoidal baseline behavior is due to scattering in the two Ar layers (§ 4.2.2).

used to monitor its time dependence (Fig. 4.16).

Higher-order alcohols such as ethanol (CH_3CH_2OH) and ethylene glycol ($HOCH_2CH_2OH$) typically display a feature near 1085 cm^{-1} (9.217 μm; Pouchert 1981) and therefore may be responsible for the absorption at 1088 cm^{-1} (9.191 μm) observed in these experiments. However, a second feature of these species with approximately the same strength located near 880 cm^{-1} (11.4 μm) was not observed. The 1088 cm^{-1} (9.191 μm) feature disappeared between 120 and 230 K, indicating a carrier with about the same volatility as CH_3OH.

Features observed at 1197 and 1352 cm^{-1} (8.354 and 7.396 μm) coincided

Table 4.9: Features observed during the photolysis of solid CH_3OH at T = 10 K. Product order is listed for features whose evolution is displayed in Fig. 4.16.

Position cm^{-1} (μm)	Assign.	Order	Ref
655 (15.3)	CO_2		1
910 (11.0)	MF[a]		2
1088 (9.191)	C–OH str		3
1160 (8.621)	MF; ν(C–O)		3
1197 (8.354)	CH_2OH		4
1244 (8.039)[b]	H_2CO	1	2
1304 (7.669)[b]	CH_4	1	1
1352 (7.396)	CH_2OH		4
1497 (6.680)	H_2CO		2
1718 (5.821)[b]	MF	2+	2
1719 (5.817)	H_2CO		2
1850 (5.405)[c]	HCO	?	5
1863 (5.368)[c]	HCO	?	6
2092 (4.780)	^{13}CO		1
2138 (4.677)[b]	CO	2+	1
2278 (4.390)	$^{13}CO_2$		1
2342 (4.270)[b]	CO_2	2+	1
3011 (3.321)	CH_4		1
4140 (2.415)[b]	H_2		7

[a] MF = methyl formate, H_3COHCO.

[b] Growth curve shown in Fig. 4.16.

[c] Combination of 1850 and 1863 cm^{-1} (5.405 and 5.368 μm) features used for HCO growth curve.

REFERENCES.— (1) Hudgins et al. 1993; (2) Schutte, Allamandola, & Sandford 1993; (3) Pouchert 1981; (4) Jacox 1981; (5) Schutte 1988; (6) Milligan & Jacox 1971; (7) Sandford & Allamandola 1993.

reasonably well (within 1 %) with those reported for the CH_2OH radical at 1183 and 1334 cm^{-1} (8.453 and 7.496 μm) produced in the irradiation of Ar:CH_3OH = 200:1 mixtures by Jacox (1981). The methoxy radical (CH_3O) could not be detected in these experiments, since its features near 1040 and 2820 cm^{-1} (9.615 and 3.546 μm; Chesters & McCash 1987) overlap with strong CH_3OH absorptions.

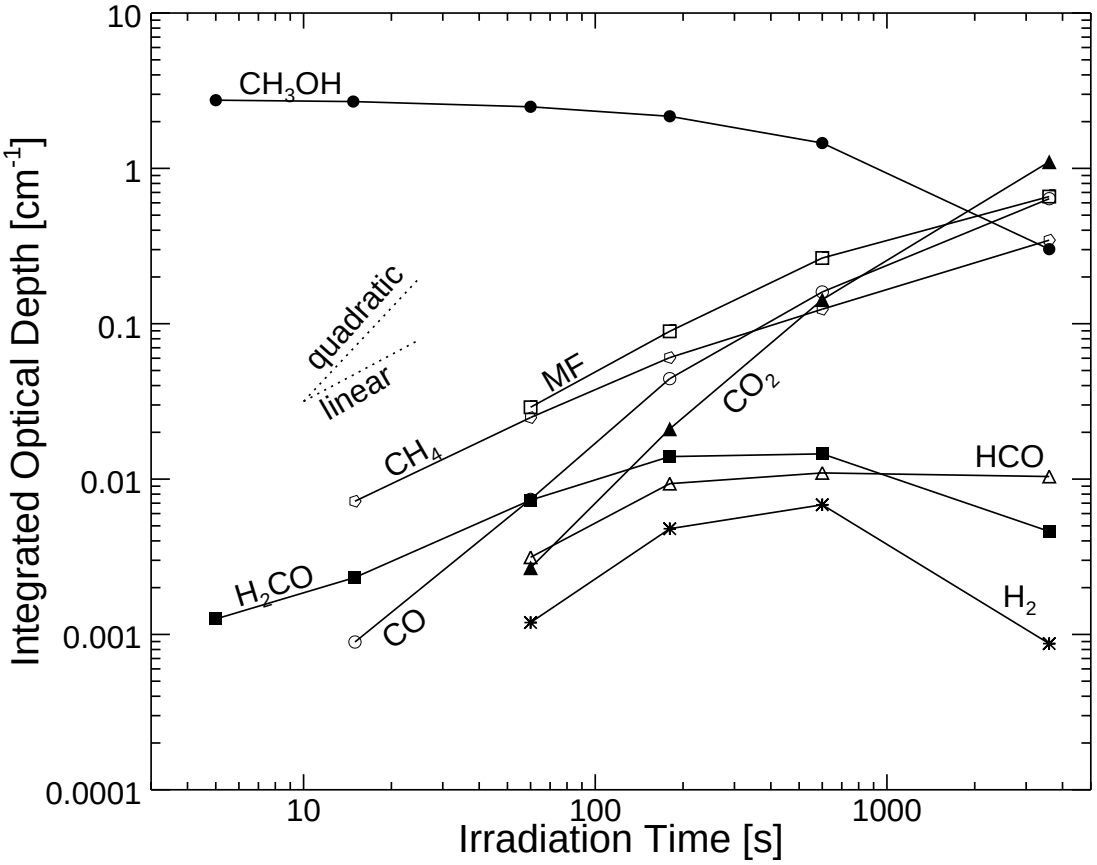

Figure 4.16: Evolution of features in irradiation of CH_3OH, represented by its 1026 cm^{-1} (9.747 μm) feature. All others are indicated in Table 4.9. MF = methyl formate, H_3COHCO. The dotted lines indicate linear and quadratic time dependencies.

4.3.10 Destruction and Formation Cross Sections

The initial destruction of a species due to UV irradiation in an optically thin ice sample of abundance N_0 is given by

$$N(t) = N_0 \exp(-\sigma_{\mathrm{des}} \cdot \phi \cdot t) \tag{4.1}$$

where σ_{des} is the UV destruction cross section, ϕ is the flux of UV photons, and t is the irradiation time. Typically, σ_{des} does not only depend on the photodissociation of the species, but also on the possibility of secondary reactions with other photolysis products.

Table 4.10: Abundances of products in CH_3OH ice after 1 hr UV irradiation at T = 10 K.

Product	Position cm^{-1} (μm)	A[a]	Ref	Abund.[b]
CO	2138 (4.677)	1.1	1	39
MF[c]	1718 (5.821)	1.2	2	13
CH_3OH	1026 (9.747)	1.8	3	11
CO_2	2342 (4.270)	7.6	1	9.3
CH_4	1302 (7.669)	0.61	3	8.0
HCO	1863 (5.368)	1.0[d]		0.67
H_2CO	1497 (6.680)	0.39	4	3.0
H_2	4140 (2.415)	≥ 0.009	5	≤ 5.9

[a] IR absorption strength, in units of 10^{-17} cm molec^{-1}.
[b] % relative to initial CH_3OH deposition.
[c] MF = methyl formate, H_3COHCO.
[d] Assumed for HCO.
REFERENCES.—(1) this work, Chapter 3; (2) Wexler 1967; (3) d'Hendecourt & Allamandola 1986; (4) Schutte, Allamandola, & Sandford 1993; (5) Sandford & Allamandola 1993.

As an example of the validity of Eq. (4.1), Fig. 4.17 shows a semi-log plot of CH_4 abundance vs. time in the methane irradiation experiment (§ 4.3.3). Initially, the destruction rate has an exponential behavior, but drops in later times. This is a general property for all of the experiments in this Chapter, primarily due to the re-formation of original species from their photoproducts. Changes in the optical properties of the ice sample may also change the UV penetration and add to this effect (i.e., the ice may become optically thick to the irradiating photons).

To derive $\sigma_{\rm des}$, fits in the functional form of Eq. (4.1) were made in all experiments to the first five points of the abundance vs. time data (at t = 0, 5, 15, 60, and 180 s). For the destruction rate of H_2CO, only the first four points were used, since its destruction rate already loses its exponential character after 60 s.

In some cases, this procedure was not even feasible. For H_2O (§4.3.1), problems arose due to constant deposition of background gases and hydrogen bonding between initially isolated H_2O molecules (§4.2.2). Molecules initially isolated in the Ar layer created a similar difficulty in the NH_3 experiments (§ 4.3.2). In § 4.3.4, the CO

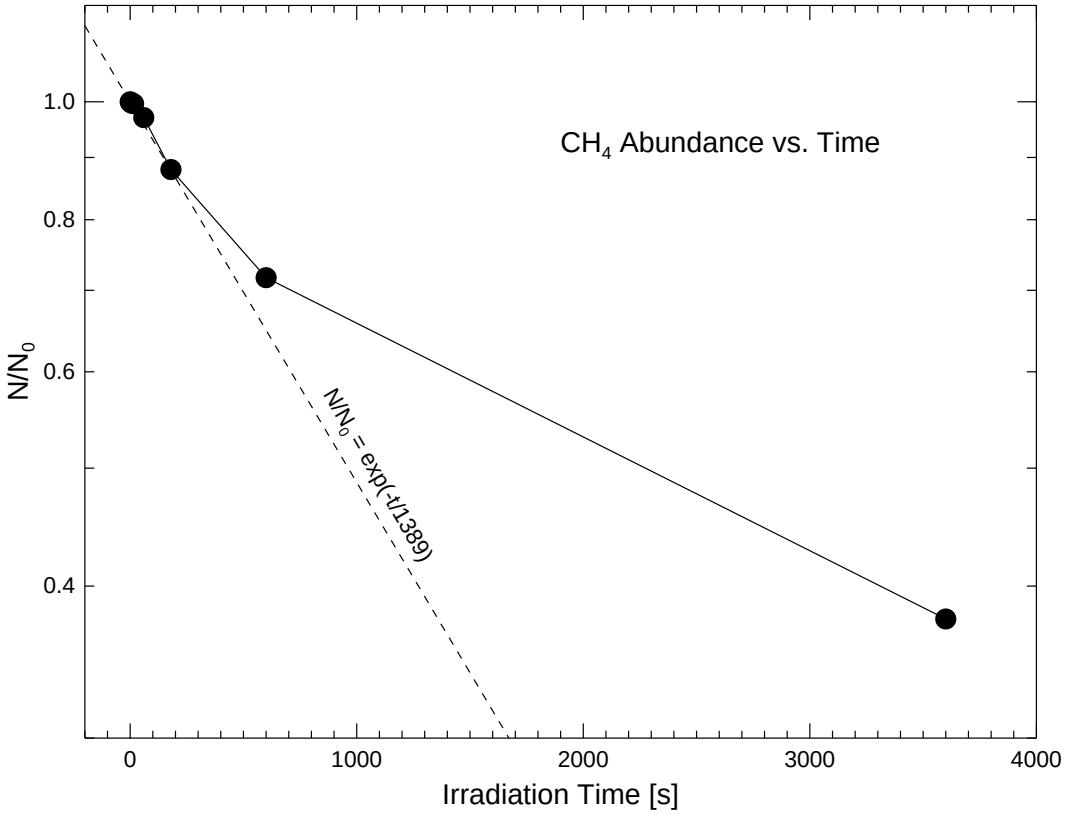

Figure 4.17: Demonstration of fits used to determine destruction cross sections. $\sigma_{\rm des}$ is given by the slope of a linear fit to points at t = 0, 5, 15, 60, and 180 s (dashed line; cf., Eq. 4.1).

feature did not measurably weaken, even after 1 hr of irradiation. Therefore, only an upper limit for its destruction cross section was estimated (Table 4.11). In order to measure $\sigma_{\rm des}$ for oxygen, the O_2 column density vs. time was indirectly calculated based on the observed O_3 abundance (in all other respects, the measurement was identical to those of the other ices).

In a number of cases, destruction was only partially caused by direct photon absorption: reactions with photoproducts also made a major contribution. In the case of O_2, the cross section for destruction due solely to photodissociation may have a value which is only one-third of $\sigma_{\rm des}$, since both O atoms have a high probability of reacting with a neighboring O_2 molecule to form O_3 when released by dissociation in the O_2 ice matrix (i.e., the sequence $3O_2 + h\nu \rightarrow O + O + 2O_2 \rightarrow 2O_3$ is initiated

Table 4.11: Initial destruction cross sections for sample ices ($\sigma_{\rm des}$) and formation cross sections for first-order products ($\sigma_{\rm form}$), assuming a lamp flux of $\phi = 10^{15}\,{\rm cm^{-2}\ s^{-1}}$.

Ice	$\sigma_{\rm des}$ $[10^{-18}\,{\rm cm}^2]$	Product	$\sigma_{\rm form}$ $[10^{-18}\,{\rm cm}^2]$
CO	< 0.08[a]	CO_2	0.013
CO_2	0.56	CO	0.38
O_2	3.2[b]	O_3	2.1
CH_4	0.72	C_2H_6	0.32
H_2CO	6.2	POM[c]	3.8
		HCO	0.31
		CO	0.15
CH_3OH	1.6	H_2CO	1.1
		CH_4	0.44

[a] Loss of CO is below resolution of measurements.
[b] Loss of O_2 esitmated from the formation rate of O_3.
[c] CH_2O groups.

through the action of only one UV photon, and three O_2 molecules are thus converted to two O_3 molecules). Similar physical processes will enhance the destruction rates of the other species, with the possible exception of CH_3OH (see § 4.3.9).

It appears likely that the values of $\sigma_{\rm des}$ should show considerable dependences on ice environment and could differ significantly if other molecular species are present. In any case, Table 4.11 gives a number of base values that may be used to understand the results obtained for complex ices.

There is a large variation in $\sigma_{\rm des}$ for the molecules studied in this Chapter (Table 4.11). By far, the most susceptible species to UV in these experiments was H_2CO, related to its very efficient polymerization. Although the photo-destruction of H_2O and NH_3 could not be measured directly, their lack of abundant photoproducts (§ 4.3.1 and § 4.3.2) suggests that they are not efficiently destroyed in a pure ice environment. Errors in the estimation of $\sigma_{\rm des}$ are dominated by the uncertainty in the UV flux, and relative values of $\sigma_{\rm des}$ are accurate. However, the absolute scale could vary by about a factor of two.

Initial cross sections for the formation of first-order photoproducts, $\sigma_{\rm form}$ (in

cm^2), may be derived from

$$\frac{dN}{dt} = \sigma_{form} \cdot \phi \cdot N_0, \tag{4.2}$$

where N is the abundance of the product, N_0 is the initial abundance of the parent molecule, ϕ is the flux of UV photons, and t is the irradiation time. Where possible, σ_{form} was derived using a fit to the abundances of irradiation products at the first four irradiation time steps (at $t = 0, 5, 15$, and 60 s). The results of these calculations are listed in Table 4.11.

4.4 Reaction schemes

The main aim of this Chapter is to quantitatively describe the photochemical modifications of astrophysically relevant ices. For this reason, no in-depth investigation was made of the formation mechanisms of detected products. The possible reaction schemes which may explain the presence of observed species in these experiments (some well established, others more speculative), are summarized in the following sections.

4.4.1 H_2O and NH_3

Products observed in the H_2O irradiations were OH, HO_2, and H_2O_2 (§ 4.3.1). The photochemistry of the water molecule begins with either of these two steps (Okabe 1978):

$$H_2O + h\nu \rightarrow H + OH \tag{4.3}$$

or

$$H_2O + h\nu \rightarrow H_2 + O. \tag{4.4}$$

Reaction (4.4) is of minor importance (Okabe 1978) and this was supported in these experiments since no H_2 was observed. Subsequent steps then lead to the formation of H_2O_2 and HO_2 as follows:

$$OH + OH \rightarrow H_2O_2 \tag{4.5}$$

$$OH + H_2O_2 \rightarrow H_2O + HO_2 \tag{4.6}$$

Reaction (4.5) is the most likely candidate for the production of H_2O_2 in the H_2O experiments. The HO_2 molecule, observed here only in long irradiation time steps, may be produced by Reaction (4.6) or by the photodissociation of H_2O_2 (Okabe 1978 and references therein).

Species produced in the photolysis of NH_3 in § 4.3.2 were N_2H_4, NH_2, and H_2. Ammonia has two possible primary photolysis steps:

$$NH_3 + h\nu \rightarrow NH_2 + H \tag{4.7}$$

$$NH_3 + h\nu \rightarrow NH + H_2, \tag{4.8}$$

where Reaction (4.7) is dominant (Okabe 1978; Hagen 1982). The formation of N_2H_4 may occur by

$$NH + NH_3 \rightarrow N_2H_4, \tag{4.9}$$

or by

$$NH_2 + NH_2 \rightarrow N_2H_4. \tag{4.10}$$

If Reaction (4.9) is very efficient, then all NH radicals may be quickly lost to the NH_3 matrix to form N_2H_4, and thus its absence in the irradiated NH_3 spectra presented in § 4.3.2 may be explained.

4.4.2 CH_4

The UV photolysis of solid CH_4 at 10 K in these experiments (§4.3.3) produced ethane (C_2H_6), propane (C_3H_8), ethylene (C_2H_4), allene (C_3H_4), larger molecules containing H–C≡C– and H_2C=C– groups, and alkanes with $\geq$ 4 C atoms per molecule, consisting of highly branched structures (seen via R–CH_3 and R–CH_2–R stretching and deformation modes). The primary photodissociation pathways for methane involve (Okabe 1978):

$$CH_4 + h\nu \rightarrow CH_3 + H, \tag{4.11}$$

$$CH_4 + h\nu \rightarrow CH_2 + H_2, \tag{4.12}$$

and

$$CH_4 + h\nu \rightarrow CH + H_2 + H. \quad (4.13)$$

Subsequent steps involve reactions between CH, CH_2, CH_3, and CH_4 (e.g., Braun, Baas, & Pilling 1970; Okabe 1978). Such reactions include

$$CH + CH_2 \rightarrow C_2H_3, \quad (4.14)$$

$$CH_2 + CH_4 \rightarrow C_2H_6, \quad (4.15)$$

$$CH_2 + CH_2 \rightarrow C_2H_4, \quad (4.16)$$

and

$$CH_3 + CH_3 \rightarrow C_2H_6. \quad (4.17)$$

Large products may evolve from the addition of radicals to unsaturated species or other radicals, such as

$$CH + C_2H_3 \rightarrow C_3H_4 \text{ (allene)}, \quad (4.18)$$

$$CH_3 + C_2H_4 \rightarrow C_3H_7, \quad (4.19)$$

and

$$C_3H_7 + CH_3 \rightarrow C_4H_{10}. \quad (4.20)$$

Such a stepwise building block mechanism seems consistent with the highly branched structures inferred for the large hydrocarbons.

4.4.3 CO and CO_2

Products of the CO photolysis experiments were CO_2, C_2O, C_3O, and C_3. The direct photodissociation of the CO molecule has a threshold wavelength of 111.8 nm (Okabe 1978) and falls outside the range of the UV radiation applied in these experiments (§ 4.2). The alternative photochemical pathway lies through an

electronic excitation of CO and requires photons with $\lambda < 147.0\,\mathrm{nm}$ (Hagen 1982). An electronically excited CO molecule (CO^*) then reacts with other CO molecules to produce CO_2 and C atoms by the reaction

$$CO^* + CO \rightarrow CO_2 + C \tag{4.21}$$

(e.g., Luiti, Dondes, & Harteck 1966; Okabe 1978). Subsequent reactions occur between the C atoms and the CO matrix:

$$C + CO \rightarrow C_2O, \tag{4.22}$$

$$C + C_2O \rightarrow C_3O, \tag{4.23}$$

$$C_2O + CO \rightarrow C_3O_2, \tag{4.24}$$

and

$$C + C + C \rightarrow C_3 \tag{4.25}$$

(Okabe 1978).

The photolysis of CO_2 produced CO, CO_3, C_3O and O_3 in these experiments (§ 4.3.5). CO_2 dissociates by interaction with photons of $\lambda < 227.5\,\mathrm{nm}$ to form CO and O (Okabe 1978). Secondary reactions of between the CO and O atoms produced lead to CO_3, O_2 and O_3 (e.g., Moll, Ckitter, & Thompson 1966). The formation of CO_3 most likely occurs by reaction of CO_2 with an oxygen atom in its doublet state (as given by Okabe 1978):

$$CO_2 + O(^1D) \rightarrow CO_3^* \tag{4.26}$$

The CO produced by the direct photolysis of CO_2 may also follow the above scheme for CO to produce the trace of C_3O seen.

4.4.4 N_2 and O_2

No products of N_2 photolysis were clearly identified (§ 4.3.6), although some evidence exists for the formation of the N_3 radical. The wavelength threshold for the photodissociation of N_2 lies at 127.0 nm (Okabe 1978), and hence, if this molecule were to photo-dissociate, then speculatively, the formation of N_3 could take place by addition of an N atom to N_2.

The sole photolysis product of O_2 seen in these experiments (§ 4.3.7) was O_3, which may be formed after the photodissociation of O_2 and the subsequent addition of an O atom.

4.4.5 H_2CO and CH_3OH

New species observed in the UV irradiation of H_2CO (§ 4.3.8) were POM ($HCO[CH_2O]_nH_2COH$) chains, CH_3OH, CH_4, HCO, CO, CO_2, C_3O, H_2, methyl formate (H_3COHCO, "MF"), and the POM isomer $HCO[HCOH]_nH_2COH$ ("POM-i"). CO and HCO may be formed via the direct photodissociation of H_2CO (Okabe 1978). CO_2, and C_3O follow from the subsequent photolysis of CO (Reactions 4.21–4.23). CH_3OH is most likely formed through the rearrangement and reactions of H_2CO:

$$H_2CO + h\nu \rightarrow HCOH \tag{4.27}$$

and

$$H_2CO + HCOH \rightarrow CH_3OH + CO \tag{4.28}$$

(Kemper, Hoeks, & Buck 1981). Also, H atoms produced by H_2CO photolysis could recombine with H_2CO to form CH_3OH (Hiraoka et al. 1994). The combination of two H_2CO molecules may lead to the formation of MF (Goldanskii, Frank-Kamenetskii, & Barkalov 1973). The chains observed, POM and POM-i, are produced through H_2CO polymerization, where (presumably) the energy produced by UV absorption overcomes the reaction barrier of these reactions.

H_2CO, CH_4, MF, HCO, CO, CO_2, and H_2 are formed in the photolysis of solid

CH_3OH at 10 K (§ 4.3.9). The first-order products of CH_3OH observed in § 4.3.9 should be formed directly from its photodissociation:

$$CH_3OH + h\nu \rightarrow H_2CO + H_2 \quad (4.29)$$

$$CH_3OH + h\nu \rightarrow CH_4 + O \quad (4.30)$$

Reaction (4.30) is not observed in the gas phase (von Sonntag 1969), and more research (e.g., photolysis of CH_3OH in inert matrices) needs to be done to verify that CH_4 truly is a first order product of the solid-phase photolysis of CH_3OH.

Subsequent reactions to form HCO, CO, CO_2, and MF follow the scheme of H_2CO (above). No POM or $HCO[HCOH]_nH_2COH$ formaldehyde polymers are observed in the spectrum of irradiated CH_3OH (see § 4.3.9).

4.5 Discussion

These experiments have shown that a large number of species are produced upon UV photolysis of simple molecules. Among these are free radicals, and in some cases, large organic species. These results are consistent with earlier experiments involving somewhat more complex ice mixtures: i.e., H_2O:CH_3OH:NH_3:CO (Allamandola, Sandford, & Valero 1988), CO:H_2O, CO:NH_3 and CO:CH_4 (Hagen 1982), H_2O:CO:CH_4:NH_3:O_2:N_2 (d'Hendecourt & Allamandola 1986), and H_2O:-CO:O_2 (Ehrenfreund et al. 1992). In addition to many previously identified species, a large number of molecules not observed in earlier laboratory astrophysics experiments have been produced here. Examples of the latter include H_2O_2 and HO_2 (from H_2O photolysis), N_2H_4 (from NH_3), and methyl formate, CH_3OHCO (from CH_3OH and H_2CO).

The discrepancy between older photolysis experiments involving complex mixtures and those presented here may be due to the absence of species which easily react with the photodissociation products, thus increasing the efficiency of other reaction pathways. Also, the less-crowded IR spectra of simple ices enable a more sensitive search for new features. The higher sensitivity of modern spectrometers in comparison with instruments previously employed could also play a role. Certainly,

these many new identifications from initially pure ice samples stress the importance of studying individual ice components before attempting to understand the photochemistry of complex mixtures.

4.5.1 Astrophysical Implications

These results could have a number of astrophysical implications. Ramifications reach beyond the solid phase, since volatile species which are photochemically produced in the ice mantles could be injected into the gas phase by desorption mechanisms such as grain mantle explosions and cosmic-ray heating (e.g., Hasegawa & Herbst 1993; Shalabiea & Greenberg 1994). In warm dense cores close to star-forming regions, sublimation of the grain mantles also becomes significant.

A number of species identified in these experiments have been found in gas phase of dense clouds. Gas-phase C_2O and C_3O have each been detected in the dark cloud TMC-1 at abundances of 10^{-5} and 10^{-6} relative to gaseous CO, respectively (Ohishi et al. 1991). Methyl formate gas has been identified in the Orion compact ridge and in Sgr B2 (regions of ongoing massive star formation) at abundances of 2×10^{-4} and 2×10^{-5} relative to gas-phase CO, respectively, but has not been found in TMC-1 ($N/N_{\rm CO} < 10^{-5}$, Blake et al. 1987; Irvine, Goldsmith, & Hjalmarson 1987).

Models of gas-phase chemistry which include surface reactions and desorption from grains fall short by many orders of magnitude in reproducing the observed C_2O abundance, although the C_3O abundance may be reasonably reproduced (Hasegawa & Herbst 1993). It seems quite possible that photoproduction of these volatile species in the nonpolar, CO-rich phase of interstellar ices could be an important source of their observed gas-phase abundances. Methyl formate, on the other hand, may be efficiently produced in the gas phase in star-forming regions (Caselli, Hasegawa, & Herbst 1993; Charnley, Tielens, & Millar 1992), and the significance of direct injection from the grains is unclear in this case.

The high destruction rate observed for H_2CO (see Table 4.11) supports the conclusions by Schutte et al. (1996a) that the generally low observed abundance of H_2CO in interstellar ices could be related to its high susceptibility to photochemical

destruction. With the destruction cross section indicated in Table 4.11, 90 % of our H_2CO ice sample is destroyed at a dose of $R \approx 0.8$. Such doses could be quite realistic for grains near protostellar objects (Tegler et al. 1995; Schutte et al. 1996a).

The very efficient polymerization of H_2CO upon ultraviolet photolysis has been observed previously (Goldanskii, Frank-Kamenetskii, & Barkalov 1973; Mansueto & Wight 1989; Mansueto, Ju, & Wight 1989). H_2CO is an efficient source of organic species even at the relatively small concentrations produced by the irradiation of solid methanol: $\sim$ 26 % of the initial CH_3OH was converted into methyl formate (with H_2CO as an intermediate) after 1 hr of irradiation (§ 4.3.9). The results in §4.3.8 clearly show that under UV photolysis, H_2CO could be an efficient producer of organic molecules in icy grain mantles. Similar results have also been found in more complex ice mixtures (Bernstein et al., private communication). This mechanism could play a role in the formation of organic materials observed in comets and the diffuse ISM.

The continuous increase in complexity with irradiation dose for the CH_4 sample could have some interesting implications for the evolution of organic species in the ISM. Although this experiment may indicate that methane photolysis is an efficient source of organic species in interstellar ices, it remains to be investigated whether such a high yield is obtained from a mixture of CH_4 with other ice components such as CO or H_2O. Additionally, it is intriguing to consider this experiment as a template for the evolution of the refractory organic grain mantles observed in the diffuse interstellar medium (e.g., Tielens & Allamandola 1987; Sandford et al. 1991; Pendleton et al. 1994). It appears that under the influence of the strong ambient UV flux in the diffuse environment, a hydrocarbon material may increase in complexity. Such an evolution could be related to the durability of this organic material, which appears to survive for timescales $\sim 10^7$ to 10^8 yr in the harsh environments of the diffuse ISM (e.g., Greenberg 1982).

CHAPTER 5
METHODS OF OBSERVATIONAL SPECTROSCOPY WITH THE ISO SHORT-WAVELENGTH SPECTROMETER

"Few people realise the immensity of vacancy in which the dust of the material universe swims."

H. G. Wells, *The War of the Worlds*, Book I, Chapter the First

5.1 Description of the Instrument

The Infrared Space Observatory (ISO) was launched on November 17, 1995 by the European Space Agency (ESA) and has provided astronomers with an unprecedented view of the infrared region of the electromagnetic spectrum from $\lambda = 2.5$ to 240 μm. It consists of a large (2000 liter) liquid Helium cryostat that cools the instruments to 2 K, a 60 cm (f/15) telescope, a service module, and four scientific instruments (short- and long-wavelength spectrometers, imaging camera, and photo-polarimeter). A diagram of the telescope is given in Figure 5.1. A complete description of ISO and its mission can be found in the ISO Observer's Manual.[8]

The SWS was developed and constructed by the Space Research Organization of the Netherlands (SRON) and the Max Planck Institüt für Extraterrestriche Physik (MPE). It consists of two grating spectrometers which use a 100 lines/mm grating in the first 4 orders from 2.4 to 13 μm, and a 30 lines/mm grating in the first 2 orders from 11 to 45 μm. A complete description of the ISO Short-Wavelength Spectrometer (SWS) can be found in de Graauw et al. (1996) and the SWS Observer's Manual.[9]

When all possible combinations of grating order, aperture, and detector array are applied, the full wavelength range covered by the SWS is split up into 12 different

[8]Available on-line at `http://isowww.estec.esa.nl/manuals/ISO_man/isoobs3_1.html`.
[9]Available on-line at `http://isowww.estec.esa.nl/manuals/SWS_man/obsman.html`.

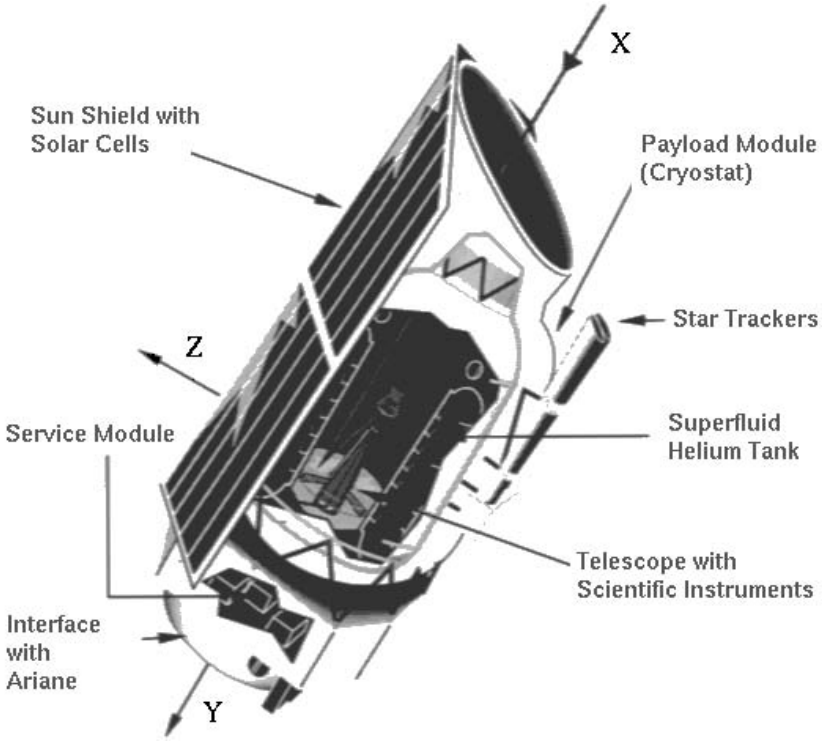

Figure 5.1: Diagram of the Infrared Space Observatory, ISO (from ISO Observer's Manual, Figure 1).

overlapping spectral bands (which are labeled 1A, 1B, 1D, 1E, 2A, 2B, 2C, 3A, 3C, 3D, 3E, and 4). The highest spectral resolution possible is different in each band and ranges from from $\lambda/\Delta\lambda \approx 1000$ to 2000. For a detailed description of the wavelength ranges and resolutions of each SWS band, see de Graauw et al. (1996), Table 1.

The SWS is designed for three major types of Astronomical Observing Templates (AOTs), two of which have been implemented in Chs. 6 and 7. The first template (AOT SWS01) observes the full wavelength range of $\lambda = 2.38$ to $45.2\,\mu$m with one of four different speeds that determine the resulting spectral resolution. Scan times in AOT SWS01 are approximately 0.25, 0.5, 1, and 2 hr with respective resolving powers of 1/8, 1/8, 1/4, and 1/2 of the full SWS resolution. The second template (AOT SWS06) is designed for smaller wavelength regions with longer integration times at full resolution. Actual integration times depend on the required sensitivity.

5.2 Data Reduction Methods

A detailed description of the SWS's calibration and data reduction techniques can be found in de Graauw et al. (1996), Schaeidt et al. (1996), and Valentijn et al. (1996). In this section, I describe the general data reduction procedure applied to the data presented in Chs. 6 and 7.

Wavelength scanning in an observation is achieved by the rotation of a flat mirror located near each grating. Every region of the spectrum is scanned at least twice, in pairs of "up" and "down" scans whose names refer to the scan direction in wavelength space.

The "pipeline" data reduction techniques developed at SRON in Groningen, the SIDT at VILSPA, Spain, and MPE in Garching, Germany were used to derive optical depth spectra. Dark currents for each detector over the total scan time were removed by the interpolation of measurements taken at the beginning and end of each scan. Data were converted to astronomical flux density units (Jy) from instrument signal level (μV s^{-1}) by division of the Relative Spectral Response Function (RSRF) for each SWS band. The wavelength dependence of the RSRF is highly oscillatory in SWS bands 3A through 3D (12–30 μm; see de Graauw et al. 1996), and if the observed data are shifted in wavelength with respect to the calibration data, a beating or "fringing" pattern results when the RSRF is divided out. Fringing effects were minimized using an interactive routine which applied small wavelength shifts to the responsivity curves before the division. In most cases, however, some small amount of fringing did remain in the spectra. If reliable analyses were still possible, this residual fringing was not removed since attempts to do so (such as clipping high-frequency components from the Fourier transform) slightly alter the shape of existing absorptions.

Scans in each SWS band free of obvious glitch effects or response jumps were combined and fit with a straight line. This line was then used to flatfield each scan individually. Up and down scans were independently flatfielded in this way to correct for anomalous trends in dark current, and final spectra were obtained by an average of each up/down pair.

5.3 Laboratory Modeling of SWS Data

In order to derive information about ice environment from ISO-SWS spectra, the profiles of observed features must be compared to those of laboratory ices in an appropriate range of ice matrices. The details of creating laboratory ice analogs and obtaining their IR optical depth spectra have been outlined in Ch. 2.

5.3.1 Optical Constants

The observed shapes and peak positions of strong absorptions depend on the shape and size of the interstellar grain upon which the ices reside. In the laboratory, the spectra of ices are obtained by depositing thin films ($l \sim 1$–$5\,\mu$m) onto a flat substrate, but interstellar ices are thought to be frozen as a mantle on top of ellipsoidal grains with a certain size and shape distribution. When the ice features are sharp, and the index of refraction changes by large amounts across the frequency range of the absorption, scattering effects become important. Therefore, direct comparison between laboratory and interstellar data is not possible in most cases.

However, the laboratory-obtained IR spectra may be modified so that they represent particles with an assumed size and shape distribution if the real and imaginary parts of the ice's refractive index, $\mathbf{m} = n + ik$, are known (n and k are often referred to as the *optical constants* of the ice in question). The optical constants of an ice may be determined using a Kramers-Kronig analysis of the laboratory transmission spectra (e.g., Hudgins et al. 1993). The Kramers-Kronig dispersion relations give:

$$n(\nu) = 1 + \frac{1}{2\pi^2} \int_0^\infty \frac{\alpha(\nu')}{(\nu'^2 - \nu^2)} d\nu' \tag{5.1}$$

$$\alpha(\nu) = \frac{4\pi k(\nu)}{\lambda} \tag{5.2}$$

$$= \frac{1}{h} \left[\tau(\nu) + \ln \left| \frac{\mathbf{t_{01}} \mathbf{t_{12}} / \mathbf{t_{02}}}{1 + \mathbf{r_{01}} \mathbf{r_{02}} \exp(4i\pi h \mathbf{m}/\lambda)} \right|^2 \right], \tag{5.3}$$

where $\alpha(\nu)$ is the absorption coefficient, $\tau(\nu)$ is the optical depth spectrum, h is the ice thickness, and $\mathbf{t_{ij}}$ and $\mathbf{r_{ij}}$ are the complex coefficients for photon transmission and reflection (respectively) at the boundary between the $i^{\rm th}$ and $j^{\rm th}$ layer (e.g.,

0 = substrate, 1 = ice, and 2 = vacuum).

In principle, we must carry out the integration in Eq. (5.1) over all frequencies. However, since electronic absorption bands (in the visible and UV parts of the spectrum) are well-separated from the IR, they contribute only a constant term to the integral. Thus, Eq. (5.1) may be approximated as

$$n(\nu) \approx n_0 + \frac{1}{2\pi^2} \int_{\rm IR} \frac{\alpha(\nu')}{(\nu'^2 - \nu^2)} d\nu', \tag{5.4}$$

where n_0 is the value of n at high frequencies (present in the literature; e.g., Hudgins et al. 1993 and references therein), and the integration is limited to the IR part of the spectrum.

Since n and k are not independent quantities, results must be obtain iteratively. To begin the iteration, it is initially assumed that $n(\nu) = n_0$. Once both n and k have been calculated using Eqs. (5.3) and (5.4), they are used to create an "artificial" spectrum using Eq. (5.3). This is compared to the original input spectrum and if the differences are outside the desired tolerance, the process begins again with the current values of n and k as the starting point.

5.3.2 Grain Shape Effects

In the long-wavelength limit, and when extinction due to scattering may be neglected, a simple expression for the absorption cross section $C_{\rm abs}$ of ellipsoidal homogeneous particles can be derived (e.g., van de Hulst 1957; Bohren & Huffman 1983):

$$C_{\rm abs}/V = \frac{2\pi}{3\lambda} \sum_{i=1}^{3} \frac{2nk/L_i^2}{(1/L_i - 1 + n^2 - k^2)^2 + (2nk)^2} \quad , \tag{5.5}$$

where it is assumed that the grain resides in a vacuum, V is the grain's volume, n and k are the optical constants, and L_i is the geometry parameter which characterizes the shape of the particle ($0 \leq L_i \leq 1$, $i \rightarrow$ x, y, and z axes). Since there will be a resonance in $C_{\rm abs}$ when $n^2 - k^2 \approx 1 - 1/L_i$, the profiles of strong absorption features are very sensitive to the particle shape. For a particular shape, the peak value of $C_{\rm abs}$ is proportional to $1/nk$. For further details on the effect of grain shapes in the calculation of $C_{\rm abs}$, see Ehrenfreund et al. (1997) and references therein.

5.3.3 Modeling Procedure

A χ^2-minimization code was written to match the observed data to shape-corrected laboratory spectra in Chs. 6 and 7. Observed spectra were matched to a suite of laboratory data from the Leiden Observatory Laboratory (Ehrenfreund et al., 1996, 1997, 1998), applying a χ^2 minimization method similar to that used by Chiar et al. (1994, 1995) to fit solid-state CO features toward the Serpens and Taurus dark clouds. Particle shape corrections were applied to the lab data as described above using four different grain models.

Laboratory mixtures considered in the fits of Chs. 6 and 7 were separated into three categories: polar, nonpolar, and annealed ices; see Table 5.1 for a complete listing. Polar ices are dominated those by H_2O, and include mixtures such as H_2O:$CO_2 \approx 100$:15 and 1:1, H_2O:CH_3OH:$CO_2 \approx 100$:40:60 and 100:10:15 (at various temperatures from 10 to 80 K). Nonpolar ice mixtures come from Ehrenfreund et al. (1997) and include a wide variety of ice compositions dominated by the molecules CO_2, CO, O_2 and N_2. Nonpolar ice temperatures are 10 and 30 K except where the mixture is dominated by CO_2, in which case temperatures of 50 and 80 K are also included. Certain nonpolar mixtures contain a trace amount of H_2O (1–10 %). The annealed ices have the approximate composition of H_2O:CH_3OH:CO_2 = 1:1:1 upon initial deposition at 10 K and have been heated to high temperatures (80–145 K).

The fitting code minimizes χ^2 for each laboratory spectrum alone and also finds the best combination for each pair of laboratory spectra. It then chooses the fit with the lowest overall value of χ^2 as the final result. Further interpretation is required before determining the best fit, however, and the code output is used to find a *range* of appropriate fits. Other known properties of the line of sight in consideration must be used in order to choose the most valid fit. For example, in the case of Elias 16, fits which contained ices at T > 20 K were ruled out, since this line of sight probes the quiescent ISM where no internal sources of heating are present.

Table 5.1: Polar, annealed, and nonpolar laboratory mixtures (from Ehrenfreund et al. 1997) used in fits to ISO-SWS data.

Mixture	Lab T [K]	Refs
Polar:		1,2
H_2O:CO_2 = 100:14	10, 50, 80	
H_2O:CO_2 = 100:125	10, 30, 50, 80, 125	
H_2O:CO:CO_2 = 100:3:20	20	
H_2O:CH_3OH:CO_2 = 100:40:60	10, 50, 80, 140	
H_2O:CH_3OH:CO_2 = 100:10:15	10, 50, 80, 120	
Annealed:		3
H_2O:CH_3OH:CO_2 = 1:1:1	10, 65, 80, 90, 96, 105, 106, 110, 111, 112, 115, 116, 117, 118, 119, 120, 121, 123, 130, 136, 145	
Nonpolar:		1
Pure CO_2	10, 50, 80	
H_2O:CO_2 = 1:100	10, 30	
H_2O:CO_2 = 1:10	10, 80	
H_2O:CO_2 = 1:6	10, 50, 75	
CO:CO_2 = 100:4	10, 30	
CO:CO_2 = 100:8	10, 30	
CO:CO_2 = 100:16	10, 30	
CO:CO_2 = 100:21	10, 30	
CO:CO_2 = 100:23	10, 30	
CO:CO_2 = 100:26	10, 30	
CO:CO_2 = 100:70	10, 30	
H_2O:CO:CO_2 = 1:50:56	10, 45	
CO_2:O_2 = 1:1	10	
CO:O_2:CO_2 = 100:50:4	10, 30	
CO:O_2:CO_2 = 100:50:8	10	
CO:O_2:CO_2 = 100:50:16	10, 30	
CO:O_2:CO_2 = 100:50:21	10, 30	
CO:O_2:CO_2 = 100:50:32	10	
CO:O_2:CO_2 = 100:54:10	10, 30	
CO:O_2:CO_2 = 100:20:11	10, 30	
CO:O_2:CO_2 = 100:11:20	10, 30	
CO:O_2:CO_2 = 100:10:23	10, 30	
CO:N_2:CO_2 = 100:50:20	10, 30	
CO:O_2:N_2:CO_2 = 100:50:25:32	10, 30	
H_2O:CO:O_2:N_2:CO_2 = 1:50:35:15:3	10	
H_2O:CO:O_2:N_2:CO_2 = 1:25:25:10:13	10	

REFERENCES.—(1) Ehrenfreund et al. 1997; (2) Leiden Observatory Laboratory database; (3) Ehrenfreund et al. 1998.

CHAPTER 6
DETECTION OF ABUNDANT CO_2 ICE IN THE QUIESCENT CLOUD MEDIUM TOWARD ELIAS 16⋆

"Life is full of infinite absurdities, which, strangely enough, do not even need to appear plausible, since they are true."

Luigi Pirandello, *Six Characters in Search of an Author*

In this chapter, I report the first detection of solid carbon dioxide (CO_2) in quiescent regions of a dark cloud in the solar neighborhood, a result that has important implications for models of ice formation and evolution in the interstellar medium. The K-type field star Elias 16 was previously known to display solid-state absorption features of H_2O and CO ices arising in the Taurus Dark Cloud. This detection of the CO_2 feature at 4.27 μm in this line of sight implies a column density $N_{CO_2} = 4.6^{+1.3}_{-0.6} \times 10^{17}\,\mathrm{cm}^{-2}$, equivalent to $\sim 18\,\%$ and $70\,\%$ of the H_2O and CO column densities, respectively. Comparison with laboratory data indicates that (unlike CO) the CO_2 resides primarily in a polar (H_2O-rich) component of the ices. CO_2 is formed easily in the laboratory by the photolysis of ice mixtures containing CO, but the detection toward Elias 16 indicates that CO_2 formation can occur in dark clouds in the absence of a local embedded source of radiation. Possible alternative mechanisms for CO_2 production include grain surface reactions and energetic processing driven by the interstellar radiation field or cosmic rays.

In § 6.2, I discuss the specifics of the data reduction involved in this observation and present the final data. The data are analyzed in § 6.3, and laboratory spectra are used to match the profile of the 4.27 μm CO_2 absorption feature. Finally, the implications of the results on astrochemistry are discussed in § 6.4.

⋆The results presented in this chapter have been published in modified form by Whittet et al. (1998).

6.1 Introduction

Icy mantles are an important component of the interstellar dust in molecular clouds (see Ch. 1; see also Chiar 1997 and Whittet 1997 for recent reviews). Observations show that typically, some 10 % of the elemental oxygen is locked up in solid H_2O, comparable to that in gas-phase CO.

The fact that CO_2 is produced easily in the laboratory by UV irradiation of ices containing CO and H_2O (d'Hendecourt et al. 1986; Sandford et al. 1988) suggests that the CO_2 abundance in interstellar ices might measure the degree of UV photolysis. Observations are hindered by the fact that strong CO_2 absorption in the Earth's atmosphere precludes detection from ground-based or suborbital platforms. Studies of the CO_2 bending mode at 15.2 μm with the low-resolution spectrometer on board the Infrared Astronomical Satellite (IRAS) provided conflicting results (d'Hendecourt & Jourdain de Muizon 1989; Whittet & Walker 1991), and convincing detection of both stretching and bending modes had to await the launch of ISO in 1995 (e.g., d'Hendecourt et al. 1996; Gürtler et al. 1996). The abundance of solid CO_2 typically exceeds that of gas-phase CO_2 by factors of $\sim$ 20–100 (van Dishoeck et al. 1996), in keeping with chemical models that predict low CO_2 production efficiency via gas-phase reactions (e.g., Herbst & Leung 1986). Solid CO_2 detections reported to date are almost exclusively toward "protostellar" objects embedded in molecular clouds, in which the ices may be at least partially processed by radiation from the source itself, consistent with the hypothesis that CO_2 is the product of photolysis. Confirmation would require the *non-detection* of CO_2 in a line of sight remote from sources of UV radiation.

The Galactic Center source Sgr A* might be considered a test case. It shows solid-state absorption features arising in both dense and diffuse clouds along the line of sight (e.g., Lutz et al. 1996). The detection of solid CO_2 toward Sgr A* (Lutz et al. 1996; this work, Ch. 7) hints that the presence of an embedded source may not be a prerequisite for CO_2 formation; however, interpretation is complicated because multiple clouds along the line of sight contribute to the observed solid-state features, and the environment of the CO_2 is thus unknown. Since much of the total visual extinction ($A_V \approx 30$ mag) in the line of sight is thought to arise in diffuse

clouds that lack solid CO_2 (Sandford et al. 1991; Whittet et al. 1997), the denser CO_2 clouds must have modest extinctions ($A_V \lesssim 10$ mag) and may be translucent, in which case they do not provide a good diagnostic of CO_2 as a tracer of photolysis.

Field stars located serendipitously behind dense molecular material provide an invaluable resource for probing the properties of icy mantles in quiescent regions of molecular clouds in the solar neighborhood, since these lines of sight are generally remote from embedded stars that might affect the local environment (Whittet, Longmore, & McFadzean 1985; Whittet et al. 1983, 1988, 1989; Kerr, Adamson, & Whittet 1993; Smith, Sellgren, & Brooke 1993; Chiar et al. 1994, 1995). Elias 16, in particular, has been adopted as a standard for the quiescent cloud medium. This source, a K 1 III star hidden by some 21 mag of visual extinction, was first detected and classified in a near-IR survey of the Taurus Dark Cloud by Elias (1978b). It is known with some confidence that the grain mantles toward Elias 16 have not been thermally or radiatively processed by an embedded source: this is indicated by (i) the shape of the 3.0 μm H_2O ice feature, consistent with a lack of annealing (Smith, Sellgren, & Tokunaga 1989); (ii) the presence of abundant solid CO in nonpolar form (Chiar et al. 1995), requiring grain temperatures below 20 K; and (iii) the absence of 4.62 μm absorption, associated with CN-bearing molecules thought to be produced by irradiation of primary ices containing nitrogen (Tegler et al. 1995). Elias 16 is thus the ideal test case for the link between CO_2 production and photolysis.

6.2 Observations and Results

Elias 16 was observed by ISO with the SWS on October 1, 1997, during day 686 of the mission. A difficulty encountered while preparing for these observations was the fact that the position of Elias 16 was previously not known with sufficient precision: since it is not possible to "peak up" on a source prior to observation with the SWS, positions better that $\pm 2''$ are required to ensure maximum sensitivity, whereas the original position of Elias 16 (Elias 1978b) has quoted errors of $\pm 5''$. The source lacks a counterpart on Palomar Observatory Sky Survey prints, precluding the determination of an optical position. Improved coordinates were determined

from the mean of eight peak-up positions in the near IR, extracted from the data archive of the UK Infrared Telescope at Mauna Kea Observatory:

$$\text{R.A.} = 04^{\text{h}}\,36^{\text{m}}\,34\overset{\text{s}}{.}4,\ \text{decl.} = +26^\circ\,05'\,36''\quad (1950).$$

This position is considered accurate to $\pm 1''$; it agrees very well with the original Elias (1978b) position, which we deduce to have conservative nominal errors.

The SWS, described in Ch. 5 and in more detail by de Graauw et al. (1996), was used to observe Elias 16 in observing mode SWS06, covering the wavelength ranges 2.6–3.5, 4.0–4.5, and 4.6–5.3 μm[10] at mean resolving power $\lambda/\Delta\lambda \approx 1800$. The total on-target time was 8894 s.

The final spectrum is plotted in Fig. 6.1 and compared with the ground-based observations from Whittet et al. (1983, 1985). The data were reduced using the SWS Interactive Analysis package (de Graauw et al. 1996) and the latest version of the RSRF (Schaeidt et al. 1996) as described in § 5.2. Dark current variations can be especially troublesome for a source as faint as Elias 16 (relative to other SWS targets) in band 2A. Preliminary reductions suggested that too much dark current is subtracted by the standard product pipeline, resulting in low apparent flux levels in the band 2A continuum compared with those in band 1 and the ground-based data. A correction offset of 0.35 μV s^{-1} was applied before dividing by the RSRF and applying gain correction factors to give absolute flux calibration. Agreement between the final SWS spectrum and ground-based data is excellent where they overlap in the 2.9–3.5 and 4.6–4.8 μm regions (Fig. 6.1), and the continuum level in the 4.0–4.5 μm region is consistent with an interpolation of the ground-based to within 10 %. Satisfactory agreement was found between the up and down scans, appreciable deviations occurring only in the trough of the deep 4.27 μm feature (where the signal-to-noise ratio is lowest) and in the adjacent short-wavelength continuum at 4.18–4.22 μm. The apparent shallow "emission wing" near 4.2 μm is probably not real. Other details of the spectrum, notably weak, narrow features at 4.295, 4.352, and 4.393 μm (see Fig. 6.2), do appear to be real, and are identified with

[10]Data were obtained serendipitously in the 14–19 μm region but are of poor quality because of the faintness of the object at these wavelengths; regrettably, this precludes the detection of the CO_2 bending mode near 15 μm.

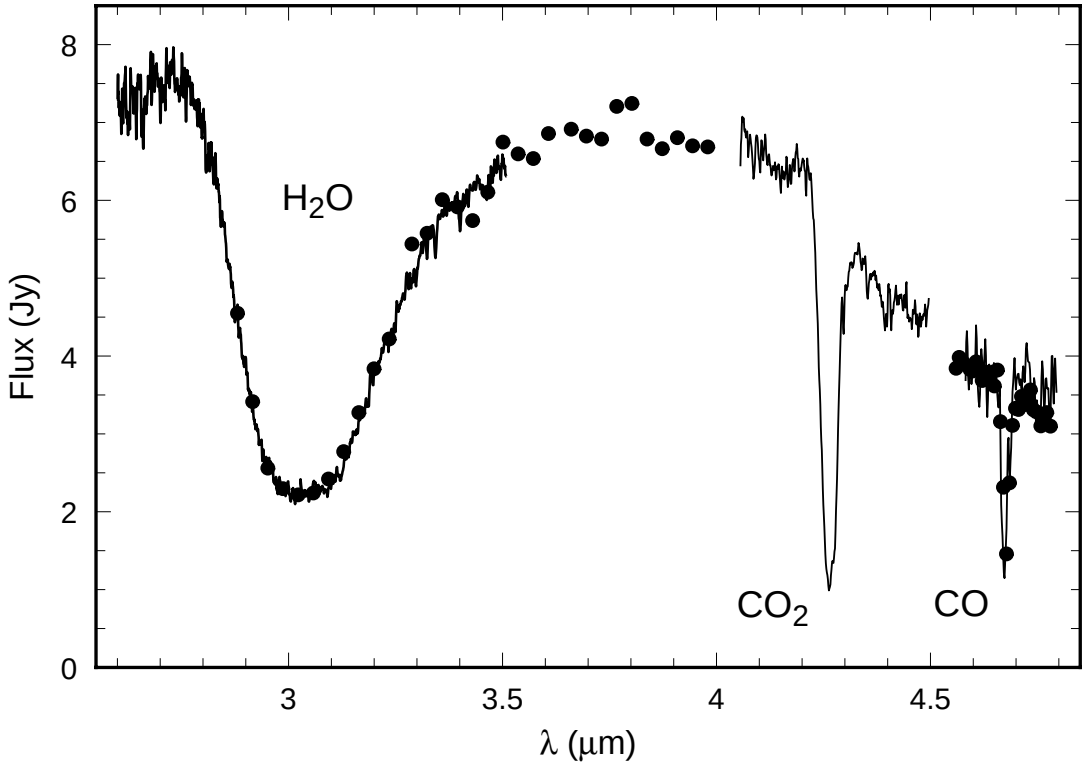

Figure 6.1: Superposition of the SWS and ground-based spectra of Elias 16 in the 2.6–4.8 μm region: SWS data (solid curves); ground-based data (filled circles) in the 2.9–4.0 and 4.6–4.8 μm windows (Whittet et al. 1983, 1985). Features due to H_2O, CO_2, and CO ices are labeled.

photospheric CO lines in the K 1 III star. The 4.393 μm line may be blended with a broader, shallower feature at 4.39 μm associated with the stretching mode of solid $^{13}CO_2$.

6.3 Analysis

The spectrum in Fig. 6.1 contains a deep feature corresponding to the C=O stretching mode of solid CO_2 at 4.27 μm, in addition to previously known features at 3.0 and 4.67 μm identified with H_2O and CO. An optical depth plot centered on the 4.27 μm feature is shown in Fig. 6.2, deduced by assuming that the 4.05–4.18 and 4.35–4.45 μm regions represent the continuum (ignoring narrow features). The peak optical depth in the CO_2 feature is estimated to be $\tau_{4.27} = 1.7^{+0.5}_{-0.2}$. The

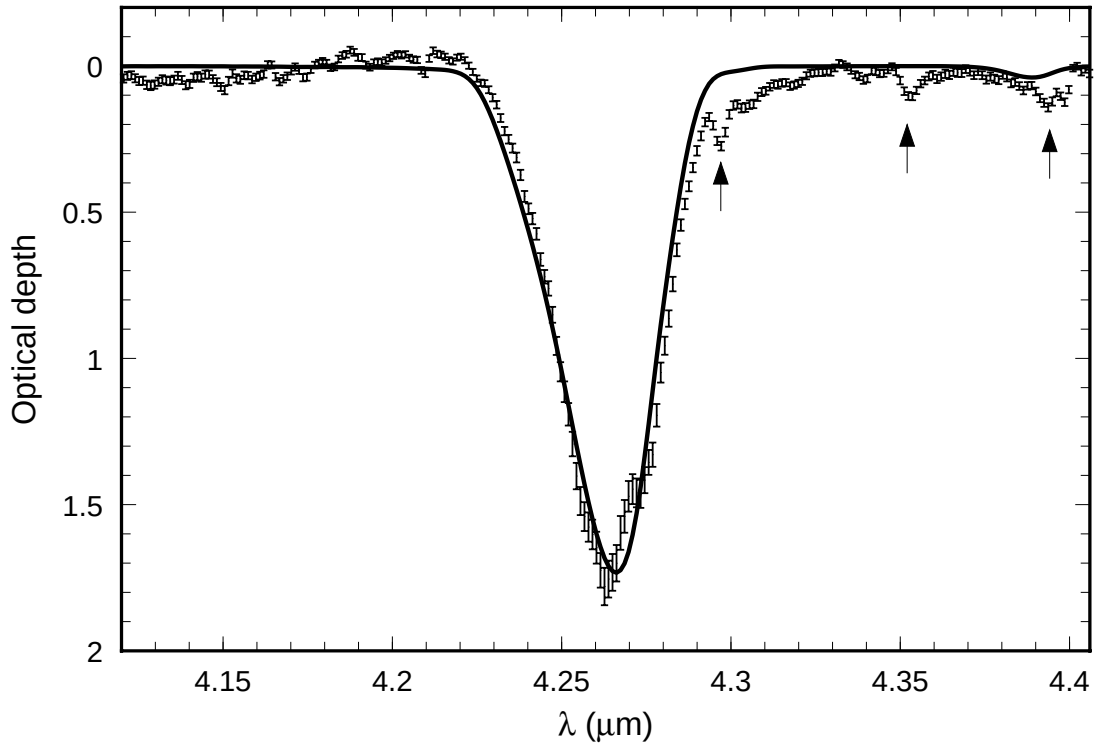

Figure 6.2: Optical depth plot (points with errorbars) deduced from the SWS data in the region of the CO_2 stretching mode. Arrows indicate the positions of photospheric CO lines in the K 1 III star. The solid curve is the best-fitting laboratory ice mixture (H_2O:CO_2:CO = 100:20:3 at 20 K).

asymmetric uncertainty allows for possible systematic error in vertical placement as well as random noise.

Fits to the feature were attempted using the laboratory ice analogs containing CO_2 (see § 5.3; the laboratory mixtures from Ehrenfreund et al. 1996, 1997 used here are listed in Table 5.1) and a χ^2 minimization routine (e.g., Kerr, Adamson, & Whittet 1993; Chiar et al. 1995; see § 5.3.3). Both polar and nonpolar ice mixtures containing CO_2 are included in the set of analog spectra, and the routine may select an individual mixture or any pair of polar and nonpolar mixtures. Grain shapes following a continuous distribution of ellipsoids in the small particle limit were assumed in the calculations (see § 5.3.2; Ehrenfreund et al. 1997). The best fit to the profile (Fig. 6.2, solid line) is obtained with a single polar ice composed

of H_2O:CO_2:CO = 100:20:3 at 20 K. A number of similar mixtures give fits that are not substantially worse than that shown, but no combination with a significant nonpolar component is capable of giving a satisfactory fit. The conclusion that the feature is dominated by an H_2O-rich polar ice at low temperature ($\lesssim 20$ K) therefore appears to be robust.

The column density of solid CO_2 is calculated from Eq. (2.4). We adopt a strength of $A = 7.6 \times 10^{-17}$ cm molec^{-1} for the CO_2 4.27 μm stretching mode, a value only weakly dependent on the composition of the matrix containing the CO_2 (see Ch. 3). The resulting column density toward Elias 16 is $N_{CO_2} = 4.6^{+1.3}_{-0.6} \times 10^{17}$ cm^{-2}. For comparison, the 3.0 and 4.67 μm features lead to column densities of 25 and 6.5×10^{17} cm^{-2} for H_2O and CO ices, respectively (Chiar et al. 1995). Hence, the CO_2 abundance is ~ 18 % relative to the H_2O abundance, consistent with the composition of the best-fitting mixture. Overall abundances of solid CO and CO_2 are comparable in Elias 16 ($N_{CO_2}/N_{CO} = 0.71$), but the CO resides predominantly in nonpolar ices (Chiar et al. 1995) and must therefore be segregated from the CO_2. The CO_2/CO ratio in the polar component alone is ~ 6.

6.4 Discussion

In general, three processes are thought to play important roles in the formation and evolution of interstellar ice mantles: (i) grain surface reactions, (ii) energetic processing by UV photolysis or particle bombardment, and (iii) thermal processing that leads to sublimation, segregation, and/or annealing. Of these, processes (i) and (ii) are the most probable sources of CO_2 in grain mantles, with process (ii) highly favored in the literature on the topic in the last 10 years (see § 1.3). An important implication of this detection is that *the presence of CO_2 in grain mantles does not require the presence of an embedded source of luminosity.* CO_2 can evidently be produced in other ways, perhaps by grain surface reactions, or by energetic processing driven by penetrating UV photons of the ISRF or cosmic rays rather than any local embedded source.

Within the context of a surface chemistry model, accreted CO reacts with accreted O to form CO_2. This reaction possesses an activation energy barrier (Grim

& d'Hendecourt 1986). However, at interstellar densities, grain surface chemistry is in the diffusion limit rather than in the reaction limit (see e.g., Tielens & Whittet 1997 and references therein), unlike the typical laboratory situation (§ 1.3). The long timescales ($\simeq 1$ day) between successive accretion events may allow the reaction to proceed: i.e., an accreted O atom has a day to react with any CO present before the accretion of another atom (O or H) with which it may react. Moreover, the estimated time for an O atom to sample the entire grain surface is quite small in comparison ($\sim 10^{-2}$ s; Tielens & Allamandola 1987). Theoretical studies have shown that it may be possible to form appreciable quantities of CO_2 ($\sim 10\,\%$) in this way (Tielens & Hagen 1982).

It was noted (§ 6.3) that CO_2 toward Elias 16 resides in a polar (H_2O-rich) mantle, whereas CO resides almost entirely in a nonpolar (H_2O-poor) mantle. In the surface chemistry scheme, CO_2 must therefore form simultaneously with H_2O in an environment where a significant abundance of atomic H is present in the accreting gas. The nonpolar mantle is presumed to arise in a different (denser) environment with very low gas-phase H and O abundances, leading to ices dominated by accreted CO and O_2 and containing very little CO_2 in the absence of an energy source. A problem faced by the surface chemistry model is the requirement to form CO_2 in a situation where hydrogenation is important (to form H_2O), yet CO is preferentially oxidized to CO_2 rather that hydrogenated to methanol.[11] The accretion of O, O_2, and CO in the presence of abundant atomic H ensures efficient H_2O formation (via hydrogenation of O_2 or O_3, where the latter is formed by the reaction of O with O_2), while CO must be inhibited from reaction with H to form CH_3OH. The barrier for the reaction of H with O_3 is indeed less than that for the reaction of H with CO (450 K compared with 1000 K; Tielens & Hagen 1982). However, the probability of the reaction that forms O_3 relative to the reaction that forms CO_2 is presently uncertain, and this precludes a detailed quantitative evaluation of the chemistry scheme. Further progress is dependent on new laboratory measurements.

Finally, energetic processing is reconsidered as a possible source of CO_2 in *quiescent* clouds. In this scenario, CO_2 forms by the reaction of CO with atomic

[11] The abundance of CH_3OH was found to be no more than 3 % of the H_2O abundance in ices toward Elias 16 (Chiar, Adamson, & Whittet 1996).

oxygen liberated by the dissociation of other molecules (primarily H_2O and O_2 in the polar and nonpolar mantles, respectively). It is important to note that CO_2 is also dissociated back to CO by energetic processing: thus, CO $\rightarrow$ CO_2 conversion is never complete. The energy sources available are the ISRF (Mathis, Metzger, & Panagia 1983), attenuated by dust in the cloud itself, and cosmic rays; the latter may contribute to CO_2 production either directly, by ion bombardment of the ices (Palumbo & Strazzulla 1993), or indirectly, by the generation of a UV radiation field through the liberation of energetic secondary electrons that excite H_2 (Prasad & Tarafdar 1983; Sternberg, Dalgarno, & Lepp 1987).

Information on some UV-photolyzed laboratory ices is available from the Leiden database.[12] As a basis for discussion, a polar laboratory mixture with an initial composition of H_2O:CO = 100:30 reaches a CO_2/CO ratio of 2.1 after exposure for 3 hr to $\sim$ 6 eV radiation of flux $10^{15}\,\mathrm{cm^{-2}\ s^{-1}}$. Equilibrium is not established at this stage, and a simple extrapolation suggests that the observed CO_2/CO ratio of $\sim$ 6 in polar ices toward Elias 16 (§ 6.3) might be reached in $\sim 3 \times 10^4$ s, i.e., after an exposure of $\sim 3 \times 10^{19}$ photons $\mathrm{cm^{-2}}$. The cosmic-ray–induced UV flux in a molecular cloud amounts to $\sim 10^3\,\mathrm{cm^{-2}\ s^{-1}}$ (Prasad & Tarafdar 1983): the time to reach an exposure of $10^{19}\,\mathrm{photons\,cm^{-2}}$ is thus $\sim 10^9$ yr, which exceeds typical cloud lifetimes, and therefore photolysis via this route alone is probably insufficient to account for the abundance of CO_2 in polar ices. In contrast, the ISRF flux is $\sim 8 \times 10^7\,\mathrm{cm^{-2}\ s^{-1}}$ at the cloud surface (Mathis, Metzger, & Panagia 1983), attenuated to $\sim 3 \times 10^4\,\mathrm{cm^{-2}\ s^{-1}}$ at $A_V = 5$ mag (assuming $A_{UV}/A_V = 1.6$). Thus, the required level is reached in $\sim 3 \times 10^7$ yr at $A_V = 5$, comparable to cloud lifetimes. This result is not necessarily in conflict with the observed total line-of-sight extinction ($A_V \approx 21$) to Elias 16, since at any location along the path, the extinction *to the cloud edge* is never more than half this value; moreover, filamentary structure and clumpiness within the cloud will tend to enhance intra-cloud penetration of the ISRF relative to that in a homogeneous cloud.

The dearth of CO_2 in the nonpolar component of the ices seems consistent with production by photolysis that is driven by penetrating UV photons. Solid CO,

[12]See the ice analogs database at `http://www.strw.leidenuniv.nl/~lab/`, which is maintained by the Laboratory Astrophysics group of Leiden Observatory.

the primary tracer of the nonpolar component, is detected only at optical depths equivalent to $A_V \gtrsim 5\,\mathrm{mag}$ (Whittet et al. 1989; Chiar et al. 1995). Thus the segregation of CO and CO_2 might arise naturally as a result of physical conditions, as a function of shielding from the external radiation field at different optical depths into the cloud. However, if CO_2 is indeed produced by UV photolysis, it is somewhat surprising that the $4.62\,\mu$m "XCN" feature, normally considered an indicator of energetic processing of grain mantles, is absent in Elias 16 (Tegler et al. 1995). Perhaps the pre-irradiation ices contain little NH_3, which may be an essential ingredient for the formation of XCN (Grim et al. 1989).

The detection of CO_2 in ice mantles toward Elias 16 clearly presents a challenge to existing models of ice formation and evolution in molecular clouds. Both surface chemistry and photolysis schemes for CO_2 production require further investigation to determine which is the most important source of CO_2 in quiescent regions of the ISM.

CHAPTER 7
ISO-SWS OBSERVATIONS OF SOLID CO_2 IN MOLECULAR CLOUDS*

> "Facts quite often, I fear to confess, like lawyers, put me to sleep at noon. Not theories, however. Theories are invigorating and tonic. Give me an ounce of fact and I will produce you a ton of theory by tea this afternoon. That is, after all, my job. And, come to think of it, the business of men."
>
> Ray Bradbury, in the foreword to *Mars and the Mind of Man*

ISO-SWS spectra of interstellar CO_2 ice absorption features at a resolving power $\lambda/\Delta\lambda \approx$ 1500–2000 are presented for 13 lines of sight. Spectral coverage includes the primary stretching mode of CO_2 near 4.27 μm in all sources; the bending mode near 15.2 μm is also detected in 12 of them. The selected sources include massive protostars (Elias 29 [in ρ Oph], GL 490, GL 2136, GL 2591, GL 4176, NGC 7538 IRS1, NGC 7538 IRS9, S 140, W3 IRS5, and W33 A), and sources associated with the Galactic Center (Sgr A*, GCS 3 I, and GCS 4). Results are compared to those from Ch. 6 for Elias 16, a background star behind a quiescent dark cloud in Taurus. These sight-lines probe a diverse range of environments, but measured column densities of interstellar CO_2 ice fall in the range of 10 to 23 % relative to H_2O ice: this ratio displays remarkably little variation for such a physically diverse sample. Comparison of the observed profiles with laboratory data for CO_2-bearing ice mixtures (from § 5.3) indicates that CO_2 generally exists in (at least) two phases, one polar (H_2O-dominant) and one nonpolar (CO_2-dominant). The observed CO_2 profiles may also be reproduced when the nonpolar components are replaced with thermally-annealed ices. Formation and evolutionary scenarios for CO_2 and implications for grain mantle chemistry are discussed. Results support the conclusion that

*The results presented in this chapter have been published in modified form by Gerakines et al. (1998).

thermal annealing, rather than energetic processing due to UV photons or cosmic rays, dominates the evolution of CO_2-bearing ices.

§ 7.2 contains a description of the methods used to derive the spectra. In § 7.3, the observed features are presented, analyzed through the use of laboratory spectra, and the derived CO_2 abundances are compared with those of other known components of icy grain mantles. Finally, the implications for grain mantle chemistry in the ISM are discussed in § 7.4.

7.1 Introduction

The evolution of carbonaceous material in the ISM is a key problem in astrophysics, with ramifications as far-reaching as the origins of life on Earth. To date, nearly 100 carbon-bearing species are known to exist in the gas-phase of the ISM, most abundantly in the form of carbon monoxide, CO (see reviews by Snyder 1997 and van Dishoeck & Blake 1998). Of these species, a handful have been detected in the solid state as constituents of icy grain mantles through IR spectroscopy (§ 1.3). Before the launch of ISO, detections were limited to molecules with transitions in spectral regions free of significant atmospheric absorption. A full inventory of interstellar ices accessible to IR observation is now possible, and one of the early highlights in reaching this goal has been carbon dioxide, CO_2 (e.g., Gürtler et al. 1996, this work, Ch. 6).

Carbon dioxide has several possible formation mechanisms in the ISM. While formation rates for CO_2 are low in the gas phase (Herbst & Leung 1989; Millar et al. 1991), laboratory experiments show that CO_2 is formed with extreme efficiency in irradiation experiments involving solid H_2O and CO (see e.g., d'Hendecourt, Allamandola, & Greenberg 1985; Sandford & Allamandola 1990; Moore, Khanna, & Donn 1991). Thus, large amounts of CO_2 are predicted near luminous protostars with strong ultraviolet (UV) fields. Computational models which include grain surface chemistry (Tielens & Hagen 1982; d'Hendecourt, Allamandola, & Greenberg 1985; Hasegawa & Herbst 1993; Shalabiea & Greenberg 1994) also predict that CO_2 should be present in interstellar icy grain mantles, where the abundance of CO_2 produced is strongly dependent on whether the grain-surface oxidation of CO is

possible. The laboratory results of Grim & d'Hendecourt (1986) indicate that this reaction may have an activation energy of 10 to 30 K, but such a barrier may be easily overcome in the ISM given the long timescales for diffusion-limited grain surface reactions (accretion rate $\sim$ 1 species per day; Tielens & Whittet 1997). Moreover, the observation of abundant CO_2 in the quiescent ISM toward Elias 16 strongly suggests that processing of mantle ices due to embedded sources of radiation is not required to produce interstellar CO_2 (Ch. 6).

Infrared spectra of CO_2-bearing ices have been well-studied in the laboratory in an astrophysical context by Sandford & Allamandola (1990), Ehrenfreund et al. (1997), and in this work, Ch. 3. CO_2 has four observable absorptions in the mid IR (two combination modes, one stretching mode and one bending mode), the strongest of which is due to its asymmetric stretching fundamental vibration (ν_3) at 4.27 μm (2342 cm^{-1}): its strength is $A = 7.6 \times 10^{-17}$ cm molec^{-1}, which may be compared with the values for the H_2O and CO stretching modes, $A = 2.0 \times 10^{-16}$ and 1.1×10^{-17} cm molec^{-1}, respectively (see e.g., Ch. 3). This transition is strong enough to be observable even when the C atom is replaced by its isotope ^{13}C (terrestrially, 89 times less abundant than ^{12}C). The asymmetric stretching mode of $^{13}CO_2$ is located at 4.38 μm (2283 cm^{-1}). The symmetric stretching mode (ν_1) of CO_2 at 7.2 μm (1385 cm^{-1}) is normally unobservable since it produces no change in the molecule's dipole moment. The bending mode (ν_2) absorbs at a wavelength of 15.2 μm (660 cm^{-1}) and is 7 times weaker than the asymmetric stretching mode ($A = 1.1 \times 10^{-17}$ cm molec^{-1}; Ch. 3). The $\nu_1+\nu_3$ and $2\nu_2+\nu_3$ combination modes, located at 2.697 and 2.778 μm (3708 and 3600 cm^{-1}), are 54 and 170 times weaker than the stretching mode, respectively.

The sensitivity of CO_2 IR features to ice composition and temperature makes them ideal probes of interstellar cloud parameters. CO_2 is less volatile than CO and may exist in solid form up to temperatures of 50 to 90 K, depending on the ice in which it resides. It could therefore provide information on carbon chemistry in a wider range of environments than CO, which will sublime almost completely at temperatures above 30 K (although a small amount may exist at higher temperatures when trapped in some ice mixtures). The profiles of CO_2 features in polar ice

mixtures (dominated by H_2O or CH_3OH) are dramatically different from those of CO_2 in nonpolar environments (dominated by molecules such as CO, O_2, or CO_2 itself) and thereby trace the chemical composition of interstellar ices (Sandford & Allamandola 1990; Ehrenfreund et al. 1997). Temperature history is also preserved in the structure of the 15.2 μm CO_2 bending mode, whose profile contains a complicated substructure when annealed (Ehrenfreund et al. 1998).

7.2 Data Reduction

ISO, the SWS instrument, and the general data reduction techniques of ISO-SWS data have been described previously in Ch. 5. Here I describe the specifics of the data reduction in the regions of the CO_2 absorption features. Details of these observations are listed in Table 7.1. Data presented in Figs. 7.1–7.4 were obtained in both AOTs SWS01 and SWS06 in instrument bands 2A ($\lambda = 4.08$–$5.3\,\mu$m) and 3A ($\lambda = 12.0$–$16.5\,\mu$m). The SWS observing modes and integration times for each observation are listed in Table 7.1. The full spectral resolution in SWS bands 2A and 3A are $\lambda/\Delta\lambda \approx 1800$ and 2000, and therefore the observations carried out with AOT SWS01 speeds 3 and 4 correspond to $\lambda/\Delta\lambda \sim 500$ and 1000, respectively.

As described previously in § 5.2, effects of fringing due to the oscillatory nature of the SWS RSRFs were minimized using an interactive routine which applied small wavelength shifts to the responsivity curves before the division. In most cases, however, some small amount of fringing did remain in the spectra. If reliable analyses were still possible, this residual fringing was not removed since attempts to do so (such as clipping high-frequency components from the Fourier transform) slightly alter the shape of existing absorptions. However, the 15.2 μm spectra of NGC 7538 IRS1, GL 4176, and GL 2591 did require this procedure to remove enough of the fringing to properly analyze them. One artifact appears in all spectra at 14.5 μm (a quasi-absorption feature with an optical depth of about 0.05; it is prominent in the spectra of GCS 4, GL 2591, GL 490, and Sgr A*, see Figs. 7.1–7.5). Its central wavelength corresponds to a discontinuity present in the RSRF, and therefore its removal is quite difficult (see Fig. 5.6 of the SWS Observer's Manual).

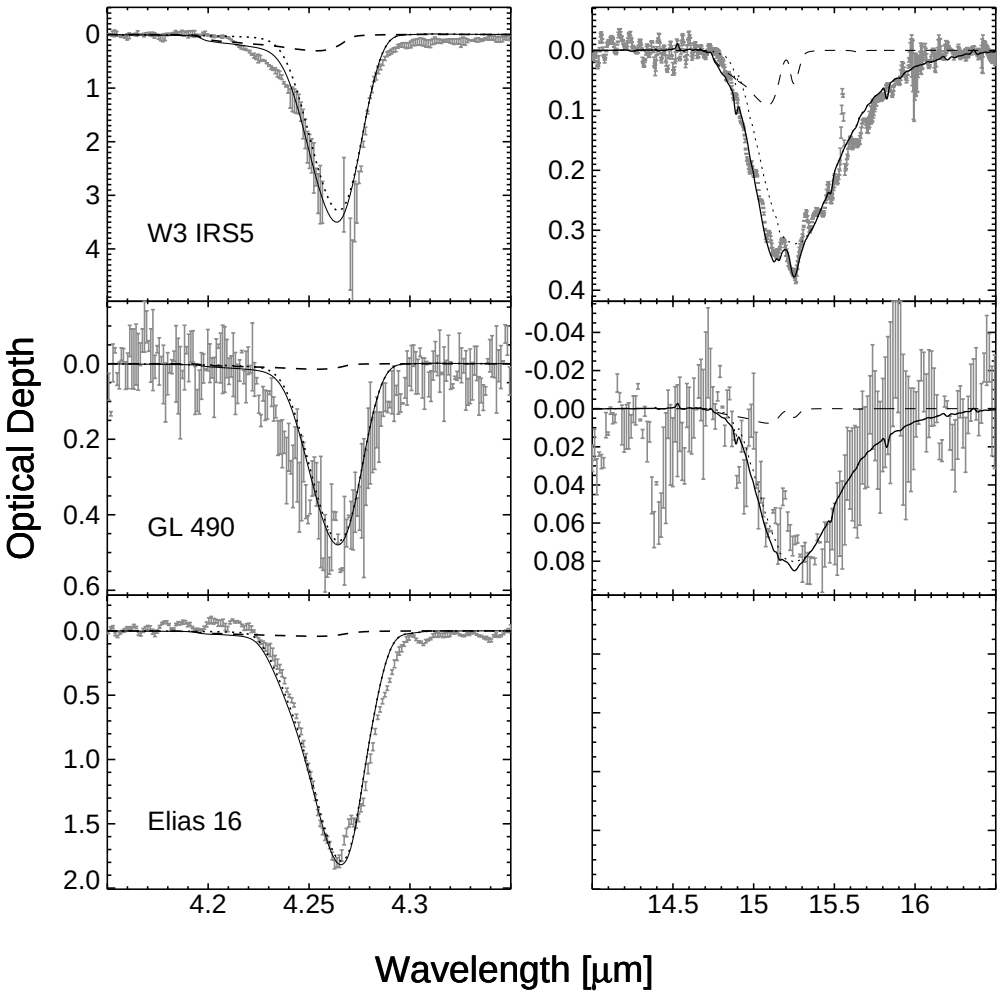

Figure 7.1: Observed stretching modes (left) and bending modes (right) toward W3 IRS5, GL 490, and Elias 16. The stretching mode of W3 IRS5 is saturated and points with S/N < 1 have been omitted. Spurious structure exists in the stretching mode of Elias 16 due to low flux levels. Absorptions near 14.5 μm are due to a feature present in the RSRF (§7.2). Dotted lines– polar components of lab fits; dashed lines– nonpolar components; solid lines– sum of polar and nonpolar components.

Table 7.1: Observing parameters for sources in CO_2 program.

Source	Position (J2000) R.A.	Dec.	Date	Rev	AOT	Δt_{int} [s]
W3 IRS5	$02^h25^m40^s.8$	$62°05'52''$	1997 Jan 17	427	1.3	3454
			1997 Jan 17	427	6	5668
GL 490	03 27 38.7	58 47 01	1997 Aug 17	640	1.3	3454
			1998 Mar 27	863	6	4354
Elias 16	04 39 38.9	26 11 27	1997 Oct 1	686	6	8894
GL 4176	13 43 02.1	−62 08 52	1996 Mar 13	117	6	1706
			1996 Sep 18	306	6	4268
Elias 29	16 27 09.3	−24 37 21	1996 Aug 9	267	1.3	3454
			1996 Sep 3	292	6	5668
Sgr A*	17 45 40.0	−29 00 28	1996 Feb 19	94	1.4	6528
GCS 3 I	17 46 14.9	−28 49 34	1996 Oct 8	327	6	3226
GCS 4	17 46 15.6	−28 49 47	1996 Sep 9	297	1.3	3454
W33 A	18 14 39.4	−17 52 01	1996 Oct 10	329	1.4	6538
			1997 Feb 25	467	6	6282
GL 2136	18 22 26.3	−13 30 08	1996 Mar 16	120	6	2994
			1996 Sep 23	311	6	4391
GL 2591	20 29 24.7	40 11 19	1996 May 28	193	6	3590
S 140	22 19 18.1	63 18 47	1996 Jun 24	220	1.4	6538
			1996 Aug 6	263	6	5270
NGC 7538 IRS1	23 13 45.3	61 28 10	1996 Aug 25	283	6	4552
			1996 Dec 6	385	1.3	3454
NGC 7538 IRS9	23 14 01.6	61 27 20	1996 Feb 23	98	6	6894
			1996 Feb 23	98	1.2	1816

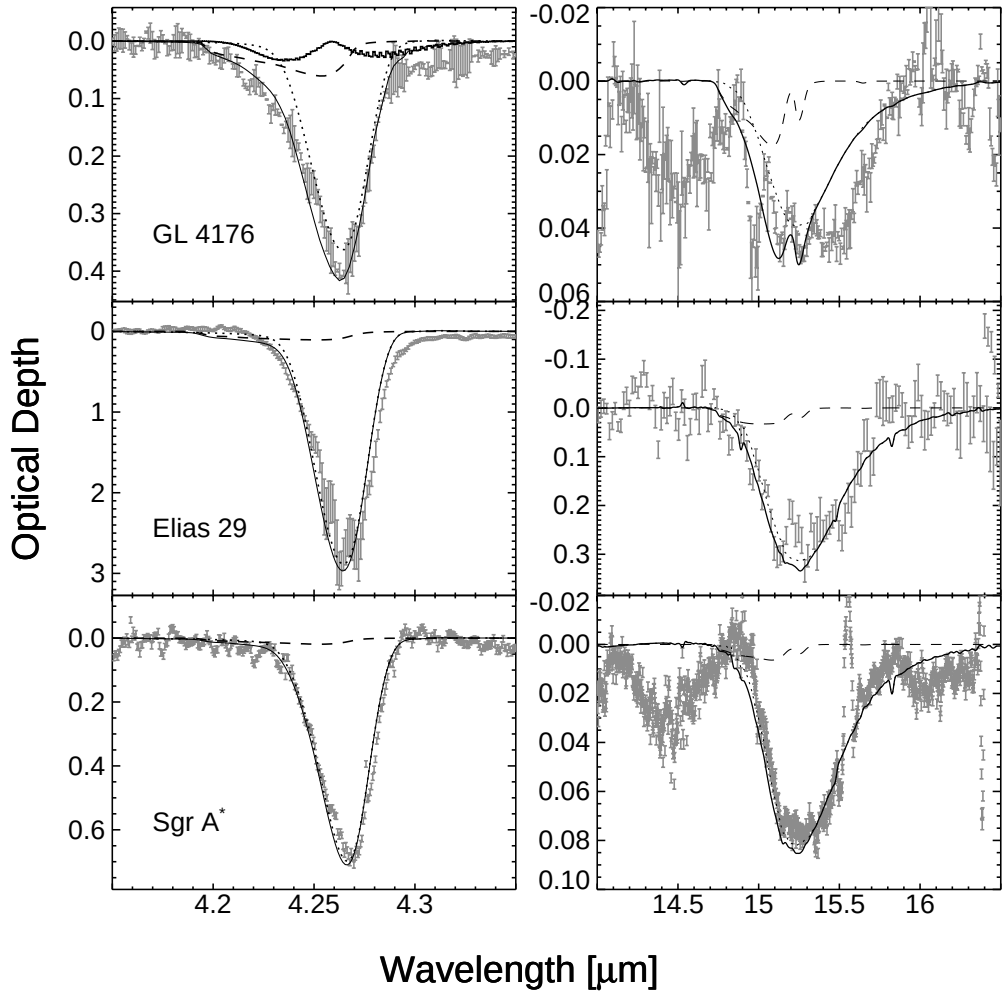

Figure 7.2: Interstellar CO_2 spectra presented as in Fig. 7.1, but for GL 4176, Elias 29, and Sgr A*. Gas-phase absorption at 4.27 μm has been estimated for GL 4176 using the 14.97 μm gas feature. Spurious structure exists in the trough of the Elias 29 stretching mode. The 15.2 μm spectrum of Sgr A* contains as emission feature at 15.55 μm due to fine-structure lines of [Ne III].

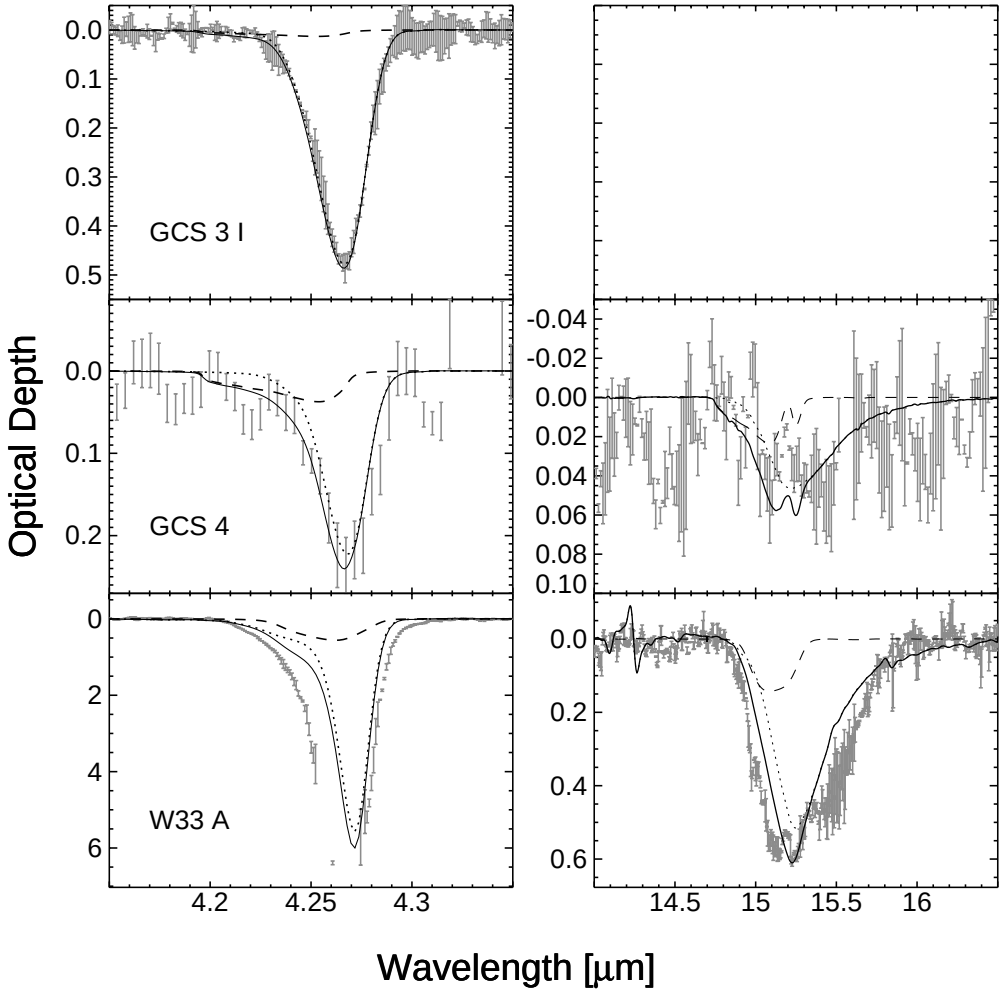

Figure 7.3: Interstellar CO_2 spectra presented as in Figs. 7.1 and 7.2, but for GCS 3 I, GCS 4, and W33 A. The stretching mode of W33 A is saturated and points with S/N < 1 have been omitted.

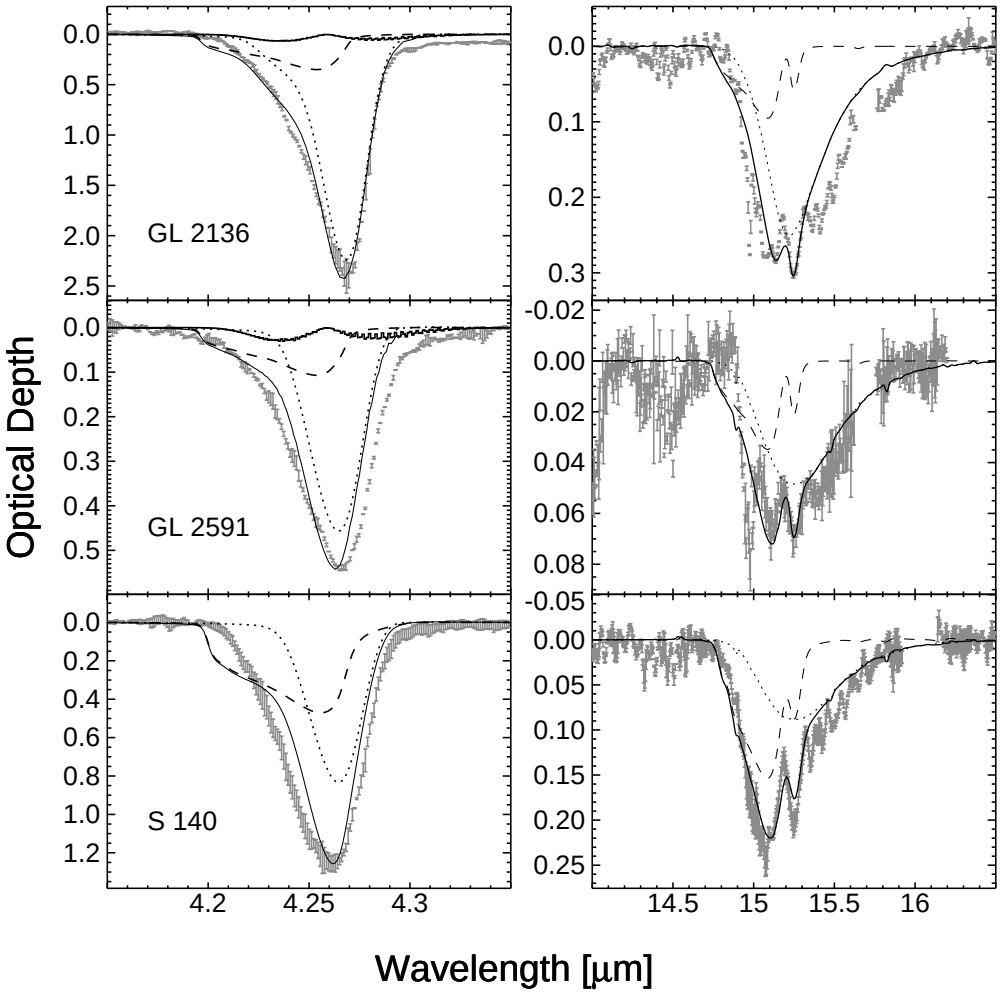

Figure 7.4: Interstellar CO_2 spectra presented as in Figs. 7.1–7.3, but for GL 2136, GL 2591, and S 140. Gas-phase absorptions at 4.27 μm have been estimated for GL 2136 and GL 2591 using the 14.97 μm gas features.

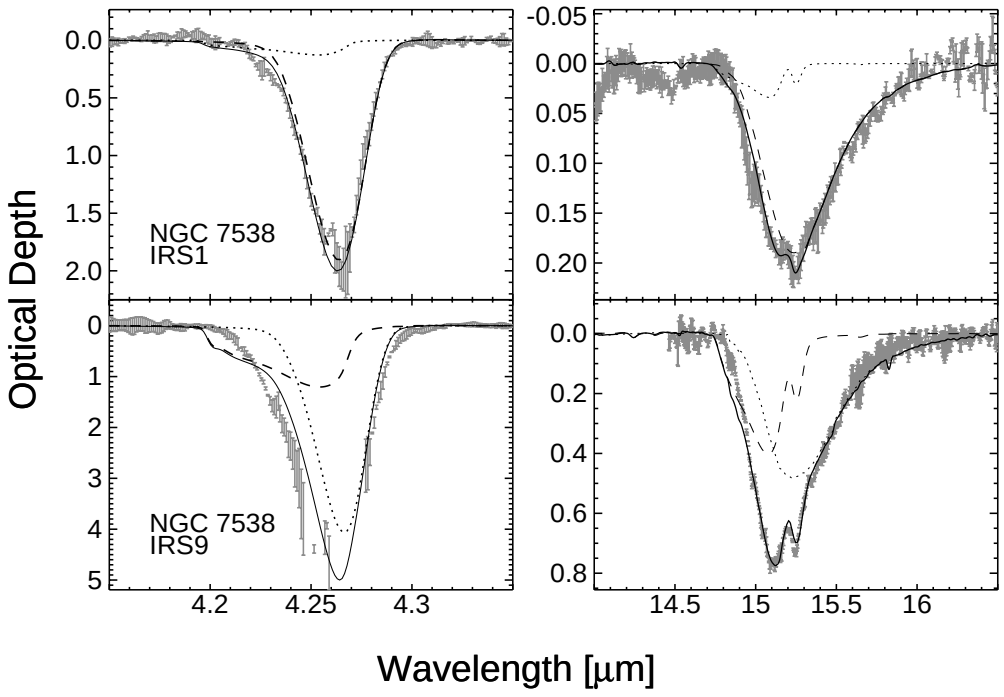

Figure 7.5: Interstellar CO_2 spectra presented as in Figs. 7.1–7.4, but for NGC 7538 IRS1 and NGC 7538 IRS9. Structure in the trough of the NGC 7538 IRS1 stretching mode is due to low flux levels. The stretching mode of NGC 7538 IRS9 is saturated and points with S/N < 1 have been omitted.

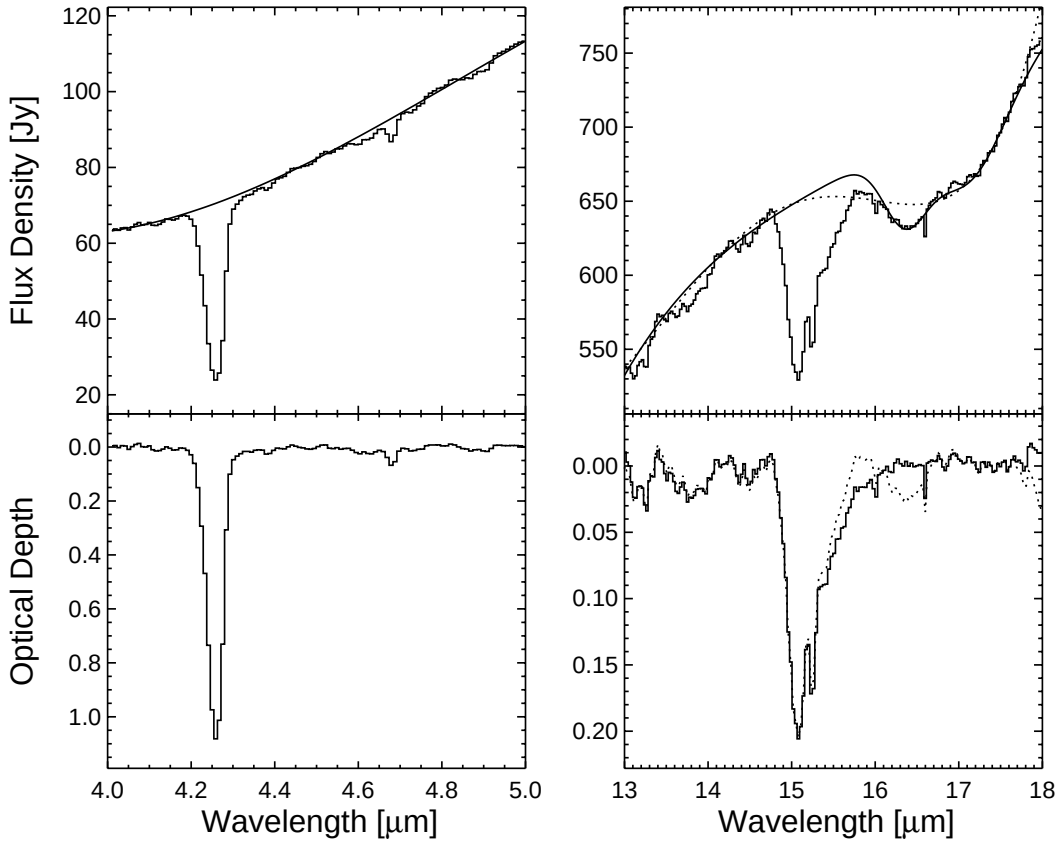

Figure 7.6: Demonstration of continuum fits using the SWS01 data of S 140. Left– stretching mode region; right– bending mode region. In the 15.2 μm region, two extreme cases are shown. The solid line is a third-order polynomial + a Gaussian fit to the 16–18 μm feature. The dotted line is a 5th-order polynomial fit to points adjacent to the CO_2 feature.

7.2.1 Continuum Determination

Continuum fits in the 4 μm region were obtained by fitting a low-order polynomial (order 1 to 3) to data points from 4.0 to 4.1 and 4.4 to 4.5 μm. Since the bending mode at 15.2 μm is located on the short-wavelength edge of the 18 μm silicate absorption, a fit was first made to the continuum from 14 to 25 μm using a low-order polynomial with points from 14 to 14.5 and 22 to 25 μm. The silicate feature was subtracted by fitting its shape with a Gaussian curve. As an example, continuum fits to the SWS01 data of S 140 are shown in Fig. 7.6.

Toward Elias 29, GL 490, GL 2136, NGC 7538 IRS1, Sgr A*, S140, W3 IRS5, and

W33 A, another feature of unknown origin centered near 16.4 μm became apparent after the subtraction. This absorption was also fit with a Gaussian and subtracted out to produce the final optical depth spectra. It is likely that this feature is merely the result of the band jump from SWS band 3A to 3C, since the RSRF is very low there.[13]

The 15.2 μm features in laboratory spectra typically contain a long-wavelength wing extending to about 16.3 μm. It is not clear whether this occurs in the SWS spectra: it may be hidden by the silicate bending mode in this region. Therefore, a proper continuum fit is not straightforward. In order to estimate error bars on the areas of the 15.2 μm features, continuum fits have also been made to to data points in the ranges 13–14 μm and 16.5–18 μm using low-order polynomials. An example is shown shown in Fig. 7.6, and the areas of the resulting 15.2 μm bending modes when two extreme (but equally valid) cases are considered are different by 17 %. Error bars in column density (§ 7.3.4) reflect this uncertainty in continuum shape in lines of sight where the 4.27 μm stretching mode is saturated. Where both features are seen, a weighted average was taken of the derived column densities from each.

Finally, the source of radiation in the line of sight toward Elias 16 is a background K 1 III star, and its spectrum contains photospheric absorption features at 4.295, 4.352, and 4.393 μm (Ch. 6). Cancellation of these lines was carried out for comparison with the protostars by ratioing the flux spectrum of Elias 16 by that of HR 8657, a K 2 III star with low extinction.

7.3 Analysis of Observed Absorption Features

Observed spectra for all sources are shown in Figs. 7.1–7.5 with the polar:nonpolar fits (described in § 7.3.3.1) and in Figs. 7.7–7.11 with the polar:annealed fits (§ 7.3.3.2). Tables 7.2 and 7.3 list their characteristics. In some cases, the bending mode was unobservable due to low flux levels (e.g., Elias 16), or too weak to distinguish from fringing or noise in the spectrum (e.g., GCS 4 and GL 4176). An extensive study of the corresponding interstellar $^{13}CO_2$ spectra may be found in

[13] More speculatively, this feature does appear coincident with a feature of CH_3 expected at this wavelength: therefore it should correlate with the known features of CH_3 at 3.4 and 6.8 μm. This has yet to be investigated.

Table 7.2: Properties of observed 4.27 μm features.

Source	ν_0 cm^{-1} (μm)	τ_0	$\Delta\nu$ cm^{-1}	S/N[a]	Comments
W3 IRS5	···	>3	∼20	28	sat.
GL 490	2346.2 (4.262)	0.46±0.05	21.3	27	
Elias 16	2344.6 (4.265)	$1.8^{+0.5}_{-0.2}$	19.6	63	long-λ wing
GL 4176	2345.4 (4.264)	0.40±0.02	17.8	97	long-λ wing
Elias 29	2343.5 (4.267)	2.77±0.2	17.1	49	contin. shift
Sgr A*	2342.3 (4.269)	0.70±0.01	16.7	100	short-λ wing
GCS 3 I	2343.3 (4.267)	0.48±0.02	15.4	67	
GCS 4	2342.0 (4.270)	0.22±0.02	12.8	40	
W33 A	···	>5	∼20	58	sat.
GL 2136	2342.7 (4.269)	2.40±0.08	18.5	144	contin. shift
GL 2591	2344.3 (4.266)	0.55±0.01	24.0	215	brd, wings
S 140	2346.5 (4.262)	1.25±0.04	23.9	50	
NGC 7538 IRS1	2344.7 (4.265)	2.03±0.11	16.4	40	
NGC 7538 IRS9	···	>5	∼20	15	saturated

[a] Median signal-to-noise ratio across range of feature.

Boogert et al. (1998).

7.3.1 Observational Characteristics

The 4.27 μm feature is clearly saturated toward NGC 7538 IRS9, W3 IRS5, and W33 A (Figs. 7.1–7.5). Sources Elias 29, GL 2136, GL 2591, and GL 4176 exhibit a shallow shoulder ($\tau \approx 0.1$) on the long-wavelength side of the feature, and it is suspected that this is the result of an unidentified, broad underlying component. On the short-wavelength side of the feature, most sources display a wing likely due to a large nonpolar component as seen in laboratory ices containing pure CO_2 (Sandford & Allamandola 1990; Ehrenfreund et al. 1997). The spectra of GL 2136, GL 2591 and GL 4176 also contain shallow absorption shoulders on the short- and long-wavelength sides of the stretching mode. These absorptions are likely due to the unresolved P- and R-branches of gas-phase CO_2, consistent with the strong gas-phase ν_2 absorptions seen at 14.97 μm toward these sources. Estimated underlying gas components in the 4 μm region are plotted in Figs. 7.1–7.5 and have been subtracted from the

Table 7.3: Properties of observed 15.2 μm features. Values marked with ":" have a high degree of uncertainty.

Source	ν_i cm^{-1} (μm)	τ_i	$\Delta\nu_i$[a] [cm^{-1}]	$\Delta\nu$[b] [cm^{-1}]	S/N[c]	Comments[d]
W3 IRS5	655.3 (15.26)	0.37±0.01	3.2	24.6	260	wk gas, wk 15.4 sh
	660.7 (15.14)	0.34±0.01	2.5			[Ne III]
GL 490	651.7 (15.34)	0.08±0.02	···	22.2	87	brd single peak
GL 4176	654.8 (15.27)	0.047±0.003	2.5	26.3	500	str gas
	660.7 (15.14)	0.044±0.003	3.0			str 15.4 sh, FT
Elias 29	654.2 (15.29)	0.33±0.02	1.9	23.1	42	str 15.4 sh
	661.4 (15.12)	0.30±0.01	4.0			
Sgr A*	654.5 (15.28)	0.077±0.005	2.1:	20.3	500	brd peak, [Ne III]
	662: (15.11)	0.08:	1.7:			poss 2nd peak
GCS 4	652: (15.34)	0.04±0.01	···	19:	90	vstr [Ne III]
	662: (15.11)	0.05±0.01	···			
W33 A	656.3 (15.24)	0.58±0.01	2.8	27.4	108	mod gas
	660.7 (15.14)	0.57±0.02	4.3			str 15.4 sh
GL 2136	656.0 (15.24)	0.30±0.01	2.9	24.5	500	str gas
	662.0 (15.11)	0.28±0.01	4.9			str 15.4 sh
GL 2591	656.0 (15.24)	0.073±0.005	2.8	25.1	307	vstr gas
	661.8 (15.11)	0.068±0.005	3.2			str 15.4 sh, FT
S 140	655.8 (15.25)	0.21±0.01	3.1	16.3	136	sharp pks
	662.9 (15.09)	0.24±0.02	6.6			
N 7538 IRS1	656.1 (15.24)	0.21±0.01	3.5	24.3	139	wk gas, wk 15.4 sh
	660.5 (15.14)	0.19±0.01	1.8			wk [Ne III], FT
N 7538 IRS9	655.9 (15.25)	0.736±0.005	2.2	21.1	101	wk gas
	662.1 (15.10)	0.766±0.005	4.3			

[a] FWHM relative to underlying broad component.
[b] Width of the entire feature.
[c] Median signal-to-noise ratio across range of feature.
[d] "FT" indicates that a Fourier transform was applied to the data to remove excessive fringing (§ 7.2).

spectra before performing the laboratory fits (§ 7.3.3). The apparent "emission" in the spectrum of Elias 16 at 4.22 and 4.27 μm is not real, but the result of differences in the up and down scans of this observation (due to the low flux level of this object at these wavelengths; see Ch. 6). Spurious structure also exists in the troughs of the 4.27 μm features of Elias 29 and NGC 7538 IRS1, which may be close to saturation.

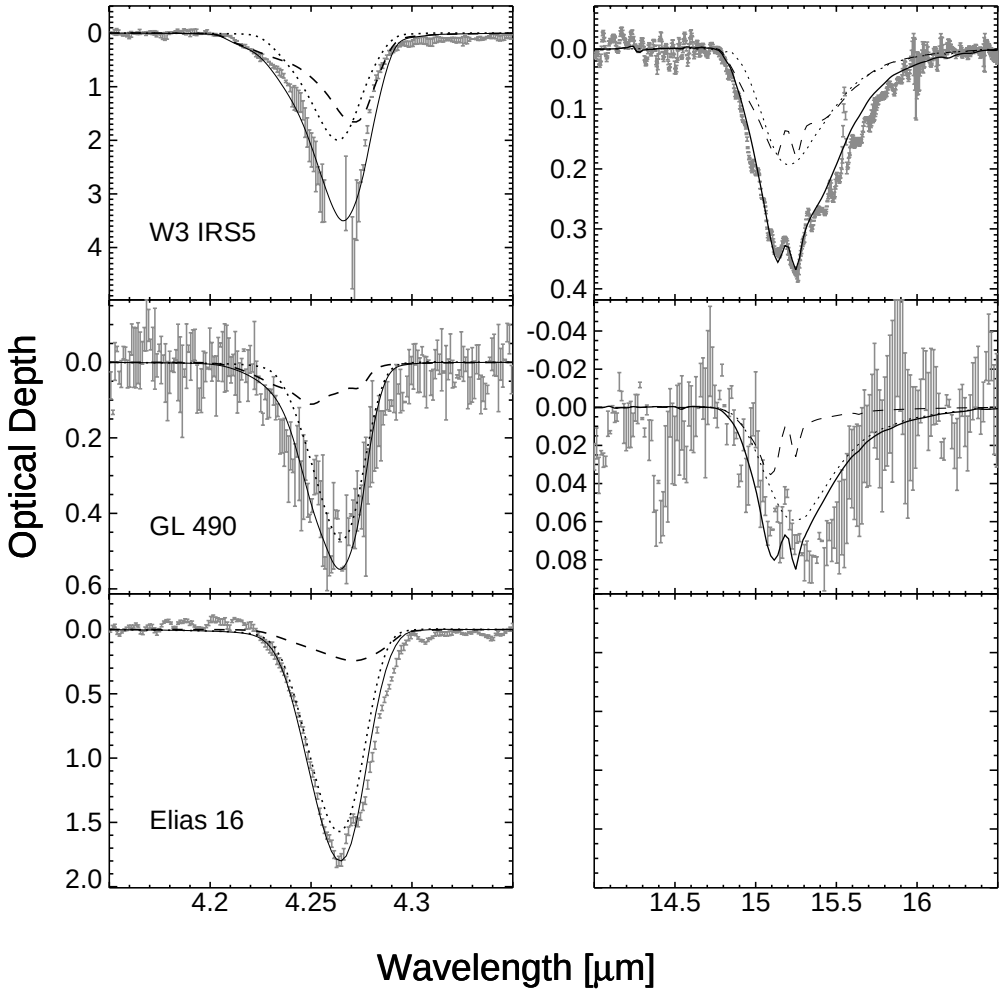

Figure 7.7: Fits to interstellar CO_2 spectra toward W3IRS5, GL490, and Elias 16 using polar + annealed methanol-rich laboratory ices. Dotted lines– polar components; dashed lines– annealed components; solid lines– sum of polar and annealed components.

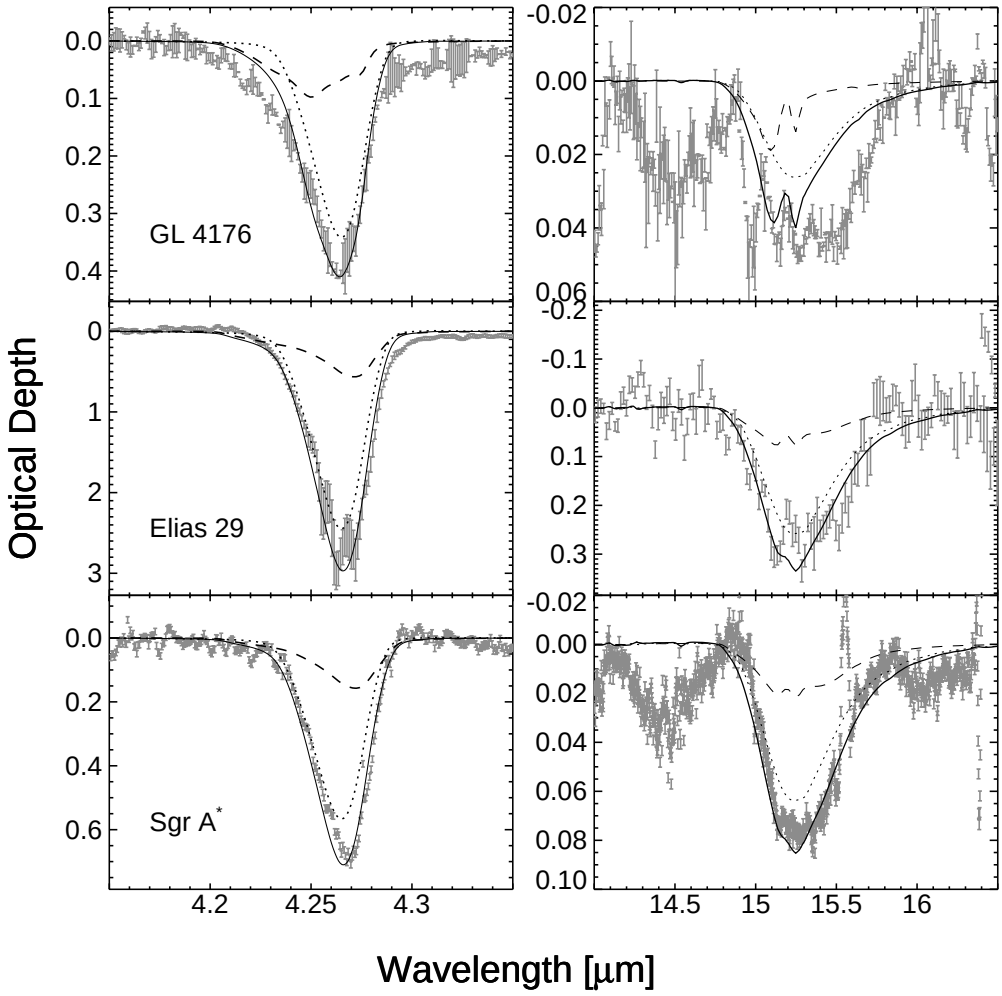

Figure 7.8: Polar:annealed laboratory fits to the CO_2 spectra toward GL 4176, Elias 29, and Sgr A*. Plotting symbols are identical to those in Fig. 7.7.

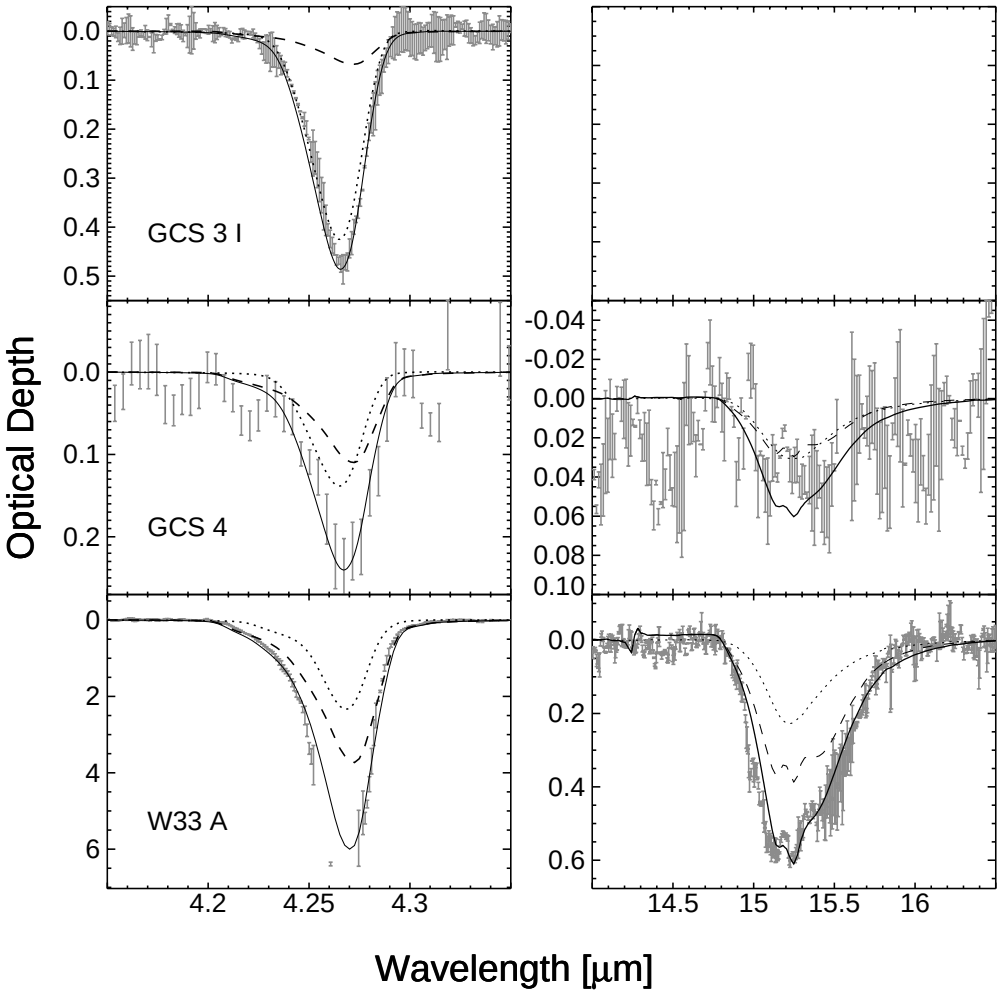

Figure 7.9: Polar:annealed laboratory fits to GCS 3 I, GCS 4, and W33 A. Plotting symbols are identical to those in Figs. 7.7 and 7.8.

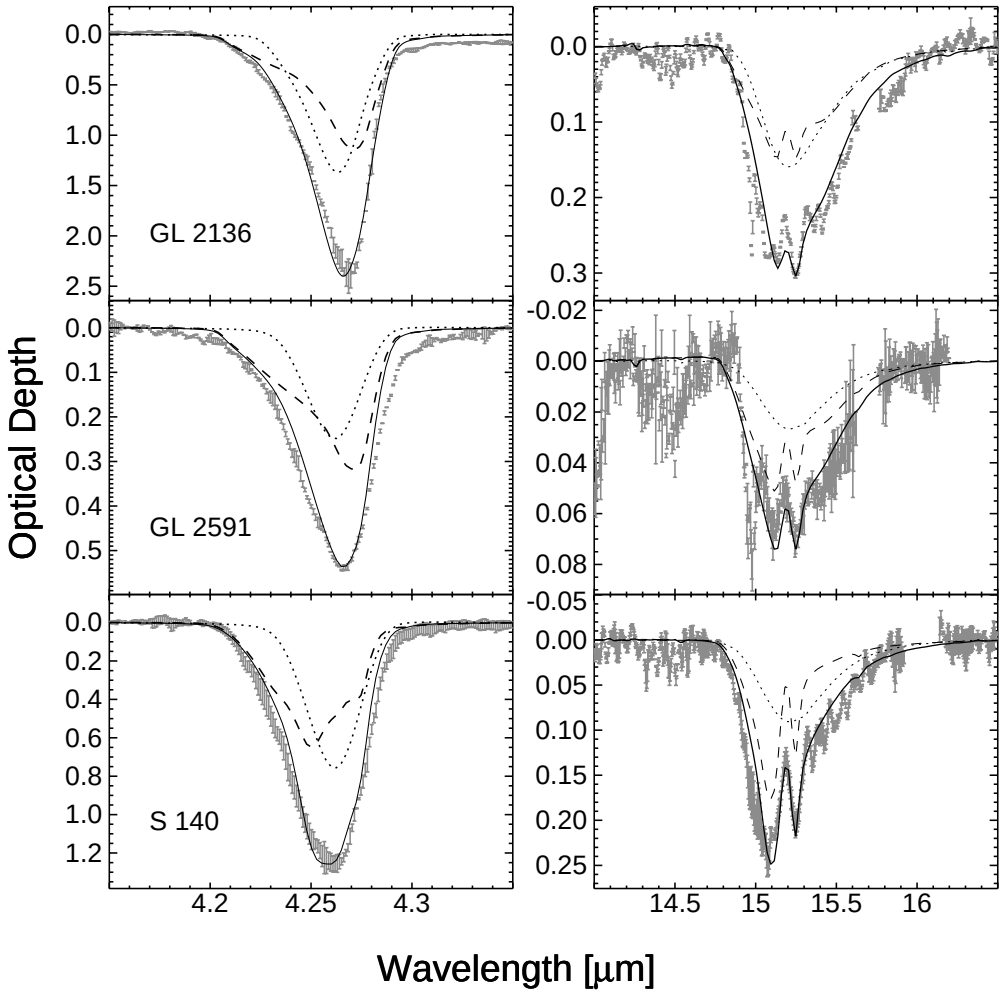

Figure 7.10: Polar:annealed laboratory fits to GL 2136, GL 2591, and S 140. Plotting symbols are identical to those in Figs. 7.7–7.9.

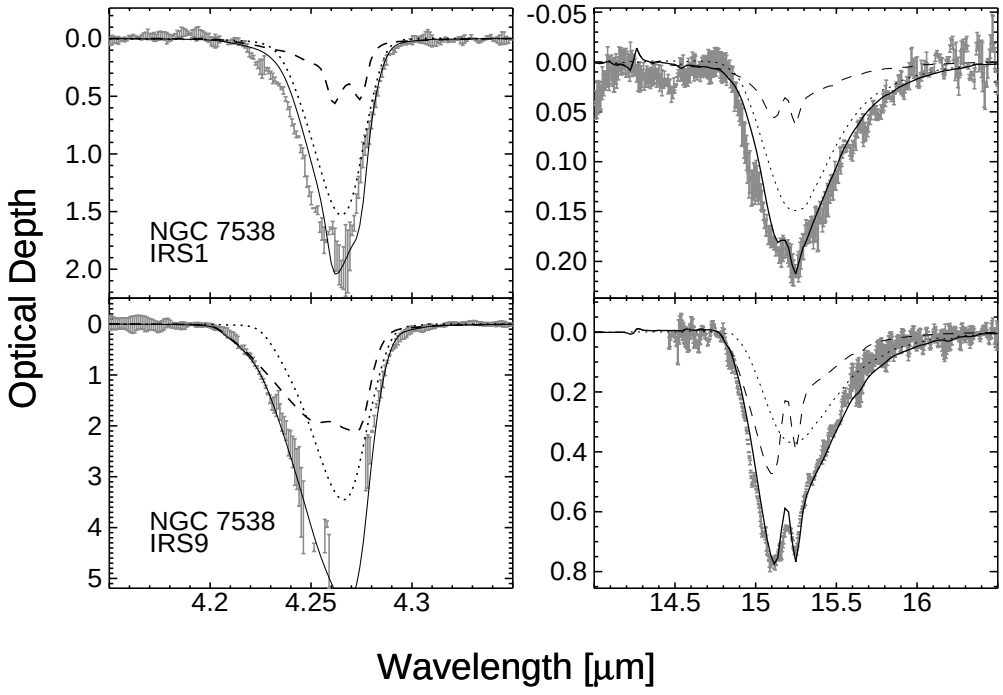

Figure 7.11: Polar:annealed laboratory fits to NGC 7538 IRS1 and NGC 7538 IRS9. Plotting symbols are identical to those in Figs. 7.7–7.10.

The observed CO_2 15.2 μm bending modes (Figs. 7.1–7.5) have at least two peaks toward most sources: apart from those with poor signal-to-noise ratio, the only exception is Sgr A*. Toward GL 2136, GL 2591, GL 4176 NGC 7538 IRS1, NGC 7538 IRS9, Sgr A*, W3 IRS5, and W33 A, absorption due to the Q-branch of the gas-phase CO_2 ν_2 band can be seen at 14.97 μm with a width of about 0.02 μm. The gas-phase features toward GL 2591 and GL 4176 may have been broadened by attempts to remove fringing (§ 5.2 and § 7.2), but their widths could also be due to high CO_2 excitation temperatures toward these sources. The gas-phase CO_2 data will be further analyzed and discussed by Boonman et al. (1998). At the resolution of these observations ($\lambda/\Delta\lambda \approx 1800$), all Q-branch ro-vibrational lines merge into one apparent absorption feature. This unresolved band is easier to observe than the corresponding gas-phase ν_3 band at 4.27 μm which is intrinsically 10 times stronger but has only P- and R-branch structure (van Dishoeck et al. 1996). The spectra of W3 IRS5, Sgr A*, and GCS 4 also contain the fine-structure line of doubly ionized neon [Ne III] at 15.55 μm, indicating the presence of ionized gas (an H II region) in these lines of sight.

In general, the profiles of all the observed interstellar 15.2 μm features can be broken down into three components: a broad underlying feature (observed $\Delta\nu$ = 16.3–27.4 $\mathrm{cm^{-1}}$ vs. $\approx 25\,\mathrm{cm^{-1}}$ in the lab), a pair of sharp peaks at 15.15 and 15.27 μm (observed $\Delta\nu$ = 1.7–6.6 $\mathrm{cm^{-1}}$ vs. $\approx$ 2–4 $\mathrm{cm^{-1}}$ in the lab), and a shoulder near 15.4 μm (laboratory measurements from Ehrenfreund et al. 1997). The relative contributions of these components vary from source to source. For example, the height of the peaks near 15.15 and 15.27 μm are highly variable and measure up to 40 % of the total peak optical depth (in S 140). Toward GL 2136, NGC 7538 IRS1, S 140, W3 IRS5, and W33 A (and weakly towards NGC 7538 IRS9), a third peak or broad shoulder is apparent on the long-wavelength side of the 15.2 μm feature at $\lambda \approx 15.4\,\mu$m (649 $\mathrm{cm^{-1}}$). In most cases, this absorption is broad and shallow, but appears sharply peaked toward GL 2136.

The broad underlying component is attributed to CO_2 in a polar environment (presumably an H_2O- and/or CH_3OH-rich ice). The two sharp peaks at 15.15 and 15.27 μm have been shown to form in annealed CO_2-bearing ices and in certain

nonpolar ice mixtures upon warm-up (Sandford & Allamandola 1990; Ehrenfreund et al. 1997). In the former, ice segregation is taking place; this forms a CO_2 ice that is embedded in the matrix of the other component. The broad shoulder does not seem to correlate with the other components, and recent lab results (Ehrenfreund et al. 1998) indicate that this absorption may be a result of CO_2:CH_3OH ice complexes (cf., § 7.3.3).

7.3.2 Laboratory Data

Laboratory experiments by Sandford & Allamandola (1990) and Ehrenfreund et al. (1997) have shown that at 10 K, the CO_2 bending mode consists of one broad absorption for all ice mixtures studied, with the exception of pure CO_2 which has two peaks. This vibration is doubly degenerate and splits when the axial symmetry of the molecule is broken. CO_2 is known to form "T-shaped" complexes with a variety of molecules (e.g., CO_2:CH_3OH complexes), leading to very broad features. Upon warm up of such mixtures, multi-peaked structures form in all CO_2 IR features (Ehrenfreund et al. 1998). The exact positions and widths of these peaks vary according to ice matrix and thereby greatly constrain the ice composition (§ 7.3.3).

The $^{13}CO_2$ asymmetric stretching mode is, like the 15.2 μm bending mode, an extremely sensitive diagnostic of the ice matrix (Ehrenfreund et al. 1997; Boogert et al. 1998). While it is the splitting of the 15.2 μm feature which indicates ice composition, both the peak position and width of the $^{13}CO_2$ stretching mode are strongly dependent on ice composition; polar and nonpolar components may be easily distinguished. When heated however, the $^{13}CO_2$ features of polar and nonpolar ices do begin to overlap, creating a certain level of ambiguity (see discussion in Boogert et al. 1998).

7.3.3 Laboratory Fits to Observational Data

All spectra were matched to a suite of laboratory data as described in detail in § 5.3. Particle shape corrections were applied to the lab data using four different grain models derived from the real and imaginary parts of the ice's refractive index (§ 5.3.2; for a detailed discussion of the calculation procedure for these mixtures, see

Ehrenfreund et al. 1997). In general, a continuous distribution of ellipsoids where each shape is equally probable gives the best fit.

The laboratory fits giving the best agreement to all three absorption features in each source are listed in Table 7.4 (for the polar:nonpolar fits) and Table 7.5 (for the polar:annealed fits). Corresponding spectra are shown in Figs. 7.1–7.5 and 7.7–7.11. The results of these fits indicate that two chemically-different CO_2 ice components exist along these lines of sight– one dominated by H_2O (polar), and another dominated by CO_2 itself (nonpolar or annealed). The height and sharpness of the 15.2 μm feature's sub peaks and the positions and widths of the 4.38 μm feature's two components are the most sensitive indicators of the CO_2 ice environment and thereby give the most stringent constraints to the resulting fits.

7.3.3.1 Polar:Nonpolar fits

Fits to the observed CO_2 features have been made in order to determine the ice environment(s) in the studied lines of sight. Since it has been shown that solid interstellar CO exists in both polar and nonpolar ice phases (Tielens et al. 1991; Chiar et al. 1995; Chiar et al. 1998b), similar fits have been attempted for the interstellar CO_2 features observed here. In conducting the polar:nonpolar fits, general agreement could be found between the 15.2 μm bending mode and the feature of $^{13}CO_2$ at 4.38 μm (i.e., the same mixtures with the same relative abundances gave good fits for each feature). In the case of W33 A, however, fits to the 15.2 μm feature indicate a polar:nonpolar ratio of about 2, while the $^{13}CO_2$ feature suggests a much higher ratio of 12. Interestingly, the opposite is found for the features of W3 IRS5, where the $^{13}CO_2$ indicates a smaller polar:nonpolar ratio than the $^{12}CO_2$ (1.3 vs. 5.0). In each of these cases, a compromise between the two features was taken (see Table 7.4 and Figs. 7.1 and 7.3).

Toward sources with a strong nonpolar component, it was difficult to fit the 4.27 μm feature with the same mixtures as the 4.38 and 15.2 μm features. A reasonable fit is possible, but the nonpolar component is always underestimated, or the structure in the 4.38 and 15.2 μm features is not well-reproduced. These problems are thought to come from the derivation of the ices' optical constants (n and k),

Table 7.4: Summary of polar:nonpolar laboratory fits.

Source	Polar Component	Nonpolar Component	% Nonpolar[a]
W3 IRS5	H_2O:CH_3OH:CO_2 = 100:8:14, 10 K	Pure CO_2, 80 K	13±4
GL 490	H_2O:CH_3OH:CO_2 = 100:8:14, 10 K	Pure CO_2, 80 K	<5
Elias 16	H_2O:CO:CO_2 = 100:3:20, 20 K	···	<4
GL 4176	H_2O:CO_2 = 100:14, 10 K	Pure CO_2, 80 K	20±3
Elias 29	H_2O:CH_3OH:CO_2 = 100:8:14, 10 K	H_2O:CO_2 = 1:100, 30 K	7±2
Sgr A*	H_2O:CH_3OH:CO_2 = 100:8:14, 50 K	···	<5
GCS 3 I	H_2O:CH_3OH:CO_2 = 100:8:14, 50 K	···	<5
GCS 4	H_2O:CH_3OH:CO_2 = 100:8:14, 80 K	Pure CO_2, 80 K	<23
W33 A	H_2O:CO_2 = 100:125, 125 K	CO:CO_2 = 100:70, 10 K	15±5
GL 2136	H_2O:CO_2 = 100:14, 80 K	Pure CO_2, 80 K	20±3
GL 2591	H_2O:CH_3OH:CO_2 = 100:8:14, 10 K	Pure CO_2, 80 K	27±4
S 140	H_2O:CH_3OH:CO_2 = 100:8:14, 10 K	H_2O:CO_2 = 1:6, 75 K	50±5
NGC 7538 IRS1	H_2O:CH_3OH:CO_2 = 100:8:14, 10 K	Pure CO_2, 80 K	12±2
NGC 7538 IRS9	H_2O:CH_3OH:CO_2 = 100:8:14, 50 K	H_2O:CO_2 = 1:10, 30 K	34±5

[a] Percent nonpolar CO_2 required by the fit. Limits obtained by adding small amounts of Pure CO_2 at various temperatures.

which has been shown to be somewhat controversial. For example, the peak values of n and k derived for the 4.27 μm feature by different laboratories differ by as much as a factor of two (Trotta 1996; Ehrenfreund et al. 1997). Moreover, any optical constant errors are magnified by the particle shape corrections in strong absorptions, since the calculated cross-sections are proportional to $1/nk$ (Eq. 5.5). Where detected with a high enough signal, the 4.38 μm feature of $^{13}CO_2$ is taken to be the most reliable indicator of the CO_2 ice environment in these fits, since it is unaffected by particle shape calculations involving the optical constants of the ice. The next most reliable indicator is the 15.2 μm bending mode of $^{12}CO_2$.

Figure 7.12 contains a plot of the resulting polar and nonpolar fractions of the total CO_2 column density vs. the cold gas component temperature measured in these lines of sight (see Table 7.6). The trend appears to be that more nonpolar CO_2 exists in lines of sight with warmer gas.

7.3.3.2 Fits with annealed CH_3OH-rich ices

The CO_2 bending mode typically contains a shoulder at 15.4 μm that is not well-represented by simple polar:nonpolar constituents. As a means of tracing its source, the observed spectra have also been compared with those of thermally annealed, methanol-rich laboratory ices (which do display such a feature; see Fig. 7.13). These ices are highly inhomogeneous as a result of segregation of the CH_3OH and CO_2 components. They are therefore no longer well-represented by thin films and particle shape corrections (§ 5.3.2) are not required, and their spectra in the laboratory may be directly compared with interstellar spectra. The physical structure of these ices will be described in detail by Ehrenfreund et al. (1998).

In Fig. 7.13, H_2O:CH_3OH:CO_2 = 1:1:1 mixtures have been fitted to the observed bending mode spectra. The temperature evolution for this ice shows a remarkable similarity to the ISO spectra. At low temperatures, the 15.2 μm feature is broad, with no sharp peaks (Sgr A*). As it is heated, the peaks indicative of pure CO_2 ice appear (NGC 7538 IRS9) and grow stronger with increasing temperature, showing that the CO_2 molecules are annealing within the polar ice (NGC 7538 IRS1, W3 IRS5). When these peaks are strong, the shoulder at 15.4 μm becomes dis-

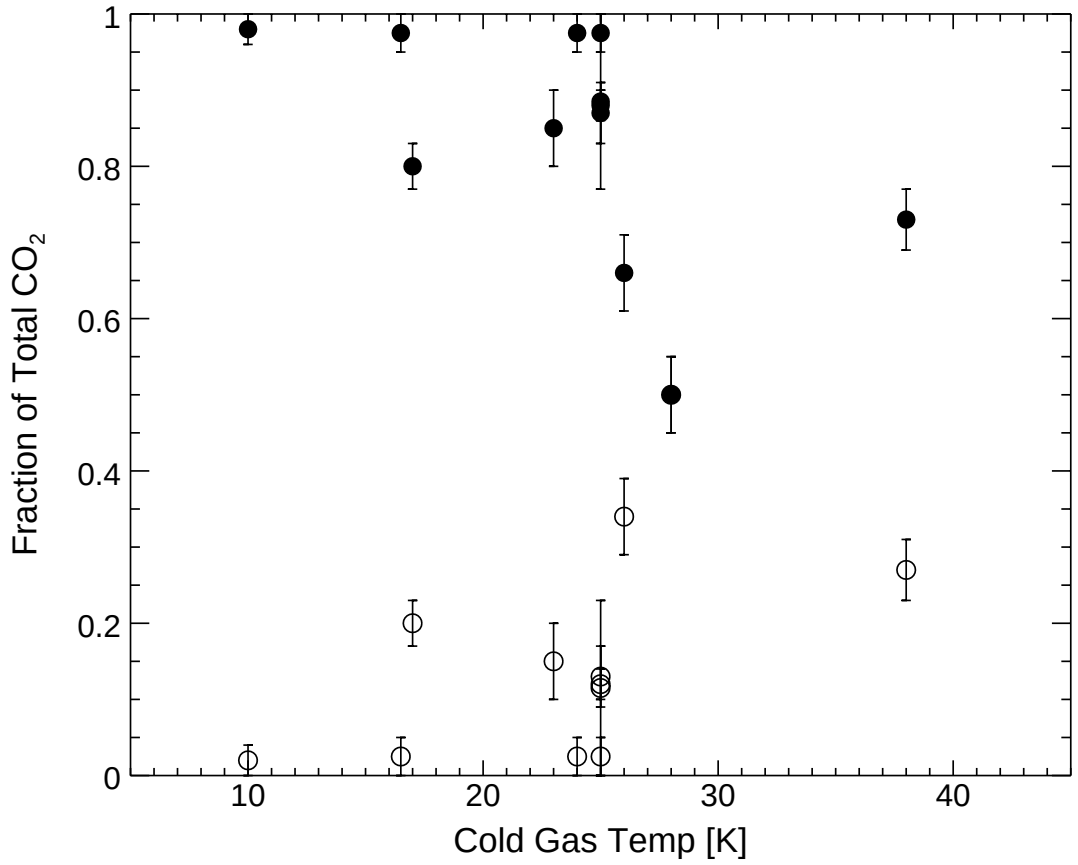

Figure 7.12: Polar and nonpolar fractions of the total CO_2 column densities (as derived from the fits to the observed 4.38 and 15.2 μm features) vs. line-of-sight cold gas temperatures from Table 7.6. Filled circles– polar CO_2; Empty circles– nonpolar CO_2. Arrows indicate upper limits on nonpolar CO_2.

tinct (W33 A, GL 2136). Finally, the nonpolar ices dominate the spectrum at high temperatures, where nearly all of the CO_2 has annealed (S 140).

While the observed CO_2 spectrum toward each source is well-matched by a single H_2O:CH_3OH:CO_2 = 1:1:1 ice (Fig. 7.13), the relative abundances of CH_3OH and CO_2 required do not agree with observations (interstellar $N_{CH_3OH}/N_{CO_2} \lesssim 50\,\%$; Allamandola et al. 1992; Brooke, Sellgren, & Smith 1996). Other polar molecules in the ice could invoke this kind of interaction with CO_2 (Ehrenfreund et al. 1998), and possibly only a fraction of the CO_2 molecules in a given line of sight is needed to produce the observed 15.4 μm shoulders. Indeed, the CO_2 profiles may also be

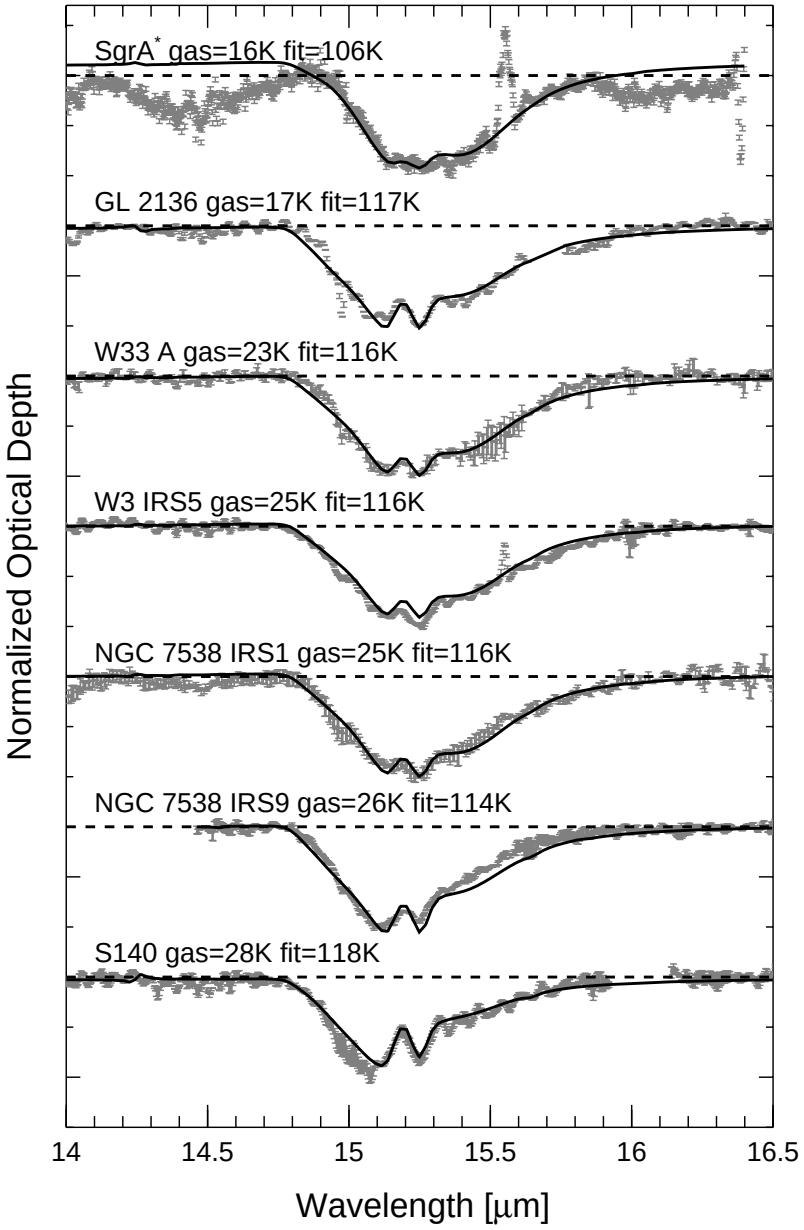

Figure 7.13: Observed 15.2 μm features ordered by cold gas temperature from Table 7.6 plotted with a H_2O:CH_3OH:CO_2 = 1:1:1 mixture at various temperatures.

Table 7.5: Summary of polar:annealed laboratory fits. All annealed components consist of the mixture H_2O:CH_3OH:CO_2 = 1:1:1.

Source	Polar Component	Annealed T [K]	% Annealed[a]
W3 IRS5	H_2O:CO_2 = 100:14, 10 K	136	46±17
GL 490	H_2O:CO_2 = 100:14, 10 K	136	≤ 25
Elias 16	H_2O:CO_2 = 100:14, 10 K	10	≤ 17
GL 4176	H_2O:CO_2 = 100:14, 10 K	136	28±10
Elias 29	H_2O:CO_2 = 100:14, 10 K	117	22±10
Sgr A*	H_2O:CO_2 = 100:14, 10 K	115	≤ 40
GCS 3 I	H_2O:CO_2 = 100:14, 10 K	115	≤ 15
GCS 4	H_2O:CO_2 = 100:14, 10 K	115	≤ 65
W33 A	H_2O:CO_2 = 100:14, 80 K	112	65±15
GL 2136	H_2O:CO:CO_2 = 100:3:20, 20 K	117	75±25
GL 2591	H_2O:CO_2 = 100:14, 10 K	117	44±11
S 140	H_2O:CO_2 = 100:14, 10 K	136	52±10
NGC 7538 IRS1	H_2O:CO_2 = 100:14, 10 K	145	25±8
NGC 7538 IRS9	H_2O:CO:CO_2 = 100:3:20, 20 K	119	45±5

[a] Percentage of total CO_2 column denisty contained in the annealed ice component.

reproduced by a sum of methanol-rich and methanol-poor ices. The methanol-poor ices provide the broad underlying component, and the annealed methanol-rich ices provide both the sharp double peaks and the 15.4 μm shoulder.

In order to constrain the amount of CH_3OH ice required, two-component fits to the interstellar spectra have been performed using the methanol-free polar ices plus the thermally annealed methanol-rich ice listed in Table 5.1. The fitting procedure is the same as described above for the polar:nonpolar ices (§ 7.3.3.1). The results are summarized in Table 7.5 and presented in Figs. 7.7–7.11. In general, fits which matched the bending mode also made good fits to the 4.27 and 4.38 μm features. The amount of annealed CO_2 which gives a good fit in each case is not unique, but spans the range listed in Table 7.5. Where known, abundances of interstellar CH_3OH are consistent with these ranges. While the spectra of these ices closely resemble those of the polar:nonpolar ices, they contain additional structure which match the interstellar spectra more closely.

7.3.4 Column Densities

Column densities of CO_2 (N_{CO_2}), in units of cm^{-2}, were measured using the formula given in Eq. (2.4). Where there is sufficient signal-to-noise in both the 4.27 and 15.2 μm features, column densities derived from each individual feature agree to within 24 % for each line of sight.

In these data, the differences in N_{CO_2} as derived from the two CO_2 features are dominated by the uncertainties in the local continuum at 15.2 μm, and are consistent within these error bars. Also, values of N_{CO_2} as derived from the 4.27 μm feature show no consistent trend with those derived from the 15.2 μm feature. Thus, within the observational errors, it is assumed that the 4.27 and 15.2 μm features probe the same CO_2 population. Derived values of N_{CO_2} are listed in Table 7.6, and their error bars reflect both the uncertainty in the continuum fits as well as the difference between values derived from the 4.27 and 15.2 μm features (where possible).

7.3.4.1 Correlation of Solid CO_2 with Solid H_2O and CO

A strong correlation exists between N_{CO_2} and N_{H_2O} and is shown in Fig. 7.14. All lines of sight observed– including the quiescent cloud medium toward Elias 16– have total CO_2 column densities between 10–23 % that of H_2O (excluding GCS 3 I and GCS 4, which have uncertain values of N_{H_2O}). A weighted fit to all data points passes through the origin to within observational error and indicates that for an average molecular cloud,

$$\frac{N_{CO_2}}{N_{H_2O}} = 0.17 \pm 0.01 \,, \tag{7.1}$$

where the value of $N_{H_2O} = 9.0 \times 10^{18}\,cm^{-2}$ for W33 A has been used (Allamandola et al. 1992). With the higher value of $N_{H_2O} = 4.7 \times 10^{19}\,cm^{-2}$ (Tielens et al. 1984) adopted in its place, Eq. (7.1) becomes $N_{CO_2}/N_{H_2O} = 0.16 \pm 0.01$.

The formation of CO_2 is undoubtedly linked to the CO molecule. A plot of the total column density of CO_2 versus that of CO in the observed lines of sight is shown in Fig. 7.15. The quiescent ISM stands out with a relatively high abundance of (nonpolar) CO as a result of its low temperature. It is also apparent from the trend of points in this plot that the correlation line has a positive intercept on the N_{CO_2} axis, implying that significant amounts of CO_2 exist even where there is little

Table 7.6: Column densities as gas temperatures in the observed lines of sight. Values marked with ":" have a high degree of uncertainty.

	N [10^{17} cm^{-2}]								N_H[a]	Gas T	
Source	CO_2	CO_2(p)	CO_2(np)	H_2O	CO	CO(p)	CO(np)	CH_3OH	[10^{23} cm^{-2}]	[K]	Refs
W3 IRS5	7.1±1.8	6.2	0.9	54	1.6	< 0.5	1.1	< 0.8	2.7	25,577	1,2,3,4
GL 490	1.7±0.3	1.7	< 0.1	7.3	1.0	< 0.3	0.69	···	0.98	24,107	1,2,5
Elias 16	$4.6^{+1.3}_{-0.6}$	4.6	< 0.2	25	6.5	0.8	5.6	< 0.7	0.39	10	6,7,8,9,10,11
GL 4176	1.2±0.2	1.0	0.2	9	< 0.5	···	···	···	···	···	
Elias 29	6.7±0.5	6.2	0.5	32	1.6	0.2	1.4	···	···	···	12,13
Sgr A*	1.7±0.2	1.7	< 0.1	12	< 1.5	···	···	···	···	16.5,240	14,15,16
GCS 3 I	1.1±0.1	1.1	< 0.1	1.3:	< 0.9	···	···	···	···	···	
GCS 4	0.7±0.2	0.7	< 0.2	1.8:	< 0.9	···	···	···	···	···	
W33 A	14.5±1.3	12.3	2.2	90/470[b]	8.9	6.6	2.3	5–9	2.8	23,120	1,3,17,18,19
GL 2136	7.8±0.3	6.2	1.6	50	1.1	1.1	···	4–8	1.8	17,580	1,2,3,19,20
GL 2591	1.6±0.2	1.2	0.4	17	< 0.2	···	···	∼ 4	1.4	38,1010	1,3,19
S 140	4.2±0.1	2.1	2.1	21.5	< 0.2	···	···	< 2.0	1.4	28,390	1,3,18
NGC 7538 IRS1	5.1±0.2	4.5	0.6	31	1.7	···	···	···	2.2	25,176	1,3
NGC 7538 IRS9	16.3±1.8	10.8	5.5	80	12.	1.4	11.	4–12	1.6	26,180	1,2,3,17,19,21
RAFGL 7009 S	25.0[c]	···	···	110	18.0	···	···	···	···	···	22

[a] Derived using $N_H = 3.5 \times 10^{22}$ cm$^{-2} \cdot \tau_{9.7}$

[b] Values derived from the 3.1 and 6.0 μm features disagree. See discussions in Allamandola et al. 1992 and Gibb et al. 1998.

[c] An uncertainty of 10% is assumed for trend analyses.

REFERENCES.—(1) Willner et al. 1982; (2) Tielens et al. 1991; (3) Mitchell et al. 1990; (4) Brooke, Sellgren, & Smith 1996; (5) Mitchell et al. 1995; (6) Whittet et al. 1998; (7) Whittet et al. 1988; (8) Chiar et al. 1995; (9) Elias 1978b; (10) Pratap et al. 1997; (11) Chiar, Adamson, & Whittet 1996; (12) Kerr, Adamson, & Whittet 1993; (13) Elias 1978a; (14) McFadzean et al. 1989; (15) Tielens et al. 1996; (16) Serabyn & Güsten 1986; (17) Chiar et al. 1998b; (18) Allamandola et al. 1992; (19) Whittet et al. 1997; (20) Schutte et al. 1996a; (21) Schutte et al. 1996b; (22) d'Hendecourt et al. 1996.

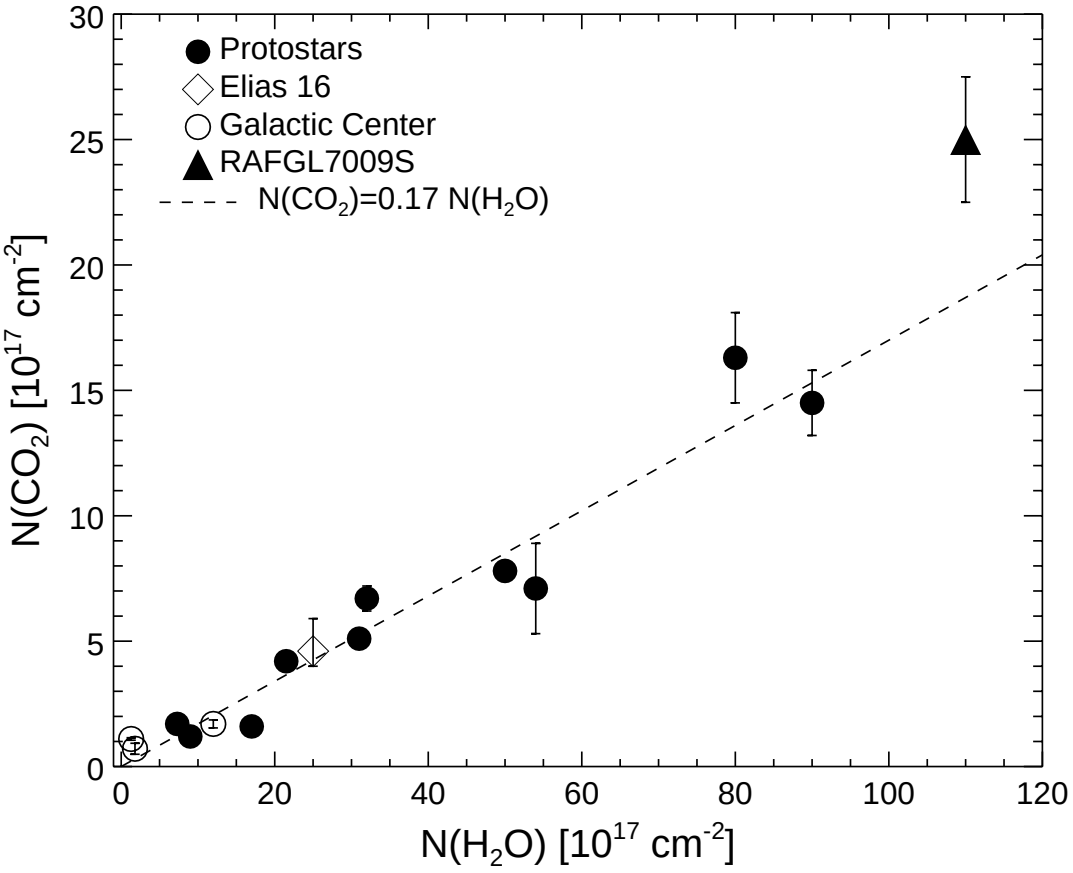

Figure 7.14: CO_2 column density vs. H_2O column density toward sources in Table 7.6. Squares– galactic center sources; circles– protostars; diamond– Elias 16 (quiescent cloud); triangle– RAFGL 7009 S (d'Hendecourt et al. 1996; 10 % uncertainty assumed); Dashed line indicates the average of all data, $N_{CO_2} = 0.17 N_{H_2O}$.

or no detectable solid CO. A best fit to the protostars with $N_{CO_2} > 4 \times 10^{17}\,\mathrm{cm}^{-2}$ gives

$$N_{CO_2} = (1.1 \pm 0.1)\, N_{CO} + (4.2 \pm 0.1) \times 10^{17}\ \mathrm{cm}^{-2}\ . \qquad (7.2)$$

Since CO is more volatile than CO_2, it will evaporate from the grain surfaces at lower temperatures (sublimation temperatures for pure CO and CO_2 are 17 and 45 K, respectively) and is held within H_2O matrices less effectively than CO_2. CO cannot exist in the more diffuse, outer regions of dark clouds where the interstellar radiation field has a strong influence (Chiar et al. 1995).

Plots of the polar and nonpolar CO_2 concentrations versus CO concentration

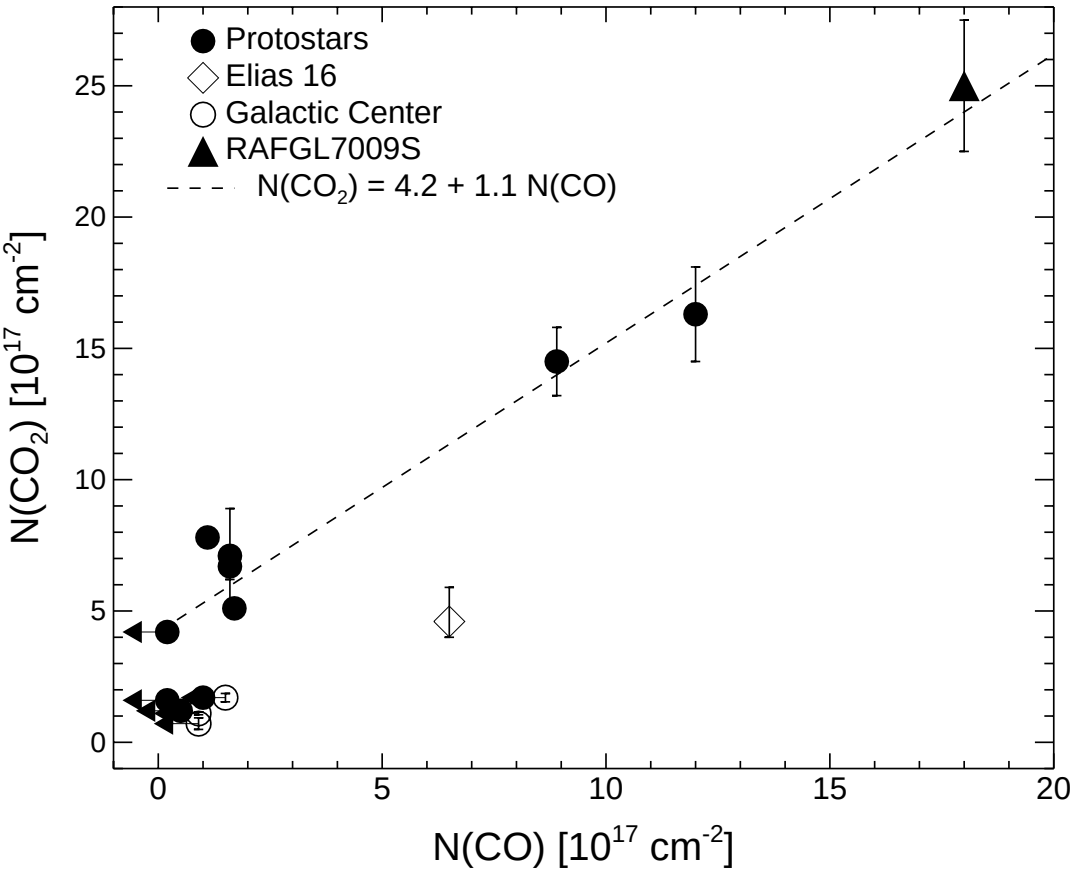

Figure 7.15: Total CO_2 column density vs. total CO column density in observed lines of sight. Symbols are identical to those in Fig. 7.14. Arrows indicate upper limits on N_{CO}. Dashed line indicates the trend for protostars with $N_{CO_2} > 4\times 10^{17}$ cm^{-2}: $N_{CO_2} = 4.2\times 10^{17}$ cm^{-2} +1.1 N_{CO}.

in these lines of sight (all relative to H_2O) are shown in Fig. 7.16. It is interesting to note that the quiescent cloud medium is consistent with the trend followed by the other lines of sight in this figure. Polar CO_2 concentrations seem to increase with higher CO concentrations. This is probably due to their respective trends with temperature: in cold regions both polar CO_2 and CO scale with total column density, whereas nonpolar CO_2 is formed under conditions that evaporate CO.

7.4 Discussion

Of the three processes thought to play important roles in the formation and evolution of ice mantles described in §6.4, grain surface reactions must be the dom-

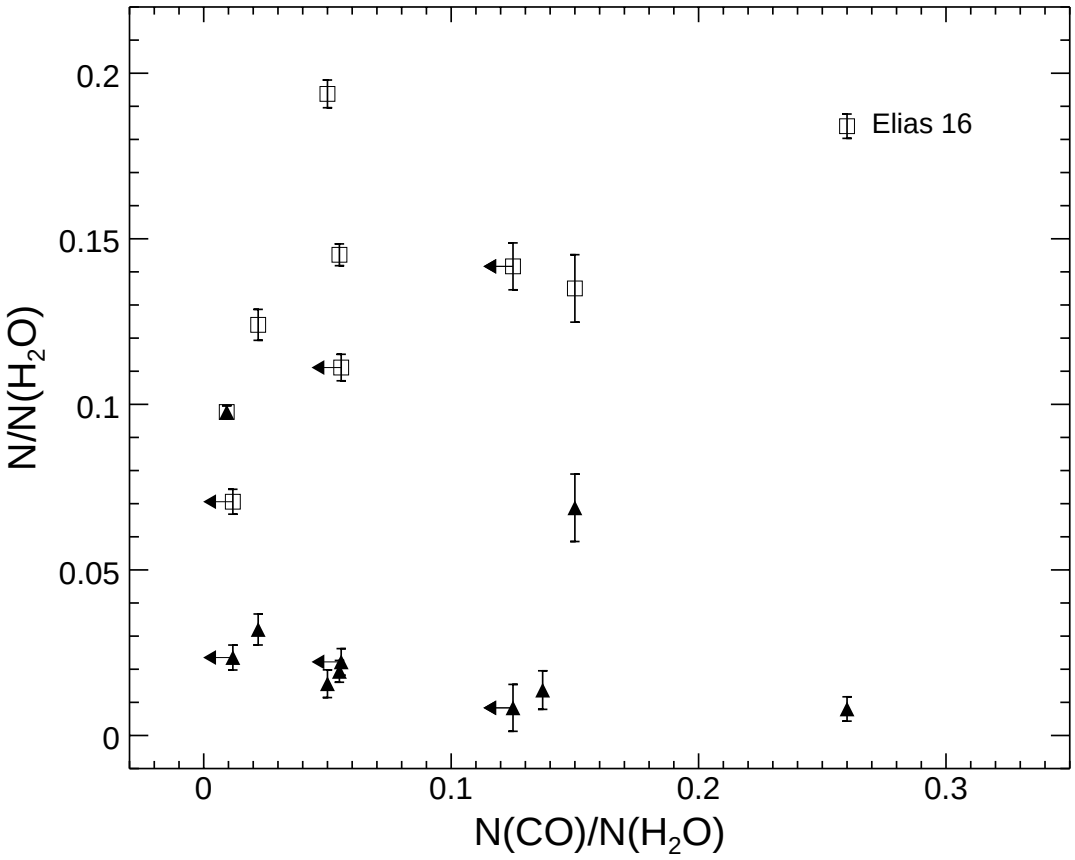

Figure 7.16: Column densities of polar and nonpolar CO_2 vs. N_{CO}, all normalized to N_{H_2O}. Squares– polar CO_2; Triangles– nonpolar CO_2. Arrows indicate upper limits on CO concentration. Elias 16 is indicated.

inant source of primary ices in molecular clouds, as there is simply no other way to explain the abundance of H_2O, the dominant constituent, in the mantles (e.g., Whittet 1992). Processing by UV photolysis or ion bombardment is often assumed to play the key role in regions of recent star formation, driving the evolution of the ices from simple volatiles to more complex organic refractory materials (Agarwal et al. 1985). Detection of ubiquitous solid CO_2 might seem consistent with this assumption, given the ease with which CO_2 is formed by photolysis reactions in laboratory ices. However, our detailed analysis of the observations lead us to conclude (below) that it is *thermal* rather than processing by UV and/or cosmic rays that is the dominant process in molecular clouds close to young stars.

7.4.1 Protostars vs. Field Stars: Evidence for thermal processing

As already discussed, the sources in this sample fall essentially into two broad groups, "field stars", in which there is little or no interaction between the source and the molecular cloud containing the CO_2, and "embedded protostars", in which the surrounding molecular cloud may be heated and/or irradiated by the source itself. The prototypical field star is Elias 16. Although the exact locations of the molecular clouds toward the Galactic Center are not known, it is reasonable to place Sgr A*, at least, in a group with Elias 16.

The area of sky included in the SWS aperture centered on Sgr A* is about $14'' \times 20$–$27''$ (wavelength dependent) so the observed spectrum likely includes flux contributions from several Galactic Center IR sources (GC IRS 1, 2, 3, 6, 7, 9, 10, and 21). In common with Elias 16, molecular cloud material toward Sgr A* appears to be cold, with CO_2 residing almost entirely in polar ice matrices: the 15.2 μm feature lacks structure associated with annealing; although the 15.2 μm feature of Elias 16 is unavailable for direct comparison (due to this star's low flux level and the SWS sensitivity at that wavelength), fits to its stretching mode preclude a strong nonpolar contribution (Whittet et al. 1998). Detection of solid CO in the spectra of some of the individual IRS toward Sgr A* (McFadzean et al. 1989; Chiar et al. 1998a) is further evidence that the molecular cloud(s) in this general line of sight are cold. Serabyn & Güsten (1986) measured the kinetic temperature of NH_3 gas toward Sgr A* and found two components with temperatures of 16.5 ± 2.5 K, and 240 ± 100 K, consistent with values based on CO observations by Hüttemeister et al. (1993) of ~ 25 and 200 K. It is assumed therefore that the icy material is associated with gas at $\sim$ 15–25 K.

These results show that CO_2 toward protostellar sources is an indicator of thermal annealing in each line of sight, and its matrix interactions trace the thermal history of the ices present with a high degree of sensitivity. Especially sensitive is the splitting of the bending mode in molecular complexes and when the axial symmetry of the molecule is broken. Toward sources previously thought to have the highest levels of processing (W33 A, GL 2136) a strong shoulder at 15.4 μm appears, due the formation of molecular complexes with CH_3OH and other polar molecules

(Ehrenfreund et al. 1998).

The consistency in CO_2/H_2O ratio from source to source implies that the CO_2 column density does not depend on the irradiation dose due to the protostellar UV flux but merely on the amount of total molecular material present. If CO_2 is formed by reactions of H_2O and CO, then a correlation between the abundances of CO_2 and polar CO should exist, but no clear evidence is present in the observed spectra. The correlations observed here seem to reflect the temperature dependences of the CO_2 polar and nonpolar phases, but no clear relationship exists with the polar and nonpolar phases of CO. If CO_2 is formed by CO + O $\rightarrow$ CO_2 on grain surfaces, the limiting factor may be the abundance of atomic O, which quickly becomes devoured in the formation of both CO and O_2 (Chiar 1997). Perhaps the concentration of CO_2 observed is the end result of a photochemical equilibrium between different mantle constituents. However, field stars provide the control group for the results on protostars: the fact that the CO_2/H_2O ratio in Elias 16 and Sgr A* is comparable with that for the protostellar sources (Fig. 7.14) implies that CO_2 is formed in the absence of embedded sources, and thus before any processing by UV photons takes place (other than that induced by cosmic rays and the weak interstellar radiation field within dense clouds). The primary conclusion of this study is thus simply that *the spectral evolution of the* CO_2*-bearing ices is dominated by thermal processing.*

7.4.2 Thermal Annealing and the Evolution of the Ices

Although evidence for thermal processing is found in these observations, it seems unlikely that this process is implicated in the *formation* of CO_2. The presence of CO_2 in field stars indicates that it must form at low temperature, by surface reactions or by processing driven by cosmic rays or the ISRF (see Whittet et al. 1998 for further discussion). In any case, the consistent CO_2/H_2O ratio from source to source implies a formation process for CO_2 which is the same in all clouds (e.g., a similar cosmic-ray ionization rate, if the formation is by cosmic-ray–induced UV). This question is yet to be resolved.

The simple overall picture drawn from these observations is that CO_2 is formed in an H_2O-rich environment at an abundance of 17 % relative to H_2O ice *in the*

quiescent cloud environment. Likely, some methanol is formed in this ice as well. Subsequent warm-up of this ice by a newly formed star leads to the formation of CH_3OH:CO_2 complexes and eventually complete ice segregation into H_2O-rich and CO_2-rich ice phases *on the same grain.* The same heating leads to the evaporation of any nonpolar CO ice mantle present.

Finally, the (perhaps) surprising lack of evidence for radiative processing by embedded protostars in the data is considered. Observations of compact H II regions (Chini et al. 1986a, 1986b; Wood, Churchwell, & Salter 1988; Wood & Churchwell 1989) require the presence of OB stars in order to explain IR flux levels emitted from the dust that encloses them. These regions are likely to be radiation limited, i.e. their boundaries are determined by the flux of photons beyond the Lyman limit rather than by the availability of material to be ionized. The radiation which escapes the H II and photon-dominated regions has an energy below that required for the ionization of H (13.6 eV) and the dissociation of H_2 and CO (11.3–13.6 eV). [14] The UV radiation field is lowered only by dust extinction beyond the photon-dominated region. However, the general absence of recombination lines in the spectra of the observed sources suggests that many have not yet reached the stage of forming extended H II regions, and therefore UV processing by the embedded protostars may play only minor roles in the evolution of the CO_2-bearing ices. Thermal processing, on the other hand, may be driven by copious IR radiation from young stars which is ubiquitous and relatively unattenuated. For instance, a previous study of the methanol C–O stretch toward GL 2136 by Skinner et al. (1992) has shown that thermal segregation of the H_2O:CH_3OH ices plays an important role there.

[14] The dissociation energy of $H_2 \rightarrow 2\,H$ is 4.48 eV, but photodissociation can only initiated by absorption of photons in the 912–1100Å range ($E = 11.3$–13.6 eV). This excitation is followed by decay back into the vibrationally continuum of the ground state, which then dissociates.

CHAPTER 8
SUMMARY & CONCLUSIONS

"FINALIZE: ... a peculiarly fuzzy and silly word. Does it mean 'terminate,' or does it mean 'put into final form'? One can't be sure, really, what it means, and one gets the impression that the person using it doesn't know, either, and doesn't want to know."

E. B. White, *An Approach to Style*

8.1 Laboratory Astrophysics

Chapters 2–4 have demonstrated some of the techniques of laboratory astrophysics and shown two examples of experiments pertaining to interstellar ices and their properties. It is important to stress the need for laboratory data to observational astronomers– for example, measurements of column density rely critically on the adopted values for IR absorption strengths of observed features (Ch. 3). Feature profiles are strongly dependent on many factors of the ice environment, and spectral details may be systematically cataloged in the laboratory according to small changes in ice character. Due to the highly non-linear problem of deconvolving observed ice features into those of their parent species, it is necessary to compare spectroscopic observations with a wide range of laboratory-produced analogs in order to extract any meaningful information.

8.1.1 IR Absorption Strengths

In Chapter 3, the IR absorption strengths of H_2O, CO and CO_2 were measured in a variety of mixtures. New experimental methods were implemented, relying on independent depositions of dilutant and subject molecules. It was shown that the strengths of the CO and CO_2 IR features *do not vary with environment*, a result somewhat contradictory to those in the literature (which rely on experimental methods with several possible sources of systematic error; see §3.2.1). The reversible

temperature dependence of the CO 4.67 μm (2138 cm^{-1}) stretching feature was found to be consistent with previous studies. No significant temperature dependence was shown for CO_2. The features of H_2O did show a small dependence on the amount of nonpolar molecules diluted within its ice matrix. For instance, in mixtures of H_2O:CO ~ 1, the strength of the 3 μm (3280 cm^{-1}) feature of H_2O is decreased by 5 % relative to that in a pure H_2O ice (§ 3.3.4): this effect is well-modeled by a semi-empirical treatment of dilution (Eq. 3.2). All features of H_2O also show an irreversible temperature evolution.

The general conclusion of Ch. 3 has a certain aesthetic appeal: while the profiles of IR absorption features vary widely from ice mixture to ice mixture, the total absorption underneath a feature (per molecule) remains essentially constant. This statement was shown to be accurate (within approximately 15 %) in the cases of the fundamental CO and CO_2 vibrational features. However, the effects of dilution were shown to play a non-negligible role in the cases of strongly interacting molecules such as H_2O (albeit a minor one; the largest change in A_{H_2O} was $\lesssim 20$ % in a mixture with approximately equal parts H_2O and a nonpolar species such as CO or CO_2).

As a consequence of this result, the column densities of molecules may be accurately calculated *independent of any multicomponent structure* in the absorption. Observed abundances depend only on the *total* integrated optical depth under the feature in question. For example, the features of interstellar CO_2 observed in Ch. 7 revealed many CO_2 components along the protostellar sight-lines, but the total abundance in each case may be determined by the total area of its features.

8.1.2 Ultraviolet Processing of Pure Ices

The experiments presented in Chapter 4 show that a highly complex chemistry can result in the UV photolysis of even pure ice mixtures. The lack of such experiments in the literature, in favor of multicomponent ices, is therefore somewhat surprising. Many species were observed in Ch. 4 that had not been seen in previous studies. This is likely due to the purity of the ices studied in this work, thus precluding reactions with photoproducts from other ice species as well as the spectral confusion due to overlapping IR features of major ice components.

Of the nine ices studied in Ch. 4, the most fruitful were CH_4, H_2CO, and CH_3OH. All three produced high abundances of complex organic material on the timescales relevant to dense molecular clouds (§ 4.3). The most susceptible molecule to the irradiating photons was H_2CO (§ 4.3.8), which was quickly polymerized into POM (and other chains) and dissociated into molecules such as CO and CO_2. Some CH_3OH was also produced, presumably through hydrogenation of the CO produced as a first-order product. The major products from the pure CH_3OH experiment (§ 4.3.9) were CO, CO_2, and methyl formate: indicating that this molecule is another possible source for complex interstellar materials. Irradiations of CH_4 produced mostly ethane (C_2H_6), and highly-branched structures containing $\geq$ 7 C atoms: species such as these are thought to produce the observed features in the aliphatic stretching region near 3.4 μm (2940 cm^{-1}; see § 1.3).

Photoproduction yields for the other molecules studied (H_2O, NH_3, CO, CO_2, N_2, and O_2) were generally low and less complex in nature, with two or three major photoproducts. In the case of CO, it was shown that this molecule in its pure state is extremely resistant to the range of UV radiation applied, and only a small amount of CO_2 was produced (0.8 % relative to the initial CO ice deposition; see § 4.3.4). In contrast, irradiated mixtures of CO:H_2O and CO:O_2 are known to be highly efficient producers of CO_2.

8.2 Interstellar Solid Carbon Dioxide

An abundant component of interstellar icy grain mantles due to CO_2 has long been expected, but strong atmospheric interferences have prevented its direct detection in the ISM. CO_2 observations had to await the launch of a space-based platform such as ISO (described in § 5.1). In Chapters 6 and 7, I have presented some of the first high-resolution ($\lambda/\Delta\lambda \approx$ 1000–2000) spectroscopic observations of solid CO_2 in dense molecular clouds obtained by the SWS instrument on board ISO.

Chapter 6 contains observations of CO_2 toward Elias 16, a line of sight representing the quiescent ISM where no internal sources of radiation are present. The observed CO_2 abundance toward Elias 16 is 18 % relative to solid H_2O. Nearly all of the CO_2 appears to reside in a polar (H_2O-dominated) mantle. This result is

somewhat surprising, given the common assumption in the last 10 years that CO_2 is produced mainly by the processing of CO-bearing ices near embedded protostars (see § 8.2.1 below).

Three lines of sight toward the Galactic Center are also included in this study (Sgr A*, GCS 3 I, and GCS 4; see Ch. 7). The observations of CO_2 toward Sgr A* in Ch. 7 place this source in a category similar to Elias 16, since it appears to be cold ($T \lesssim 30\,K$), with CO_2 residing almost entirely in polar matrices (see § 7.3).

The remaining ten sources in the CO_2 program were lines of sight toward deeply embedded protostars. In these environments, the icy grain mantles are thought to be highly processed by UV and IR radiation from the young stellar object. The complexity in the observed profiles of the interstellar CO_2 bending modes at 15.2 μm (660 cm^{-1}) was another somewhat surprising result. Sharp peaks on this feature appear in almost every observation of a protostar (see Figs. 7.1–7.5). Comparisons with laboratory spectra (§ 7.3.3) indicate that these structures are due to CO_2 ice in a relatively pure state. Other aspects of the CO_2 bending mode profiles (namely, the shoulders at 15.4 μm/650 cm^{-1}) indicate that this structure may derive from thermal annealing which has both segregated the CO_2 and formed CO_2 complexes with other ice components. In particular, CO_2:CH_3OH complexes are shown to give rise to a such a bending mode profile.

8.2.1 Possible Origins of CO_2

Carbon dioxide is efficiently produced in laboratory photolysis experiments involving CO-bearing ice mixtures. This fact has commonly led to the assumption that its major interstellar production pathway lay also in energetic processing, driven by the UV flux of nearby protostars. In all observed lines of sight considered in Chs. 6 and 7, the CO_2 abundance relative to H_2O ice falls in the range from 9 to 23 %: a remarkable consistency given the diverse nature of the data set. Such a similarity between sight-lines would not be expected if the abundances of CO_2 were determined merely by the UV flux of the embedded protostar and the amount of UV extinction between the source and the relevant regions of the molecular cloud. Moreover, the comparable values of N_{CO_2}/N_{H_2O} between both *embedded* and *quiescent* lines of

sight implies a common origin in both cases, one that must preclude the necessity for embedded sources of radiation.

Another possible production route for CO_2 is the oxidation of CO ($CO + O \rightarrow CO_2$) on grain surfaces. This reaction possesses a small energetic barrier (10–30 K) that may be easily overcome even at the low temperatures in the quiescent cloud medium where $T < 20\,K$ (see § 1.3 and § 6.4). The CO_2 toward Elias 16 resides in a polar (H_2O-rich) mantle (§ 6.3), and in the grain surface reaction scheme, it must therefore form simultaneously with H_2O in an environment where a significant abundance of atomic H is present in the accreting gas. A problem with this model is the requirement to form CO_2 in a situation where hydrogenation is important (to form H_2O), yet CO is preferentially oxidized to CO_2 rather than hydrogenated to form CH_3OH (see § 6.4).

CO_2 may also be produced by photolysis in the outer regions of molecular clouds where the ISRF is relatively unattenuated. The positive N_{CO_2} intercept on the plot of N_{CO_2} vs. N_{CO} (Fig. 7.15) would imply that $CO \rightarrow CO_2$ conversion is nearly complete there. Moreover, the ISRF does deliver enough flux to the outer edges of molecular clouds ($A_V \leq 5\,mag$) to account for the observed CO_2 abundances (§ 6.4). A constant cosmic-ray–ionization rate within these clouds may also be implied by the observed linear trend in N_{CO_2} vs. N_{CO} (with a slope of approximately 1.0; see Eq. 7.2).

In the UV-formation model, therefore, most CO_2 is formed in the outer edges of molecular clouds (where some enhancement is possible by filamentary cloud structure), with additional formation within the cloud by cosmic-ray–induced UV. However, if CO_2 is indeed produced by UV photolysis, it is somewhat surprising that the 4.62 μm (2160 cm^{-1}) "XCN" feature, normally considered an indicator of energetic processing of grain mantles, is absent in Elias 16. Perhaps, in quiescent-cloud ice mantles, the formation of CO_2 requires a smaller UV dose than is needed to form XCN. This assertion agrees with laboratory results from d'Hendecourt et al. (1986) who showed that 24 hours of UV irradiation produced 5–10 times more CO_2 than XCN in a mixture of H_2O:CO:CH_4:NH_3 = 6:2:1:1 at low temperature.

8.2.2 CO_2 and Thermal Annealing

Fits to the observed features with laboratory-obtained spectra (§ 7.3.3) indicated that interstellar solid CO_2 exists in at least two major environments: one that is polar (H_2O- or CH_3OH-rich), and one that is nonpolar (e.g., CO_2- or CO-rich). The origin of the nonpolar component is not clear, but the best laboratory fits are those where annealing of CO_2 has occurred in a CH_3OH-rich polar ice to form CO_2:CH_3OH complexes (§ 7.3.3.2). Constraints on the amounts of CH_3OH required are consistent with known upper limits for N_{CH_3OH}. Most differences in CO_2 spectra between sources (especially in the bending mode) may be explained merely by the temperature of the annealed ice (and not its composition; see e.g., Fig. 7.13).

Analyses of interstellar CO_2 observations presented in Chapter 7 led to the conclusion that the dominant factor in maintaining the state of interstellar ices is *thermal processing* (§ 7.4). The correlations of CO_2 with H_2O and CO reflect the temperature dependencies of the CO_2 polar and nonpolar phases, but no clear relationship exists with the phases of CO.

The simple overall picture drawn from these observations (Chs. 6 and 7) is that CO_2 is formed in an H_2O-rich environment at an abundance of $\sim 17\,\%$ relative to H_2O ice *in the quiescent cloud environment*. Likely, some methanol is formed in this ice as well. Subsequent warm-up of this ice by the IR radiation from a newly formed star leads to the formation of CH_3OH:CO_2 complexes and eventually complete ice segregation into H_2O-rich and CO_2-rich ice phases *on the same grain*. The same heating leads to the evaporation of any nonpolar CO ice mantle present. The lack of evidence for *energetic processing* by embedded protostars may due to the fact that (i) the youngest protostars emit IR but not UV, and (ii) IR radiation is less attenuated than UV.

8.3 Future Research

The results of the previous chapters have answered many questions, but leave still more to be investigated. For instance, the IR absorption strengths of molecules such as CH_4 have yet to be studied in great detail as in Ch. 3. It is also unclear whether energetic processing of ices in the ISM is dominated by UV irradiation

(due to protostars, the ISRF, or the cosmic-ray–ionization of H_2) or by particle bombardment (by cosmic rays themselves). The final compositions of ices produced in these two processes do differ, so it is important to carefully compare their effects on the same ice in the same laboratory experiment.

The CO_2 spectra obtained by the ISO-SWS (Chs. 6 and 7) have enabled us to achieve a greater understanding of the processes which control icy grain mantle environments. On the other hand, the detection of abundant CO_2 in the quiescent ISM opens wide the topics of icy mantle formation and evolution. Unfortunately, the limited sensitivity of the SWS and the low fluxes of field stars in the relevant wavelength regions put tight constraints on the number of quiescent lines of sight observable during the ISO mission (one or two, depending on the assignment of Sgr A*). Moreover, the low flux of Elias 16 beyond $\lambda \approx 4.5\,\mu$m ($2200\,\mathrm{cm}^{-1}$) precluded detection of the CO_2 bending mode at $15.2\,\mu$m ($660\,\mathrm{cm}^{-1}$), a sensitive diagnostic of the CO_2-bearing ices. One might predict that the bending mode toward Elias 16 would resemble that of Sgr A*: a broad feature with no sub-peaks, indicative of CO_2 in a polar ice matrix (Fig. 7.2).

Careful studies of CO_2 toward quiescent cloud sources with NASA's Space Infrared Telescope Facility (SIRTF) may answer this question, since the sensitivity of the SIRTF Infrared Spectrograph (IRS) will allow observations of field stars and low-mass young stellar objects that fell below the limit of the ISO SWS. It will observe in the spectral range from 10 to $37\,\mu$m with a resolution $\lambda/\Delta\lambda \sim 600$, sufficient to resolve the substructure in the CO_2 bending mode at $15.2\,\mu$m ($660\,\mathrm{cm}^{-1}$). As shown in Ch. 7 and described above, the profile of this feature is an important indicator of annealing levels and ice composition. Its observation toward a large group of field stars, as opposed to the $4.27\,\mu$m ($2340\,\mathrm{cm}^{-1}$) CO_2 stretching feature which is often near saturation in the ISO-SWS spectra, may provide the most important information about the nature of CO_2 ice mantles in quiescent clouds.

The abundance of CO_2 vs. line-of-sight visual extinction (A_V) in quiescent clouds may be an indicator of the CO_2 formation process. If it is formed mainly by the grain surface oxidation of CO, then the concentration of CO_2 in the grain mantle should depend merely on the availability of these species in the gas phase,

and would likely not depend strongly on A_V (measured values of N_{CO_2}/A_V would show little or no dependence on A_V). However, if radiative processes due to the ISRF is the key to forming CO_2, then one might expect its production to be most efficient at low extinctions, where the ISRF is strongest. At values of $A_V \gtrsim 5\,\mathrm{mag}$, the ISRF becomes negligible and the level of CO_2 formation dependent merely on the cosmic-ray–ionization rate, which is constant throughout the cloud. Therefore, lines of sight with low extinctions would produce most of the CO_2 observed. A corresponding plot of N_{CO_2} vs. A_V would show a quick increase below $A_V \lesssim 5\,\mathrm{mag}$, where it may level off to a slower increase due to a relatively constant production due to cosmic-ray–induced UV which exists throughout the cloud.

REFERENCES

Acquista, N., Schoen, L. J., & Lide, D. R. 1968, J. Chem. Phys., 48, 1534

Agarwal, V. K., Schutte, W., Greenberg, J. M., Ferris, J. P., Briggs, R., Connor, S., van de Bult, C. P. E. M., & Baas, F. 1985, Origins Life Evol. Biosphere, 16, 21

Allamandola, L. J., Sandford, S. A., Tielens, A. G. G. M., & Herbst, T. M. 1992, ApJ, 399, 134

Allamandola, L. J., Sandford, S. A., & Valero, G. J. 1988, Icarus, 76, 225

Ausloos, P., Rebbert, R. E., & Lias, S. G. 1965, J. Chem. Phys., 42, 540

Behringer, R. E. 1958, J. Chem. Phys., 29, 537

Bernstein, M. P., Sandford, S. A., & Allamandola, L. J. 1997, ApJ, 476, 932

Bernstein, M. P., Sandford, S. A., Allamandola, L. J., Chang, S., & Scharberg, M. A. 1995, ApJ, 454, 327

Blake, G. A., Sutton, E. C., Masson, C. R., & Phillips, T. G. 1987, ApJ, 315, 621

Bohren, C. F., & Huffman, D. R. 1983, Absorption and Scattering of Light by Small Particles (New York: J. Wiley & Sons), Ch. 5

Boogert, A. C. A., Ehrenfreund, P., Gerakines, P. A., Tielens, A. G. G. M., Whittet, D. C. B., Schutte, W. A., van Dishoeck, E. F., & de Grauuw, T. 1998, A&A, accepted

Boogert, A. C. A., Schutte, W. A., Helmich, F. P., Tielens, A. G. G. M., & Wooden, D. H. 1997, A&A, 317, 929

Boogert, A. C. A., et al. 1996, A&A, 315, L377

Boonman, A., et al. 1998, in preparation

Braun, W., Baas, A. M., & Pilling, M. 1970, J. Chem. Phys., 52, 5131

Brecher, C., & Halford, R. S. 1961, J. Chem. Phys., 35, 1109

Brewer, L., & Wang, J. L. 1972, J. Chem. Phys., 56, 759

Briggs, R., Ertem, G., Ferris, J. P., Greenberg, J. M., McCain, P. J., Mendoza-Gomez, C. X., & Schutte, W. A. 1992, Origins Life Evol. Biosphere, 22, 287

Brooke, T. Y., Sellgren, K., & Smith, R. G. 1996, ApJ, 459, 209

Brown, P. D., & Charnley, S. B. 1990, MNRAS, 244, 432

Cairns, B. R., & Pimentel, G. C. 1965, J. Chem. Phys., 43, 3432

Caselli, P., Hasegawa, T. I., & Herbst, E. 1993, ApJ, 408, 548

Charnley, S. B., Tielens, A. G. G. M., & Millar, T. J. 1992, ApJ, 399, L71

Chesters, M. A., & McCash, E. M. 1987, Spectrochim. Acta, 43A, 1625

Chiar, J. E. 1997, Origins Life Evol. Biosphere, 27, 79

Chiar, J. E., et al. 1998a, in preparation

Chiar, J. E., Adamson, A. J., Kerr, T. H., & Whittet, D. C. B. 1994, ApJ, 426, 240

Chiar, J. E., Adamson, A. J., Kerr, T. H., & Whittet, D. C. B. 1995, ApJ, 455, 234

Chiar, J. E., Adamson, A. J., & Whittet, D. C. B. 1996, ApJ, 472, 665

Chiar, J. E., Gerakines, P. A., Whittet, D. C. B., Pendleton, Y. J., Tielens, A. G. G. M., Adamson, A. J., & Boogert, A. C. A. 1998b, ApJ, 498, 716

Chini, R., Kreysa, E., Mezger, P. G., & Gemünd, H.-P. 1986a, A&A, 154, L8

Chini, R., Kreysa, E., Mezger, P. G., & Gemünd, H.-P. 1986b, A&A, 157, L1

Chlewicki, G. 1985, Ph.D. thesis, Leiden University, Leiden, the Netherlands

Comeford, J. J., & Gould, J. H. 1960, J. Mol. Spectr., 5, 474

de Graauw, T., Haser, L. N., Beintema, D. A., Roelfsema, P. R., van Agthoven, H., Barl, L., et al. 1996, A&A, 315, L49

DeKock, R. L., & Weltner, W. 1971, J. Am. Chem. Soc., 93, 7106

d'Hendecourt, L., et al. 1996, A&A, 315, L365

d'Hendecourt, L. B., & Allamandola, L. J. 1986, A&AS, 64, 453

d'Hendecourt, L. B., Allamandola, L. J., & Greenberg, J. M. 1985, A&A, 152, 130

d'Hendecourt, L. B., Allamandola, L. J., Grim, R. J. A., & Greenberg, J. M. 1986, A&A, 158, 119

d'Hendecourt, L. B., & Jourdain de Muizon, M. 1989, A&A, 223, L5

Draine, B. T., & Lee, H. M. 1984, ApJ, 285, 89

Duley, W. W., & Williams, D. A. 1981, MNRAS, 196, 269

Duncan, J. L., McKean, D. C., & Mallinson, P. D. 1973, J. Mol. Spectr., 45, 221

Ehrenfreund, P., et al. 1998, in preparation

Ehrenfreund, P., Boogert, A. C. A., Gerakines, P. A., Jansen, D. J., Schutte, W. A., Tielens, A. G. G. M., & van Dishoeck, E. F. 1996, A&A, 315, L341

Ehrenfreund, P., Boogert, A. C. A., Gerakines, P. A., Tielens, A. G. G. M., & van Dishoeck, E. F. 1997, A&A, 328, 649

Ehrenfreund, P., Breukers, R., d'Hende court, L. B., & Greenberg, J. M. 1992, A&A, 260, 431

Elias, J. H. 1978a, ApJ, 224, 453

Elias, J. H. 1978b, ApJ, 224, 857

Elsila, J., Allamandola, L. J., & Sandford, S. A. 1997, ApJ, 479, 818

Evans, I., Neal J., Lacy, J. H., & Carr, J. S. 1991, ApJ, 383, 674

Fan, L., & Ziegler, T. 1992, J. Chem. Phys., 96, 9005

Geballe, T. R. 1986, A&A, 162, 248

Geballe, T. R., Baas, F., Greenberg, J. M., & Schutte, W. 1985, A&A, 146, L6

Gerakines, P. A., Schutte, W. A., & Ehrenfreund, P. 1996, A&A, 312, 289

Gerakines, P. A., Schutte, W. A., Greenberg, J. M., & van Dishoeck, E. F. 1995, A&A, 296, 810

Gerakines, P. A., et al. 1998, in preparation

Giguère, P. A., & Harvey, K. B. 1959, J. Mol. Spectr., 3, 36

Gillett, F. C., & Forrest, W. J. 1973, ApJ, 179, 483

Goldanskii, V. I., Frank-Kamenetskii, M. D., & Barkalov, I. M. 1973, Science, 182, 1344

Gredel, R., Lepp, S., Dalgarno, A., & Herbst, E. 1989, ApJ, 347, 289

Greenberg, J. 1973, in Molecules in the Galactic Environment, ed. M. A. Gordon & L. E. Snyder (New York: Wiley), 94

Greenberg, J. M. 1979, in Stars and Star Systems, ed. B. E. Westerlund (Dordrecht: Reidel), 173

Greenberg, J. M. 1982, in Submillimetre Wave Astronomy, ed. J. E. Beckman & J. P. Philips (Cambridge University Press), 261

Greenberg, J. M., van de Bult, C. E. P. M., & Allamandola, L. J. 1983, J. Phys. Chem., 87, 4243

Grim, R. J. A. 1988, Ph.D. thesis, Leiden University, Leiden, the Netherlands

Grim, R. J. A., & d'Hendecourt, L. B. 1986, A&A, 167, 161

Grim, R. J. A., & Greenberg, J. M. 1987, ApJ, 312, L91

Grim, R. J. A., Greenberg, J. M., de Groot, M. S., Baas, F., Schutte, W. A., & Schmitt, B. 1989, A&AS, 78, 161

Gürtler, J., Henning, T., Koempe, C., Pfau, W., Krätschmer, W., & Lemke, D. 1996, A&A, 315, L189

Hagen, W. 1982, Ph.D. thesis, Leiden University, Leiden, The Netherlands

Hagen, W., Allamandola, L. J., & Greenberg, J. M. 1979, Ap&SS, 65, 215

Hagen, W., Greenberg, J. M., & Tielens, A. G. G. M. 1983, A&A, 117, 132

Hagen, W., & Tielens, A. G. G. M. 1981, J. Chem. Phys., 75, 4198

Hasegawa, T. I., & Herbst, E. 1993, MNRAS, 263, 589

Hasegawa, T. I., Herbst, E., & Leung, C. M. 1992, ApJS, 82, 167

Helmich, F. P. 1996, Ph.D. thesis, Leiden University, Leiden, the Netherlands

Herbst, E., & Leung, C. M. 1986, MNRAS, 222, 689

Herbst, E., & Leung, C. M. 1989, ApJS, 69, 271

Hiraoka, K., Ohashi, N., Kihara, Y., Yamamoto, K., Sato, T., & Yamashita, A. 1994, Chem. Phys. Lett., 229, 408

Hollenbach, D., & Salpeter, E. E. 1971, ApJ, 163, 155

Hudgins, D. M., Sandford, S. A., Allamandola, L. J., & Tielens, A. G. G. M. 1993, ApJS, 86, 713

Hüttemeister, S., Wilson, T. L., Bania, T. M., & Martín-Pintado, J. 1993, A&A, 280, 255

Irvine, W. M., Goldsmith, P. F., & Hjalmarson, A. 1987, in Interstellar Processes, ed. D. J. Hollenbach & H. A. Thronson (Reidel), 561

Jacox, M. E. 1981, Chem. Phys., 59, 213

Jacox, M. E., & Milligan, D. E. 1972, J. Mol. Spectr., 42, 495

Jacox, M. E., Milligan, D. E., Moll, N. G., & Thompson, W. E. 1965, J. Chem. Phys., 43, 3734

Jiang, G. J., Person, W. B., & Brown, K. G. 1975, J. Chem. Phys., 64, 1201

Kemper, M. J. H., Hoeks, C. H., & Buck, H. M. 1981, J. Chem. Phys., 74, 5749

Kerr, T. H., Adamson, A. J., & Whittet, D. C. B. 1993, MNRAS, 262, 1047

Kissel, J., & Krueger, F. R. 1987, Nature, 326, 755

Kitta, K., & Krätschmer, W. 1983, A&A, 122, 105

Klein, M. L., & Venables, J. A., ed. 1976, Rare Gas Solids, Vol. 1 (London: Academic Press)

Lacy, J. H., Baas, F., Allamandola, L. J., Persson, S. E., McGregor, P. J., Lonsdale, C. J., Geballe, T. R., & van de Bult, C. E. P. 1984, ApJ, 276, 533

Lacy, J. H., Carr, J. S., Evans, N. J., II, Bass, F., Achtermann, J. M., & Arens, J. F. 1991, ApJ, 376, 556

Larson, H. P., Davis, D. S., Black, J. H., & Fink, U. 1985, ApJ, 299, 873

Leitch-Devlin, M. A., & Williams, D. A. 1985, MNRAS, 213, 295

Lindblad, B. 1935, Nature, 135, 133

Luiti, G., Dondes, S., & Harteck, P. 1966, J. Chem. Phys., 44, 4051

Lutz, D., et al. 1996, A&A, 315, L269

Maki, A. G., & Toth, R. 1965, J. Mol. Spectr., 17, 136

Mansueto, E. S., Ju, C.-Y., & Wight, C. A. 1989, J. Phys. Chem., 93, 2143

Mansueto, E. S., & Wight, C. A. 1989, J. Am. Chem. Soc., 111, 1900

Mathis, J. S., Metzger, P. G., & Panagia, N. 1983, A&A, 128, 212

Mathis, J. S., Rumpl, W., & Nordsieck, K. H. 1977, ApJ, 217, 425

McFadzean, A. D., Whittet, D. C. B., Bode, M. F., Adamson, A. J., & Longmore, A. J. 1989, MNRAS, 241, 873

Millar, T. J., Bennett, A., Rawlings, J. M. C., Brown, P. D., & Charnley, S. B. 1991, A&AS, 87, 585

Milligan, D. E., Brown, H. W., & Pimentel, G. C. 1959, J. Chem. Phys., 25, 1080

Milligan, D. E., & Jacox, M. E. 1965, J. Chem. Phys., 43, 4487

Milligan, D. E., & Jacox, M. E. 1971, J. Chem. Phys., 54, 927

Mitchell, G. F., Lee, S. W., Maillard, J.-P., Matthews, H., Hasegawa, T. I., & Harris, A. I. 1995, ApJ, 438, 794

Mitchell, G. F., Maillard, J.-P., Allen, M., Beer, R., & Belcourt, K. 1990, ApJ, 363, 554

Moll, N. B., Ckitter, D. R., & Thompson, W. E. 1966, J. Chem. Phys., 45, 4469

Moore, M. H., Donn, B., Khanna, R., & A'Hearn, M. F. 1983, Icarus, 54, 388

Moore, M. H., Khanna, R., & Donn, B. 1991, J. Geophys. Res., 96, 17541

Ohishi, M., et al. 1991, ApJ, 380, L39

Okabe, H. 1978, Photochemistry of Small Molecules (New York: Wiley)

Oort, J. H., & van de Hulst, H. C. 1946, Bull. Astron. Inst. Netherlands, 10, 187

Pacansky, J., & Bargon, J. 1975, J. Am. Chem. Soc., 97, 6896

Pacansky, J., Koch, W., & Miller, M. D. 1981, J. Am. Chem. Soc., 113, 317

Palumbo, M. E., Geballe, T. R., & Tielens, A. G. G. M. 1997, ApJ, 479, 839

Palumbo, M. E., & Strazzulla, G. 1993, A&A, 269, 568

Pendleton, Y. J., Sandford, S. A., Allamandola, L. J., Tielens, A. G. G. M., & Sellgren, K. 1994, ApJ, 437, 683

Pendleton, Y. J., Tielens, A. G. G. M., & Werner, M. W. 1990, ApJ, 349, 107

Pouchert, C. J., ed. 1981, The Aldrich Library of Infrared Spectra, edition III (Millwaukee: Aldrich Chemical Company)

Prasad, S. S., & Tarafdar, S. P. 1983, ApJ, 267, 603

Pratap, P., Dickens, J. E., Snell, R. L., Miralles, M. P., Bergin, E. A., Irvine, W. M., & Schloerb, F. P. 1997, ApJ, 486, 862

Rosengren, K., & Pimentel, G. C. 1965, J. Chem. Phys., 43, 507

Roux, J. A., & Wood, B. E. 1983, J. Opt. Soc. Am., 73, 1181

Salama, F., & Allamandola, L. J. 1992, ApJ, 395, 301

Salama, F., Bakes, E. L. O., Allamandola, L. J., & Tielens, A. G. G. M. 1996, ApJ, 458, 621

Sandford, S. A., & Allamandola, L. J. 1990, ApJ, 355, 357

Sandford, S. A., & Allamandola, L. J. 1993, ApJ, 409, L65

Sandford, S. A., Allamandola, L. J., Tielens, A. G. G. M., Sellgren, K., Tapia, M., & Pendleton, Y. 1991, ApJ, 371, 607

Sandford, S. A., Allamandola, L. J., Tielens, A. G. G. M., & Valero, G. J. 1988, ApJ, 329, 498

Saussey, J., Lamotte, J., & Lavalley, J. C. 1976, Spectrochim. Acta, 32A, 763

Schaeidt, S. G., et al. 1996, A&A, 315, L55

Schmitt, B., Greenberg, J. M., & Grim, R. J. A. 1989, ApJ, 340, L33

Schutte, W. A. 1988, Ph.D. thesis, Leiden University, Leiden, the Netherlands

Schutte, W. A., Allamandola, L. J., & Sandford, S. A. 1993, Icarus, 104, 118

Schutte, W. A., Gerakines, P. A., Geballe, T. R., van Dishoeck, E. F., & Greenberg, J. M. 1996a, A&A, 309, 633

Schutte, W. A., & Greenberg, J. M. 1991, A&A, 244, 190

Schutte, W. A., et al. 1996b, A&A, 315, L333

Seloudoux, R., Soussen-Jacob, J., & Vincent-Geisse, J. 1979, Chem. Phys., 40, 257

Serabyn, E., & Güsten, R. 1986, A&A, 161, 334

Shalabiea, O. M., & Greenberg, J. M. 1994, A&A, 290, 266

Skinner, C. J., Tielens, A. G. G. M., Barlow, M. J., & Justtanont, K. 1992, ApJ, 399, L79

Smith, M. A. H., Rinsland, C. P., Fridovich, B., & Rao, K. N. 1985, Molecular Spectroscopy: Modern Research, ed. K. N. Rao, Vol. III (London: Academic Press), 111

Smith, R. G., Sellgren, K., & Brooke, T. Y. 1993, MNRAS, 263, 749

Smith, R. G., Sellgren, K., & Tokunaga, A. T. 1989, ApJ, 344, 413

Smith, W. H., & Leroi, G. E. 1966, J. Chem. Phys., 45, 1767

Snyder, L. E. 1997, Origins Life Evol. Biosphere, 27, 115

Sodeau, J. R., & Lee, E. K. 1978, Chem. Phys. Lett., 57, 71

Sternberg, A., Dalgarno, A., & Lepp, S. 1987, ApJ, 320, 676

Strazzulla, G., & Baratta, G. A. 1992, A&A, 266, 434

Tegler, S. C., Weintraub, D. A., Rettig, T. W., Pendleton, Y. J., Whittet, D. C. B., & Kulesa, C. A. 1995, ApJ, 439, 279

Tielens, A. G. G. M., & Allamandola, L. J. 1987, in Interstellar Processes, ed. D. Hollenbach & H. Thronson (Dordrecht: Reidel), 397

Tielens, A. G. G. M., Allamandola, L. J., Bregman, J., Goebel, J., Witteborn, F. C., & d'Hendecourt, L. B. 1984, ApJ, 287, 697

Tielens, A. G. G. M., & Hagen, W. 1982, A&A, 114, 245

Tielens, A. G. G. M., Tokunaga, A. T., Geballe, T. R., & Baas, F. 1991, ApJ, 381, 181

Tielens, A. G. G. M., & Whittet, D. C. B. 1997, in IAU Symp. 178, Molecules in Astrophysics: Probes and Processes, ed. E. F. van Dishoeck (Dordrecht: Kluwer), 45

Tielens, A. G. G. M., Wooden, D. H., Allamandola, L. J., Bregman, J., & Witteborn, F. C. 1996, ApJ, 461, 210

Trotta, F. 1996, Ph.D. thesis, LGGE-CNRS, Université Joseph Fourier, Grenoble, France

Valentijn, E. A., et al. 1996, A&A, 315, L60

van de Bult, C. E. P. M., Greenberg, J. M., & Whittet, D. C. B. 1985, MNRAS, 214, 289

van de Hulst, H. C. 1957, Light Scattering by Small Particles (New York: J. Wiley & Sons), Ch. 6

van Dishoeck, E. F., & Blake, G. A. 1998, ARA&A, in press

van Dishoeck, E. F., Helmich, F. P., de Graauw, T., Black, J., Boogert, A. C. A., et al. 1996, A&A, 315, L349

von Sonntag, C. 1969, Forshr. Chem. Forsch., 13, 333

Walker, J. F. 1964, Formaldehyde (New York: Reinhold)

Weber, P., & Greenberg, J. M. 1985, Appl. Spectrosc. Rev., 1, 29

Wexler, A. S. 1967, Appl. Spectrosc. Rev., 1, 29

Whittet, D. C. B. 1992, Dust in the Galactic Environment (New York: Institute of Physics)

Whittet, D. C. B. 1997, Origins Life Evol. Biosphere, 27, 101

Whittet, D. C. B., Adamson, A. J., Duley, W. W., Geballe, T. R., & McFadzean, A. D. 1989, MNRAS, 241, 707

Whittet, D. C. B., Bode, M. F., Longmore, A. J., Admason, A. J., McFadzean, A. D., Aitken, D. K., & Roche, P. F. 1988, MNRAS, 233, 321

Whittet, D. C. B., Bode, M. F., Longmore, A. J., Baines, D. W. T., & Evans, A. 1983, Nature, 303, 218

Whittet, D. C. B., et al. 1997, ApJ, 490, 729

Whittet, D. C. B., et al. 1998, ApJ, 498, L159

Whittet, D. C. B., Longmore, A. J., & McFadzean, A. D. 1985, MNRAS, 216, 45P

Whittet, D. C. B., et al. 1996, A&A, 315, L357

Whittet, D. C. B., & Walker, H. J. 1991, MNRAS, 252, 63

Willner, S. P., et al. 1982, ApJ, 253, 174

Wood, D. O. S., & Churchwell, E. 1989, ApJS, 69, 831

Wood, D. O. S., Churchwell, E., & Salter, C. J. 1988, ApJ, 325, 694

Wormhoudt, J., & McCurdy, K. E. 1989, Chem. Phys. Lett., 156, 47

Yamada, H., & Person, W. B. 1964, J. Chem. Phys., 41, 2478

Youngquist, M. J., Crawford, B., & Overend, J. 1979, J. Phys. Chem., 83, 2638

Zhao, N. S. 1990, Ph.D. thesis, Leiden University, Leiden, the Netherlands